

# Simple Models for Late Holocene and Present-day Patagonian Glacier Fluctuation and Predictions of a Geodetically Detectable Isostatic Response

**Erik R. Ivins**

Jet Propulsion Laboratory, California Institute of Technology, Pasadena

**Thomas S. James**

Geological Survey of Canada, Pacific Geoscience Centre, Sidney, British Columbia

**Abstract.** The late Holocene glacial moraine chronology in the southernmost South American Andes includes four  $^{14}\text{C}$  dated Neoglacial advances and retreats. These are used as proxy information to characterize mass fluctuation of the Patagonian icefields during the last 5 thousand years. Modeled ice loads force a phase lagged viscoelastic gravitational deformation of the solid Earth. The ancient glacier fluctuations may, therefore, drive present-day crustal motion even in the absence of present-day ice mass imbalance. Numerical models show that such rates of present-day uplift and/or subsidence are larger than those driven by the viscous memory of late-Pleistocene deglaciation. Both spherical and flat-earth models are employed, the latter being used to exhaustively study the effects of glacial load history on the predicted vertical crustal velocity. Recent assessment of net mass balance from 1944 to 1985 indicates that the Southern Patagonian icefield (SPI) has significantly deteriorated due to snout retreat and thinning. Volume loss rates are estimated at about 3.4 - 9.3  $\text{km}^3/\text{yr}$  for the SPI. The predicted vertical isostatic response to this recession and to the modeled Holocene Neoglaciations is at a marginally detectable level (of order 1  $\text{mm}/\text{yr}$ ) if the mantle/asthenosphere beneath Patagonia is of the order of  $10^{21}$  Pa s. However, for reduced mantle viscosities, younger glacial load histories predict more substantial signatures. In fact, if the viscosity is about  $2 \times 10^{20}$  Pa s, or lower, then geodetically detectable vertical motion may be driven by a regional Little Ice Age (LIA) (1400 - 1750 AD) glacier advance and subsequent 20th century retreat. Although this value for mantle viscosity is lower than thought typical of continental shield mantle ( $\approx 10^{21}$  Pa s), it is, none-the-less, consistent with inversions for postseismic relaxation time constants in island arc environments and in regions with significant Neogene continental tectonism. In the viscosity regime,  $5 \times 10^{18}$  to  $2 \times 10^{19}$  Pa s, the predicted rates of vertical crustal motion are similar to those presently occurring in Fennoscandia and Hudson Bay (5 - 10  $\text{mm}/\text{yr}$ ). Geodetic data may be sensitive to the time integrated growth and subsequent retreat of NPI and SPI ice mass over the last 600 years in Patagonia.

**Key Words:** crustal movements, glacier change, mantle rheology, continental lithosphere, GPS geodesy.

**Short Title:** Glacial isostasy in southern Patagonia.

*glacial recession postglacial rebound*

## 1. Introduction.

Recent evaluation of the 20th Century mass balance of the Northern and Southern Patagonian Icefields (NPI and SPI, respectively) has concluded that both are in prolonged state of recession that continues into the present-day [Aniya 1988; Naruse *et al.* 1995; Aniya *et al.* 1996]. An impressive compilation of mass balance related information has been published and summarized by Aniya *et al.* [1997]. These include a wealth of satellite and airborne imagery that complement ground-based glaciological data. The study by Aniya *et al.* [1997] concludes that the total volume change for SPI during a time span covering 1945 to 1986 is roughly 140 to 380 km<sup>3</sup>. This rate of glacial recession is substantial, amounting to about 1/40 - 1/20th of that estimated by Meier [1984] ( $\approx 0.46 \pm 0.26$  mm/yr in sea level rise equivalent) due to recession of all the world's mountain glacier systems combined during the years 1900 to 1961. Crust beneath and adjacent to the current glacial retreat may be sustaining rapid vertical movement due to the solid Earth's elastic-gravitational response. These crustal responses might be occurring at geodetically detectable levels if high quality Global Positioning System (GPS) station data were to be employed.

The viscoelastic response of the Earth is a serious complication, however, since it allows past glacial advancement and/or retreat to affect the present-day crustal response signature. Fennoscandian and Hudson Bay uplift represent classic examples of the Earth's long-term memory of past glacial loading. A relatively well-documented Little Ice Age glacial advance [Mercer 1970, 1976, 1982; Rabassa & Clapperton 1990; Aniya 1995] of somewhat uncertain timing (circa 1400 - 1750 AD) and 2 - 3 additional Neoglacial oscillations of late Holocene age (1 - 5 ka BP) might be preserved in the viscously "sluggish" isostatic memory of the mantle/lithosphere.

The main goal of this paper is to examine the sensitivity of the predicted present-day vertical crustal response to three factors: (i) ongoing and well-documented 20th Century Patagonian glacial recession [Aniya 1988; Naruse *et al.* 1995; Aniya *et al.* 1997]; (ii) variations in viscoelastic Earth model parameters; (iii) pre-20th Century paleo-icefield reconstructions that can be partially constrained by <sup>14</sup>C dated moraine sequences. Toward this end a simple and computationally efficient method for calculation of the viscoelastic response with an elastic lithosphere and a Maxwell half-space is presented. The mathematical formulation follows that of Wolf [1985] and is well-suited to complex load histories. It will be shown that, although lithospheric thickness is important, the viscosity assumed for the half-space is the more fundamental mechanical parameter influencing the predictions of present-day vertical rates.

The Patagonian icefields are surrounded by a unique tectonic environment, one that has recently experienced the creation of a mantle slab window, left in the wake of the northward migration of the Chile Triple Junction and subduction of an active oceanic ridge during the past 12 Ma [Candie & Leslie 1986; Gorring *et al.* 1997]. High heat flow, late Tertiary-Quaternary volcanism and the subduction of ocean ridge segments during the past 15 million years [Hamza & Muñoz 1996; Gorring *et al.* 1997] suggest a mantle viscosity that should be substantially lower than 10<sup>21</sup> Pa s. We demonstrate that if the upper mantle viscosity is lower than that determined from analysis of raised beaches in Fennoscandia by factors of 15

to 100, then vertical motions caused by a "Little Ice Age" glacial rebound are large enough to be detected using space geodetic methods.

## 2. Observations of Glacier Fluctuation

The extent of the Northern and Southern Patagonian icefields is shown in Figure 1. Together the two temperate glacier systems form the third largest continental ice complex in the world, with only Greenland and Antarctica retaining greater hydrological mass [Naruse & Aniya 1992; Warren & Sugden 1993]. Dramatic changes in the Patagonian outlet glacier system have been documented since the beginning of historical record taking [Warren 1993; Warren & Sugden 1993]. Within the past decade new quantitative estimates of the rate of volume changes of both the NPI [Aniya 1988] and SPI [Aniya *et al.* 1997] have emerged. These studies have been spatially comprehensive. The section that follows gives a brief review of these important observations.

### 2.1 Mid to Late 20th Century Changes

Evaluation of mid to late 20th Century total mass balance of the Patagonian ice fields has been accomplished by using a combination of ground surveys and aerial photographs, including oblique Space Shuttle photos and cloud-free LANDSAT imagery of the NPI (January 22, 1979) and of the SPI (January 14, 1986). The results have been discussed in a series of papers by Aniya [1988], Naruse *et al.* [1995] and Aniya *et al.* [1996;1997]. Here a total of 48 outlet glaciers of SPI were examined utilizing a series of U.S. Army Air Force oblique photographs taken during the summer of 1944/1945 as a basis for comparison to glacial extent of the summer of 1985/1986. While several SPI glaciers were found to be in near equilibrium, and two in a state of advancement, 33 glaciers of the SPI glaciers show loss in area at an average rate of  $0.192 \text{ km}^2/\text{yr}$  while a similar study of NPI shows a loss rate of  $0.044 \text{ km}^2/\text{yr}$  [Aniya *et al.* 1997]. By obtaining a number of thickness estimates at the retreating snout of outlet glaciers an approximate volume estimate could be calculated. Some glacial thinning estimates were made from combined aerial photography and field observation, ranging from below 1 m/yr to a maximum of 4 m/yr averaged over 41 years. Aniya *et al.* [1997] conclude that the volume loss in the SPI over a 41 year time span by snout retreat is 40 to 80  $\text{km}^3$  while that associated with thinning is roughly 100 to 300  $\text{km}^3$ . The pace of glacial recession in the SPI seems to have accelerated after the mid-1970's according to Aniya *et al.* [1997]. No analogous volume loss estimates for the NPI have yet been published.

Atmospheric moisture that sustains icefield growth is derived almost exclusively from the prevailing Southern Westerlies. Pleistocene and Recent glacial fluctuation is, therefore, intimately connected to the moisture content, temperature, zonal position and intensity of these Westerlies [Heusser 1989; Hulton *et al.* 1994]. Atmospheric temperature variation may be of significance to both the growth and shrinkage of the icefields over centennial time scales. Numerical simulation of the shrinkage of the Franz Joseph Glacier in New Zealand over the last 150 years by Oerlemans [1997] indicates that a secular warming of 0.6

°C per century could account for the observed recession from moraine maxima at 1750 - 1820 AD. A model of Patagonian glacial recession during the 20th Century developed by *Naruse et al.* [1995] suggests that rise in the equilibrium-line altitude of 100 m (perhaps corresponding to a 1-2 °C increase in air temperature) could explain the observed retreat of Upsala and Moreno glaciers in the SPI (see Figure 1). The characteristic time for glacial mass response for alpine glaciers at this latitude is fairly short, about 15 years according to *Oerlemans* [1997], implying that Holocene volume changes of the Patagonian icefields are probably indicative of climate changes (also see *Warren* [1993]).

## 2.2 Late Holocene (0 - 5 ka BP) Moraine Advances and Retreats

### 2.2.1 Little Ice Age (LIA)

Mean surface air temperature in the southern Hemisphere appear to follow the basic 0.5 - 0.7 °C warming trend over that past 100 - 150 years that is observed in the northern Hemisphere [*Jones, Raper & Wigley* 1986; *Hansen & Lebedeff* 1987]. Temperature records in the latitude band from 44.4 °S to 64.2 °S show an average surface air temperature increase of  $0.9 \pm 0.3$  °C from 1880 to 1940, but the number and quality of the reporting stations makes inferences inadvisable according to *Hansen & Lebedeff* [1987]. In Patagonia any local correlation of temperature and glacier volume change cannot be made [*Warren & Sugden* 1993]. However, very clear evidence for glacial advancement during the Little Ice Age (LIA) in Patagonia is found in the form of datable moraines. *Mercer* [1970; 1976] dated both forest trimlines and moraine debris and determined widespread glacial maxima to have occurred during the mid-18th and mid-19th centuries. The data includes a strongly tilted cypress tree found in the northwestern section of the SPI that dates the maximum advancement of the Tempano glacier to the year AD  $1760 \pm 10$  [*Mercer* 1970]. Glacial moraines outside the Patagonian icefields show a somewhat coincident advancement during the LIA both in the Andean mountains to the north [*Clapperton & Sugden* 1988] and in the sub-Antarctic islands to the south [*Clapperton & Sugden* 1983]. Mid-18th Century advancement of the San Rafael glacier, and subsequent recession initiated in 1880, has been documented in historical records [*Warren* 1993]. Unfortunately, many of the dendrochronological temperature reconstructions for Patagonia show no consistent pattern of cold conditions since AD 1500 with the exception of the years AD 1532-1538 and 1563-1562 [*Boninsegna* 1995]. An analysis of tree ring records near the northern edge of the NPI, however, reveal evidence of an extended period of cold-moist conditions from AD 1280-1670 with this trend peaking at AD 1340 and again at 1650 [*Villalba* 1990]. For the purpose of computing present-day isotatic signature we will take the LIA in Patagonia to be bracketed in time by AD 1400-1880.

### 2.2.2 Neoglacial Moraine Record

Advances of outlet glaciers of the SPI and the NPI were dated at the ancient terminal moraines along both the western and eastern flanks of the southern Andes. The dates of various organic materials tend to yield minimum ages only, thus, the derived chronologies must be accepted with some uncertainty. *Mercer* [1970; 1976; 1982] proposed three Neoglacial advances since 5 ka BP based upon moraine dates along the northwestern margins of the SPI. The first was dated to 4.7-4.2 ka and a second to 2.7-2.0 ka BP. The third coincided with the LIA as discussed above. *Aniya* [1995] later analyzed data from moraines of the Tyndall and Upsala glaciers (see Figure 1) and concluded that there have been four late Holocene Neoglacial advances, each maxima being achieved at about 3.6, 2.3, 1.6-1.4 and 0.3 ka BP. The evidence for the 3rd Neoglacial includes a  $^{14}\text{C}$  date from a standing *Nothofagus* stump near a terminal moraine of the Tyndall glacier. Both the Neoglacial scenarios suggested by *Mercer* [1970] and by *Aniya* [1995] will be examined to test their potential influence on present-day glacial rebound.

In Figure 2 an approximate method is shown for accounting for the scenarios of late-Holocene Neoglaciation and Last Glacial Maximum (LGM). Here the total volume of ice is shown as a function of time for two scenarios, similar to that of [*Mercer* 1970; 1976; 1982] (Type 1) and the other reminiscent of that proposed by *Aniya* [1995] (Type 2). An early Neoglacial at 4.5 ka BP corresponds to numerous minimal age dates reported by *Mercer* [1970; 1976; 1982] and coincides with regional cooling trends suggested by *Heusser & Streeter* [1980]. The palynological record indicates that the period 13 - 5 ka was marked by warm temperatures [*Heusser & Streeter* 1980; *Rabassa & Clapperton* 1990], punctuated only at 11-10 ka BP by a Younger Dryas-like cold epoch [*Heusser et al.* 1996]. *Rabassa & Clapperton* [1990] suggest that the icefields may have been substantially smaller during 13-5 ka than at the present-day.

Estimates of the total Neoglacial volume change,  $\Delta V \equiv V_{\text{max}} - V_{\text{min}}$ , can only be made in fairly crude manner. These estimates are given in Section 6. A preliminary study found that the assumption of equivolume changes for each Neoglacial period was sufficient for parameterizing the load, at least as it affected the prediction of present-day isostatic uplift rate.

### 2.3 Last Glacial Maximum (LGM)

During the 100,000 years major glaciation of the Andes south of 36 °S probably involved at least 3 separate maxima [*Porter* 1981; *Clapperton & Sugden* 1988; *Rabassa & Clapperton* 1990; *Clapperton et al.* 1995]. During a period when the Northern Hemispheric ice sheets were in rapid collapse (15 - 14 ka), Patagonian glacier advance ceases and subsequent retreat is rapid, with the region being substantially deglaciating by 13 ka [*Rabassa & Clapperton* 1990]. For modeling purposes we found it sufficient to assume the volume changes and timing of late Pleistocene Patagonian deglaciation that are given by *Tushingham & Peltier* [1991] in model ICE-3G, in spite of its relatively early completion of retreat at 15 ka. It can be easily demonstrated that inclusion of a 11-10 ka readvance has a negligible contribution to present-day crustal motion signature. The total volume of ice lost during deglaciation from LGM, as portrayed in

ICE-3G, is  $\Delta V_{LGM} \approx 1.8 \times 10^5 \text{ km}^3$ . A sophisticated numerical simulation of Patagonian LGM by *Hulton et al* [1994] finds that ice sheet growth may be somewhat larger:  $\Delta V_{LGM} \approx 4.4 \times 10^5 \text{ km}^3$ . Neoglacial oscillations represent a small fraction of the volume lost from 21 to 13 ka.

### 3. Motivation for a Simplified Earth Model with Complex Load Pattern and History.

Over the past 30 years a series of increasingly sophisticated global glacio-isostatic models have been employed to explain the  $^{14}\text{C}$ -dated paleoshoreline record. Mantle viscosity structure plays a prominent role in such models, for it controls, to a significant extent, the timing, pattern and magnitude of postglacial isostatic land emergence and subsidence [e.g., *Walcott* 1970; *Peltier* 1976; *Lambeck* 1993]. Mantle viscosity plays a vital role since the time scales for global deglaciation phenomena ( $\approx 10^3 - 10^4 \text{ yr}$ ) and viscous-gravitational relaxation ( $\approx 10^2 - 10^4 \text{ yr}$ ) overlap. Simple models of the viscously lagged isostatic response are useful when the underlying concern is over the spatial pattern, total hydrological mass and chronology of a region having poorly constrained glacial history. By considering the mantle structure to be known, ice load models may be sought by iteration with the goal of fitting local land emergence records. For example, using a simple parameterization of the viscous isostatic response, *Broecker* [1966] interpreted carbon 14 dated paleoshorelines of proglacial lakes with the intent of deriving first order constraints on ice sheet geometry during Laurentide advancement and retreat. One drawback of the latter approach is a lack of wavelength sensitivity in the exponential response times, and this is a severe limitation when the load has geometrical complexity.

Most simple models assumed by glacio-geomorphologists are in stark contrast to the sophisticated treatments developed for analysis of global postglacial shoreline data [e.g., *Peltier* 1974; 1976; 1994; *Mitrovica & Peltier* 1991; *Lambeck* 1993]. In this paper we develop a semi-analytical approach that retains the essentials of Maxwellian viscoelastic gravitational relaxation and apply this method to the retreat and readvance of the Patagonian glacier fields during the late Holocene. The model and method offer a compromise between the sophisticated global spherical models and those that assume a single mode, viscously lagged, postglacial response, such as assumed by *Broecker* [1966]. The model also offers a more sophisticated approach than those models in current use for ice sheet modeling purposes (see a recent summary by *Huybrechts* [1992]). Using this simple numerical tool we may span both the viscosity and lithospheric thickness parameter space along with a spatially detailed and temporally varying ice load. The predicted uplift signature for Patagonia due to 20th century glacial recession is significant ( $\dot{h} \geq 4 \text{ mm/yr}$ ) over a quite plausible portion of the mantle viscosity and lithospheric thickness parameter space.

#### 4. Upper Mantle Rheology and Lithospheric Thickness

##### 4.1 Laterally Heterogeneous Upper Mantle and Lithosphere

The effective viscosity of the mantle, lithospheric thickness and elastic rigidity, in most simple continuum mechanical models, set the time scales for these gravity-driven isostatic responses [McConnell 1965; Walcott 1970; Peltier 1976]. Using the global sea level record Peltier [1976; 1994] has constrained spherically symmetric, radially varying, viscosity models of the mantle. Although such models provide a global average, Nakada & Lambeck [1991], Ivins & Sammis [1995], Kaufmann & Wolf [1996], Giunchi, Spada & Sabadini [1997], and others, have emphasized that the strength of lateral heterogeneity in the upper mantle probably exceeds one order of magnitude in viscosity variability and that regional estimates must account for continental-scale tectonic environment. Models for sea level change and time-dependent shoreline evolution driven by the removal of glacial ice that covered northern Europe during glacial times (100 - 21 kyr BP) provide some estimate of both the viscosity and lithospheric thickness beneath Fennoscandia. Recent modeling by Mitrovica [1996] indicates that the lithosphere beneath Fennoscandia is roughly 75 - 120 km thick and the upper mantle viscosity is bounded between about  $6.5$  to  $11.0 \times 10^{20}$  Pa s. Another analysis of Northern European LGM and subsequent ice retreat [Lambeck 1993] determined that an optimum fit to relative sea level changes along the coast of the British Isles corresponds to an elastic lithospheric thickness of 65 km and an upper mantle viscosity near  $4\text{--}5 \times 10^{20}$  Pa s. However, even lower upper mantle viscosity ( $1 - 2 \times 10^{20}$  Pa s) and thinner elastic lithosphere values (50 km) fit paleoshoreline data along the eastern coast of Australia [Nakada & Lambeck 1989] and analyses of glacio-isostatic rebound in Iceland, near an active oceanic spreading center, indicate a regional upper mantle viscosity lower than  $1 \times 10^{19}$  Pa s [Sigmundsson 1991]. Modeled postseismic [Matsu'ura & Iwasaki 1983] and glacio-hydroisostatic [Maeda et al. 1992] coastal tilting and rebound in the island arc setting of Japan indicate sublithospheric viscosity are also fairly low, in the range of  $2 \times 10^{19}$  to  $2 \times 10^{20}$  Pa s. It is important to note that the crustal deformation decay time scales set by such estimates of viscosity and lithospheric thickness for this island arc environment are similar to those corresponding to well-documented centennial and millennial scale climate changes such as the LIA.

##### 4.2 Patagonian Tectonic Framework

The Miocene and Plio-Pleistocene magmatic and tectonic history of Patagonia is characterized by the northward migration of the Chile Triple Junction and the progressive subduction of active ridge segments [Candie & Leslie 1986]. A substantial "slab window" has developed beneath Patagonia due to the oblique angle of this subduction [Gorring et al. 1997]. The implied thermo-rheologic weakening associated with both ridge subduction [Hsui 1981] and slab window evolution [Thorkelson 1996; Goes et al. 1997] suggest that the mechanical strength properties of the Patagonian lithosphere and upper mantle are more analogous to an island arc setting [Stern & Kilian 1996] than to a continental shield environment.

In this paper we present the results of a numerical modeling study that treats the lithosphere as an elastic layer and the upper mantle as a homogeneous Maxwell viscoelastic half-space. Both regions are hydrostatically pre-stressed. The governing equations are essentially the same as given by *Peltier* [1976] except that the geometry is simplified to a cylindrical coordinate frame and material compressibility along with certain self-gravitational terms are ignored. The system of equations of motion was given extensive treatment by *Wolf* [1985a] and the numerical procedures adopted here are similar to this later study. The efficiency of these procedures allow an extensive investigation of the icefield load history to be undertaken. It is assumed that the last Pleistocene ice age sets the viscoelastic gravitational conditions (amounting to a slight deviation from isostatic equilibrium by mid-Holocene time) for subsequent responses to ice volume oscillations during the late Holocene ( $\leq 5$  ka). This era of glacial readvances in the region are termed "Neoglacial" by *Mercer* [1970]. The last of these advances may have a causal link to the lower world-wide temperatures during the Little Ice Age (e.g., *Thompson et al.* [1986]). Subsequent retreat, known to be underway by 1880-1900 [*Warren* 1993], may possibly be linked to a global warming trend since 1850 [*Jones et al.* 1986]. We now give a complete accounting of the simple theory for the solid Earth deformation.

## 5. Theory

### 5.1 Equations of Motion and Reduction to an O.D.E. Form

Within a layer of constant density,  $\rho$ , the perturbation equations for the displacement field,  $\mathbf{u}$ , and stress tensor,  $\boldsymbol{\tau}$ , are

$$\nabla \cdot \boldsymbol{\tau} + \rho g \nabla (\mathbf{u} \cdot \mathbf{k}) = 0, \quad (1)$$

where  $g$  is gravity acting parallel to the unit vector  $\mathbf{k}$  of the positive (downward directed)  $z$ -axis in a cylindrical coordinate system  $(r, z, \theta)$ . For axisymmetric loading and assuming lateral homogeneity, the Eulerian displacement is

$$\mathbf{u} = u(r, z, t) \mathbf{r} + w(r, z, t) \mathbf{k} \quad (2)$$

with  $\mathbf{r}$  the unit vector in the radial direction. If the lithosphere and mantle are elastic, then time,  $t$ , does not enter as an independent variable. For isotropic elasticity,

$$\boldsymbol{\tau} = (\kappa^e - \frac{2}{3} \mu^e) \text{tr} \{ \boldsymbol{\varepsilon} \} \mathbf{I} + 2 \mu^e \boldsymbol{\varepsilon} \quad (3)$$

where  $\text{tr} \{ \boldsymbol{\varepsilon} \}$  is the trace of the deformation tensor,  $\mathbf{I}$  is the identity tensor, and  $\kappa^e$  and  $\mu^e$  are the bulk and shear moduli, respectively. The  $r$  and  $z$  components of the equation of motion (1) are then

$$\frac{\partial \tau_{rr}}{\partial r} + \frac{\partial \tau_{rz}}{\partial z} + \frac{(\tau_{rr} - \tau_{\theta\theta})}{r} + \rho g \frac{\partial w}{\partial r} = 0 \quad (4a)$$

$$\frac{\partial \tau_{rz}}{\partial r} + \frac{\partial \tau_{zz}}{\partial z} + \frac{\tau_{rz}}{r} + \rho g \frac{\partial w}{\partial z} = 0 \quad (4b)$$



The stress-strain relations in cylindrical coordinates allow for some simplification of (4a). In particular,

$$\frac{\partial \tau_{rr}}{\partial r} + \frac{\partial \tau_{rz}}{\partial z} + \frac{(\tau_{rr} - \tau_{\theta\theta})}{r} = 2 \mu^e (\varepsilon_{rr} - \varepsilon_{\theta\theta}) + (\kappa^e - \frac{2}{3} \mu^e) \left[ \frac{1}{r} \frac{\partial(ru)}{\partial r} + \frac{\partial w}{\partial z} \right], \quad (5)$$

where  $\varepsilon_{rr}$  and  $\varepsilon_{\theta\theta}$  are strain components in cylindrical coordinates. Use of explicit relations for the latter strain components, stress-strain relations for  $\tau_{zz}$  (for example, see Jaeger [1969] p. 61-62) and the following relation derived from (5);

$$\frac{\partial w}{\partial z} = \frac{2 \mu^e - 3 \kappa^e}{4 \mu^e + 3 \kappa^e} \frac{1}{r} \frac{\partial(ru)}{\partial r} + \frac{3}{4 \mu^e + 3 \kappa^e} \tau_{zz}, \quad (6)$$

allows (4a) to be rewritten as

$$\begin{aligned} \frac{\partial \tau_{rz}}{\partial r} + \frac{3 \kappa^e - 2 \mu^e}{4 \mu^e + 3 \kappa^e} \frac{\partial \tau_{zz}}{\partial z} + \\ \frac{4 \mu^e (3 \kappa^e + \mu^e)}{4 \mu^e + 3 \kappa^e} \left( \frac{\partial^2}{\partial r^2} + \frac{1}{r} \frac{\partial}{\partial r} - \frac{1}{r^2} \right) u + \rho g \frac{\partial w}{\partial r} = 0. \end{aligned} \quad (7)$$

The first order Hankel transform of (7) is defined by the integral operator;

$$\hat{f}_1(k) \equiv H_1 \left[ f(r); k \right] \equiv \int_0^\infty r f(r) J_1(kr) dr \quad (8)$$

where the operator notation  $H_1$  follows that of Sneddon [1972]. Using transformation (8) on (7) yields

$$\begin{aligned} \frac{\partial \hat{\tau}_{z1}}{\partial z} - \frac{3 \kappa^e - 2 \mu^e}{4 \mu^e + 3 \kappa^e} k \hat{\tau}_{z0} - \\ \frac{4 \mu^e (3 \kappa^e + \mu^e)}{4 \mu^e + 3 \kappa^e} k^2 \hat{u}_1 - \rho g \hat{w}_0 = 0. \end{aligned} \quad (9)$$

In (9) the zeroth order Hankel transform has been introduced, where

$$\hat{f}_0(k) \equiv H_0 \left[ f(r); k \right] \equiv \int_0^\infty r f(r) J_0(kr) dr, \quad (10)$$

with  $J_0(kr)$  and  $J_1(kr)$  are zeroth and first order Bessel functions, respectively. Dependent variables transformed by these two integral operators correspond to notation of forms:  $\hat{\cdot}_0$  and  $\hat{\cdot}_1$ , respectively. Applying the operator (10) to (4b) yields

$$\frac{\partial \hat{\tau}_{z0}}{\partial z} + k \hat{\tau}_{z1} + \rho g \frac{\partial \hat{w}_0}{\partial z} = 0. \quad (11)$$

Hankel transforms of derivative terms in  $r$  are provided by Sneddon [1972]. Let us confine the remaining development to the incompressible case for which  $\kappa^e \rightarrow \infty$ . In this case the following holds:

$$\frac{1}{r} \frac{\partial(ru)}{\partial r} + \frac{\partial w}{\partial z} = 0, \quad (12)$$

and this allows (9) to simplify to the form

$$\frac{\partial \hat{\tau}_{rz1}}{\partial z} - k \hat{\tau}_{zz0} - 4 \mu^e k^2 \hat{u}_1 - \rho g \hat{w}_0 = 0 \quad (13)$$

The zeroth order transform of (12);

$$\frac{\partial \hat{w}_0}{\partial z} + k \hat{u}_1 = 0 \quad (14)$$

and the first order Hankel transform of the stress-strain relation for  $\tau_{rz}$ ;

$$\frac{\partial \hat{u}_1}{\partial z} - k \hat{w}_0 - \frac{1}{\mu^e} \hat{\tau}_{rz1} = 0 \quad (15)$$

with (11) and (12) then provide a coupled system of ordinary differential equations in the dependent variables;  $\hat{u}_1(z,k)$ ,  $\hat{w}_0(z,k)$ ,  $\hat{\tau}_{rz1}(z,k)$  and  $\hat{\tau}_{zz0}(z,k)$ . The system (11) through (14) is identical to that derived by *Wolf* [1985a].

## 5.2 Gravitational Forces

A key element was retained by *Wolf* [1985a, b] in comparison to an earlier treatments of the axisymmetric elastic half-space problem in a cylindrical coordinate system by *Farrell* [1972]. In particular, the term in (1) involving gravity and vertical displacement arises from the advection of initial hydrostatic prestress [*Vermeersen & Vlaar* 1991]. Its existence allows gravitational restoring forces to act at any density interface, such as the interface between the Earth's rock crust and the atmosphere or ocean. In the elastic problem, wherein (11), (13), (14) and (15) represent the static equilibrium conditions, gravity may play a fairly minor role [*Ward* 1984]. However, when solid-state creep processes become important, as in the case of glacial time-scales, a physical description of isostasy and its time-evolution absolutely require this term. In effect, the gravitational buoyancy term allows for restoration of isostatic equilibrium after either loading or unloading events have ceased. This fact was discussed in the viscoelastic analogue of the well-known Boussinesq solution for an impulsive load by *Peltier* [1974].

For the elastic equilibrium equations (11), (13), (14) and (15), *Wolf* [1985b] recognized that the form of the matrix differential system was identical to that of *Farrell* [1972], provided the stress variable  $\hat{\tau}_{zz0}$  is modified to

$$\delta \hat{\tau}_{zz0} \equiv \hat{\tau}_{zz0} + \rho g \hat{w}_0 \quad (16)$$

## 5.3 Viscoelastic Solution for the $i$ th Layer

The correspondence principle of linear viscoelasticity allows the solution to be recovered from that of the elastic equations. This requires Laplace transformation to the variable  $s$ , and replacement of  $\mu^e$  by  $\mu(s)$  in the equilibrium equations. Henceforth, we assume the viscoelastic system with solution for the  $i$ th homogeneous layer:

$${}_i\hat{u}_1(z, s, k) = -A_i e^{kz} + B_i e^{-kz} + kz C_i e^{kz} + kz D_i e^{-kz}, \quad (17a)$$

$${}_i\hat{w}_0(z, s, k) = A_i e^{kz} + B_i e^{-kz} - (kz - 1) C_i e^{kz} + (kz + 1) D_i e^{-kz}, \quad (17b)$$

$${}_i\hat{\tau}_{rz1}(z, s, k) = \quad (17c)$$

$$2k {}_i\mu(s) \left[ -A_i e^{kz} - B_i e^{-kz} + kz C_i e^{kz} - kz D_i e^{-kz} \right],$$

$${}_i\delta\hat{\tau}_{zz0}(z, s, k) = \quad (17d)$$

$$2k {}_i\mu(s) \left[ A_i e^{kz} - B_i e^{-kz} - (kz - 1) C_i e^{kz} - (kz + 1) D_i e^{-kz} \right].$$

The equivalent of (17) is given by *Wolf* [1985b], although his eq. 2a and 2b, contain some typographical errors.

#### 5.4 Boundary Conditions and Solution for a Two-Layer System

While solutions (17a) through (17d) are appropriate to an N-layered half-space, we now use these to construct a model that describes the surface deformation of a two-layered system. The top layer corresponds to  $i = 1$  and the half-space to  $i = 2$ . The surface of the top layer is loaded by finite stress load,  $q$ , that represents the downward directed force on the solid Earth at the base of an ice sheet. This force is balanced by the finite material strength of the crust, so that

$${}_1\hat{\tau}_{zz0}(0, s, k) = -\hat{q}_0(s, k) \quad (18a)$$

where the load is assumed axisymmetric and  $\hat{q}_0$  now is assumed to be in both the Laplace and zeroth order Hankel transform space, as indicated by the dependencies upon  $s$  and  $k$  in (18). The ice sheet will be assumed to cause negligible transverse stresses, hence

$${}_1\hat{\tau}_{rz1}(0, s, k) = 0. \quad (18b)$$

Together, (18a) and (18b) represent the required boundary conditions at the ice-rock interface. Note, however, that (18a) is not expressed in terms of our dependent variables of the solution (17a -d). Both of the cylindrical stress components  $\tau_{r\theta}$  and  $\tau_{\theta\theta}$  vanish everywhere in the space due to the assumed axisymmetry. It is convenient to reconsider the unmodified vertical stresses,  $\hat{\tau}_{zz0}$ , for completion of the solution. For a two-layer system the complete solution in the transform domain is obtained by solving for the unknown constant coefficients,  $A_1, B_1, C_1, D_1, A_2, B_2, C_2$  and  $D_2$ . Conditions of finite behavior as  $z \rightarrow \infty$  demands that  $A_2 = C_2 = 0$ . The two stress conditions (18a) and (18b) can be used to eliminate two of the constants for the top layer solution. Use of the modified vertical stresses (16) in (18a) is facilitated by the simplicity of  ${}_1\hat{w}_0$  at  $z = 0$ , noting that

$${}_1\hat{w}_0(0, s, k) = A_1 + B_1 + C_1 + D_1. \quad (19)$$

Additionally, it is convenient to write the unmodified stress as

$${}_1\hat{\tau}_{zz0} = A_1\phi_1 e^{kz} - B_1\chi_1 e^{-kz} + (1 - kz) C_1\phi_1 e^{kz} - (kz + 1) D_1\chi_1 e^{-kz} \quad (20)$$

where

$$\chi_1 \equiv 2k\mu_1 + \rho_1 g, \quad (21a)$$

and

$$\phi_1 \equiv 2k\mu_1 - \rho_1 g. \quad (21b)$$

Equation (2) allows the stress continuity conditions to be readily applied at the interface,  $z = h$ , between top layer and the half-space. The latter conditions are

$${}_1\hat{\tau}_{zz0} = {}_2\hat{\tau}_{zz0} \quad (22a)$$

and

$${}_1\hat{\tau}_{rz1} = {}_2\hat{\tau}_{rz1} \quad (22b)$$

and the displacement conditions at this interface are

$${}_1\hat{w}_0 = {}_2\hat{w}_0, \quad (22c)$$

$${}_1\hat{u}_1 = {}_2\hat{u}_1. \quad (22d)$$

From the surface conditions (18a) and (18c) it can be easily shown that

$$D_1 = (\hat{q}_0 + 4k\mu_1 A_1 + \phi_1 C_1) / \chi_1 \quad (23a)$$

$$B_1 = -A_1 \quad (23b)$$

and, consequently, the four conditions at  $z = h$ , (22a-d) form a  $4 \times 4$  linear system for the constants  $A_1$ ,  $C_1$ ,  $B_2$  and  $D_2$ . Such a system can be solved analytically. Below we combine only those parts of such a solution that are required for obtaining the uplift/subsidence at the surface  $z = 0$ .

### 5.5 Surface Vertical Displacement Solution

Upon obtaining the solution for the linear system, the remaining constants  $B_2$ ,  $D_2$ ,  $A_1$  and  $C_1$  are eliminated and a complete solution in  $z$  is obtained. The vertical displacement solution  ${}_1\hat{w}_0$  takes the simple form;

$$(2k\mu_1 + \rho_1 g) {}_1\hat{w}_0 = 4k\mu_1 (A_1 + C_1) + \hat{q}_0 \quad (24)$$

where the sum  $A_1 + C_1$  is

$$\frac{A_1 + C_1}{\hat{q}_0} = \left\{ 2k\mu_1^2 \left\{ 2k \left[ 1 + e^{4kh} + 2e^{2kh} (1 + 2k^2 h^2) \right] \cdot \mu_1 \right. \right. \quad (25)$$

$$\left. \left. - g\rho_1 (1 - e^{4kh} + 4kh e^{2kh}) \right\} \right\}$$

$$\begin{aligned}
& + \mu_2 \left\{ -8 k^2 (1 - e^{kh}) (1 + e^{kh}) (1 + e^{2kh}) \mu_1^2 \right. \\
& + 2 k g \left[ (\rho_1 + \rho_2) (1 + e^{4kh}) + 2 (\rho_2 - \rho_1) e^{2kh} (1 + 2 k^2 h^2) \right] \cdot \mu_1 \\
& \quad \left. - \rho_1 g^2 (\rho_2 - \rho_1) (1 - e^{4kh} + 4 kh e^{2kh}) \right\} \\
& + 4 k^2 \mu_1^3 (1 - e^{2kh} - 2 kh e^{kh}) (1 - e^{2kh} + 2 kh e^{kh}) \\
& \quad - 2 k g \rho_2 \mu_1^2 (1 - e^{4kh} - 4 kh e^{2kh}) \\
& \quad + g^2 \rho_1 (\rho_2 - \rho_1) \mu_1 (1 - e^{kh})^2 (1 + e^{kh})^2 \Big]^{-1} \cdot \\
& \left[ -2 k \mu_2^2 \left\{ 1 + e^{2kh} \left[ 1 + 2 kh (1 + kh) \right] \right\} \right] \\
& + \mu_2 \left\{ 4 k \mu_1 - g (\rho_2 - \rho_1) \left[ 1 + e^{2kh} \left[ 1 + 2 kh (1 + kh) \right] \right] \right\} \\
& \quad + \mu_1^2 \left\{ 2 k \left[ (e^{2kh} - 1) + 2 kh e^{2kh} (1 + kh) \right] \right\} \\
& \quad + \mu_1 g (\rho_2 - \rho_1) \left[ 1 - e^{2kh} (1 + 2 kh) \right] \Big] .
\end{aligned}$$

Note in (25) that the rheological parameters,  $\mu_1$  and  $\mu_2$ , are isolated in each part of the expression. For either of the limits  $\rho_2 \rightarrow \rho_1$ ,  $\mu_2 \rightarrow \mu_1$  or  $h \rightarrow 0$ , corresponding to the half-space limit [Wolf 1985a], the correct limit  $A_1 + C_1 \rightarrow 0$  is obtained.

## 5.6 Decay Spectra $\gamma_p$

In equation (25) both  $\mu_1$  and  $\mu_2$  might be considered viscoelastic due to fluid poroelastic and/or low temperature creep in the crustal/lithospheric environment of layer 1 or due to high temperature creep in the lower crust and/or mantle environment (layer 2). Although the upper crust may maintain a finite short-term viscoelasticity [Ivins 1996], a long-term, high-temperature creep deformation in layer 2 (half-space) dominates the total strain field associated with centennial and millennial time-scale isostatic responses due to hydrological and sedimentary depositional transport. Our assumption is that the rheologies of regions 1 and 2 shown in Figure 3 correspond to a constant elastic rigidity

$$\mu_1 = \mu_1^e \quad (26a)$$

for the surface layer, and to a Maxwell material

$$\mu_2 = \frac{\tau_{MX} s}{1 + \tau_{MX} s} \cdot \mu_2^e \quad (26b)$$

for the half-space. Here  $\mu_1^f$  and  $\mu_2^f$  correspond to the instantaneous elastic shear moduli. Equation (26b) introduces  $\tau_{MX}$ , the Maxwell time, equal to the ratio of long-term effective viscosity  $\eta$  to short-term elastic modulus  $\mu_2^f$ . The latter represents the  $1/e$ -folding time for the transition to viscous creep dominated deformation. Equation (25), coupled with the simple material parameters of (26a) and (26b), affords an extremely straightforward computation of analytic decay times. Expressions for the two decay times of the two-layer incompressible deformation are relegated to Tables 1 and 2. These free decay eigenvalues,  $\gamma_p$ , are recovered from the inverse Laplace transform of equation (24). Figure A-1 of Appendix A shows the inverse decay times,  $\gamma_p$ , as a function of Hankel wave number  $k$  assuming a 100 km thick elastic layer and a half-space viscosity of  $\eta = 0.75 \times 10^{21}$  Pa s. A study of the mode and amplitude structure of a layered incompressible Maxwell Earth model by *Wolf* [1985b] demonstrated, quite unequivocally, that the two modes are sensitive to the combined effects of load evolution and lithospheric thickness. *Peltier* [1976] discussed these modes using the terminology C0, M0 and L0 for 'core', 'mantle' and 'lithosphere' dominated gravitational response. *Wolf* [1984] performed a comparison of spherical and half-space M0 and L0 structure and demonstrated that sphericity might be safely neglected for loads of radii less than  $1/10$  of the Earth's radius. Modes M0 and L0 account for the wavelengths associated with both elastic bending of the lithosphere and slow viscous relaxation of the mantle.

### 5.7 Laplace Transform Inversion $L^{-1}$

Analytic expressions for the time-dependent vertical displacement may be found in Hankel transform domain. Let  $\hat{B}(k, s) \equiv (A_1 + C_1)/\hat{q}_0$  in equation (24) and, from (25), this can be placed in the form

$$\hat{B}(k, s) = (a_2 s^2 + a_1 s + a_0)/(s^2 + b_1 s + b_0) \quad (27)$$

The inverse Laplace transform is found readily as

$$L^{-1} \hat{B}(k, s) = \sum_{p=1}^2 \frac{(-1)^p}{\gamma_2 - \gamma_1} e^{-\gamma_p t} \cdot \left[ \gamma_p (a_1 - a_2 \gamma_p) - a_0 \right] + a_2 \delta(t) \quad (28)$$

where  $\delta(t)$  is the Dirac delta function. The analytic solutions for inverse relaxation times  $\gamma_p$  are given in terms of the Earth structure-dependent coefficients  $a_0, a_1, a_2, b_0$  and  $b_1$  are given in Tables 1 and 2. A convolution with the load  $\hat{q}_0$  requires use of the Faltung theorem such that

$$L^{-1} \left\{ \hat{B}(k, s) \hat{q}_0(k, s) \right\} = \int_0^t \hat{B}(k, t - \tau) \hat{q}_0(k, \tau) d\tau \quad (29)$$

Separating the spatial and time-dependence of the load so that

$$\hat{q}_0 = \hat{q}_0^*(k) \cdot \hat{q}_0^{**}(t) \quad (30a)$$

and letting the surface load part  $\hat{q}_0^{**}$  be approximated as piece-wise continuous with  $J$  linear segments

$$\hat{q}_{0j} = \bar{m}_j t + \bar{b}_j \quad (30b)$$

where  $\hat{q}_0^*$  is that part associated with the Hankel wave number of the load,  $k$ . Examples of the

decomposition (30b) are shown in Figure 4. The amplitude factors  $\xi_p$  for the free decay solution are defined from (28) as given in Table 2. At the termination of the  $j$ th interval, the contribution to the convolution from the interval has the simple form

$$\begin{aligned} \hat{Q}_j(k, t) = & \sum_{p=1}^2 \frac{\bar{b}_j \xi_p}{\gamma_p} \left[ e^{\gamma_p(t_j - t)} - e^{\gamma_p(t_{j-1} - t)} \right] \\ & - \frac{\bar{m}_j \xi_p}{\gamma_p^2} \left[ (1 - \gamma_p t_j) e^{\gamma_p(t_j - t)} - (1 - \gamma_p t_{j-1}) e^{\gamma_p(t_{j-1} - t)} \right] . \end{aligned} \quad (31)$$

At the termination of  $J$  linearly evolving intervals, and for all  $t > t_J$ , where  $t_J$  is end-time of the final linear segment, the complete convolution is

$$\mathbf{L}^{-1} \left\{ \hat{B}(k, s) \hat{q}_0^{**}(s) \right\} = \sum_{j=1}^J \hat{Q}_j(k, t) , \quad (32)$$

wherein the Earth is initially unloaded and in hydrostatic-gravitational equilibrium with  $\bar{b}_1 = t_0 = 0$ . An example of a linear load height history is shown in Figure 4. Note that the memory effect of any  $j$ th interval is captured by the terms  $e^{\gamma_p(t_j - t)}$ . For example, the most recently "memorized" event has a  $1/e$ -folding time proportional to the time elapsed from the last portion of load evolution between  $t_{j-1}$  to  $t_j$ . For loads,  $\hat{q}_0$ , that have finite evolution during the evaluation time  $t$  the convolution (29) must include the last terms of (24) and (28), respectively. Employing the appropriate integral relations [Dirac 1958, p. 59] and modifying  $\hat{Q}_j$  of (32) for the  $J$ -th interval to

$$\begin{aligned} \hat{Q}_J(k, t) = & (a_2 + 1/4 k \mu_f^e) (\bar{m}_J t + \bar{b}_J) \\ & + \sum_{p=1}^2 \frac{\xi_p}{\gamma_p^2} \left\{ \gamma_p \bar{b}_J + \bar{m}_J (t \gamma_p - 1) - \left[ \gamma_p \bar{b}_J + \bar{m}_J (t_{J-1} \gamma_p - 1) \right] e^{\gamma_p(t_{J-1} - t)} \right\} \end{aligned} \quad (33)$$

with  $t_{J-1} \leq t \leq t_J$ . The modified term is of importance for computing the partly viscoelastic and partly elastic rebound occurring beneath the basement rock of an ice sheet whose mass balance evolves up to and including the present-day. Note the sensitivity to the slope of the linear load evolution,  $\bar{m}_J$ , for time derivatives of (33) which largely control the prediction of vertical rates at time  $t$ .

### 5.8 Hankel Transform Inversion $\mathbf{H}_0^{-1}$

The case of a cylindrical load with perfectly square edges centered at  $r = 0$  with form

$$q^*(r) = \begin{cases} 0 & r > \alpha \\ 1/2 & r = \alpha \\ 1 & r < \alpha \end{cases} \quad (34a)$$

has the forward transform  $\mathbf{H}_0$ ;

$$\mathbf{H}_0 \left\{ q^*(r) \right\} = \hat{q}_0^*(k) = \frac{\alpha}{k} J_1(k \alpha) . \quad (34b)$$

The case of an ellipsoidal cross-section has the form

$$q^*(r) = \begin{cases} 0 & r > \alpha \\ \sqrt{\alpha^2 - r^2} & r \leq \alpha \end{cases} \quad (35a)$$

and has the forward transform  $H_0$ ;

$$H_0 \left\{ q^*(r) \right\} \equiv \hat{q}_0^*(k) = \frac{\alpha}{k} j_1(k\alpha) , \quad (35b)$$

where  $j_1$  is the spherical Bessel function of the first kind, of order one (see *Wolf* [1984] and *Farrell* [1972], respectively). In order to obtain the complete solution for an individual cylindrical disk load that is of constant radius  $\alpha$  and evolving in time with the approximation (30b), the inverse zeroth order Hankel transform  $H_0^{-1}$  must be computed. From (24), (27) and (32), the vertical displacement history is then;

$$w_0(r, t) = \int_0^\infty \frac{4 k \mu_1^f}{2 k \mu_1^f + \rho_1 g} \cdot \left[ \sum_{j=1}^J \hat{Q}_j(k, t) \right] J_1(k\alpha) \cdot \frac{\alpha}{k} J_0(kr) k dk \quad (36)$$

In practice, equation (36) must be solved numerically and it is useful to consider the following sampling for  $k$ . First, consider the smallest wave number to be comparable to the radius of the Earth,  $R$ , or

$$k \approx \frac{1}{R} .$$

However, much of the power in the deformation field is concentrated near the wave numbers associated with the surface load and elastic layer thickness [*McConnell* 1965; *Wolf* 1993]. The highest wave numbers sampled in the integral (36) must allow

$$k > \max \left\{ \frac{1}{\alpha}, \frac{1}{h} \right\} .$$

Introducing dimensionless time and length scales and integral wave number,  $n$ ,

$$t' = \tau_{MX}^{-1} t \quad w'_0 = h^{-1} w_0 \quad (37)$$

$$k' = hk = n h R^{-1} \quad \alpha' = h^{-1} \alpha$$

facilitates practical computation and the integral solution. Additionally, it is assumed that all stresses are scaled such that  $\tau_{ij} = \mu^e \tau'_{ij}$ . For  $h = 100$  km the range for  $k'$  is  $1.57 \times 10^{-2}$  ( $n \approx 1$ ) to  $32.0$  ( $n \approx 2048$ ). The high resolution is noteworthy as this is similar to a spherical harmonic model of degree and order 2048 [*Wolf*, 1984]. This sampling is capable of resolving horizontal structure of the uplift/subsidence field at  $10'$ , or at a wavelength comparable to 20 km. Sampling of  $k'$  may be tailored to shorter wavelengths. For example, a calculation for  $h = 50$  km may assume higher resolution with the same truncation at maximum  $k'$  by doubling the truncation parameter for  $n$ . All computations given in this paper assume Simpson's rule for the approximation to (36). Note that the vertical rates,  $dw_0(r, t)dt$ , can be computed from the derivative,  $d\hat{Q}/dt$ , in (32).



## 6. Models of Patagonian Holocene Fluctuation

### 6.1 Estimation of $\Delta V$ .

The total volume change,  $\Delta V$ , between times of maximum glacial advance and retreat can only be crudely estimated. The SPI and NPI cover about  $1.3 \times 10^4$  and  $0.42 \times 10^4$  km<sup>2</sup>, respectively. Rates of volume change during the period 1944 - 1985 are available only for the SPI. Estimates based on the SPI observations [Aniya *et al.* 1996;1997] are made for both the NPI and the smaller glacier system in the vicinity of the Magellan Strait. The strategy for generalizing to the latter systems minimizes the overall estimate of the total loading of the lithosphere in the Patagonian region.

Change in glacier area is readily deciphered from aerial photography and satellite imagery. By incorporating ground-based surveys and oblique aerial photography, Aniya *et al.* [1997] were able to estimate the volume loss due to thinning of the SPI at about 100 - 300 km<sup>3</sup> over a 41 year period spanning 1944 to 1985. An additional 40 - 80 km<sup>3</sup> of ablation was explained by retreat of the glacial fronts. Observations of the rate of thickness change vary from extreme thinning at -11.1 m yr<sup>-1</sup> to a thickening rate on the Moreno glacier of 2.7 m yr<sup>-1</sup>. To obtain an estimate of the change over a Neoglacial advancement phase, we approximate the 48 SPI outlet glaciers as equivolume masses having a cross sectional area given by the equilibrium profile for a 2D glacier obeying Glen's flow law [e.g. Hutter 1983, page 284]. Truncating these idealized volumes with square edges, so that the longitudinal dimension is  $\bar{W}$ , then the volume of a single outlet glacier of flow law power index  $n = 3$  is

$$V = \frac{2}{3} \gamma^* \cdot \bar{D} \cdot \bar{W} \cdot \bar{L} \quad , \quad (38)$$

where  $\gamma^* \equiv \Gamma(3/8) \Gamma(7/4) / \Gamma(9/8) \approx 0.6006$ . Here  $\bar{L}$  is the half-width along the cross section,  $\bar{D}$  is the maximum depth (along the central axis) and  $\Gamma$  is the Euler gamma function. Typical dated moraine depositions show LIA and earlier Holocene advancements are about 1-2 km, or larger. A total volume estimate using  $N_{SPI} = 48$  plus  $N_{NPI} = 28$  for this glacier prototype yields 15,450 km<sup>3</sup>, for  $\bar{D} = 440$  m,  $\bar{L} = 10$  km and  $\bar{W} = 30$  km. Such a value is in rough accord with the inventories tabulated by Aniya *et al.* [1996]. A more precise estimate is unnecessary, as it is the differential Neoglacial ice volume that determines the load change. Taking the total differential of (38);

$$dV \approx 1.54 (N_{SPI} + N_{NPI}) (d\bar{D} \cdot \bar{L} \cdot \bar{W} + d\bar{W} \cdot \bar{L} \cdot \bar{D} + d\bar{L} \cdot \bar{W} \cdot \bar{D}) \quad (39)$$

and estimating the differential values to be 0.17, 1.9, 4.0 km for  $d\bar{D}$ ,  $d\bar{L}$ , and  $d\bar{W}$ , respectively, roughly consistent with the advances mapped by Mercer [1970; 1976; 1982], Rabassa & Clapperton [1990] and Aniya [1995], gives  $dV = 10,964$  km<sup>3</sup>. If these were positive (accumulation) changes it would correspond to a 3.4-fold increase in ice volume and a 0.36 meter lowering of eustatic sea level.

In order to expedite the parameter study it shall be assumed that the Neoglacial differential volume for the entire Patagonian ice fields, including those of the Cordillera Darwin, south of the Magellan Strait, is  $\Delta V = 1.0 \times 10^4$  km<sup>3</sup>. Similarly, for the rate sustained from 1944 to 1985 the same type of distribution is

assumed. Consequently, an identical disk thinning rate,  $\dot{h}_{0ji}$ , is assumed for each member of the pattern of disks shown in Figure 5 during each  $j$ th time interval. In terms of the  $i$ th disk load (Figure 3), it is assumed that all advance and recession is approximated by a linear rate  $\dot{h}_{0ji}$  with each radii  $\alpha_i$  held constant (Figure 4) for the entire duration of loading and unloading. The uniform rate of height change for the maximum and minimum estimates for SPI during 1944-1985 by *Aniya et al.* [1997], distributed over all disks shown in Figure 5, are  $\dot{h}_{0ji} = 0.13$  and  $0.36$  m/yr, respectively. Such values are consistent with direct observations. The estimates of volume change rates and magnitudes for the Holocene fluctuation model assumed (Figure 2) are consistent with the numerical studies of *Hulton et al.* [1994] and *Naruse et al.* [1995]. The former study shows that a 25 - 50 meter decrease in the equilibrium line altitude (ELA) has the potential to cause order  $0.1 - 1 \times 10^4 \text{ km}^3$  increase in total icefield volume over time scales of several centuries. It is plausible that such lowering of the ELA could be achieved by an atmospheric temperature decrease of about  $0.5^\circ \text{C}$  [*Hulton et al.* 1994].

## 6.2 Possible Patagonian Lithosphere-Mantle Structure.

In section 4 we have briefly discussed the possible mechanical strength properties that might be applicable to the southernmost Cordillera of Chile and Argentina. The main point is that Patagonia and environs are quite unlike Fennoscandia and eastern Canada, and all tectonic indicators suggest a weaker lithosphere-mantle mechanical structure. Lithosphere and mantle properties that have been derived from Fennoscandian rebound, therefore, provide a probable upper bound for both an estimate of lithospheric thickness and effective mantle viscosity. *Mitrovica* [1996] has recently reanalyzed Fennoscandian rebound constraints on lithospheric thickness and upper mantle viscosity and determined a range of values:

$$75 \leq h \leq 125 \text{ km} ,$$

$$0.65 \times 10^{21} \leq \eta \leq 1.1 \times 10^{21} \text{ Pa s} .$$

We shall refer to values in this range as "Fennoscandian" structure. Another recent analysis of relative sea level history along the coastline of the United Kingdom by *Lambeck* [1993] has determined a bound;

$$60 \leq h \leq 75 \text{ km} ,$$

$$3 \times 10^{20} \leq \eta \leq 5 \times 10^{20} \text{ Pa s} .$$

A lower viscosity seems to fit paleoshoreline data from Australia [*Nakada & Lambeck* 1989] and bounds for this region are approximately;

$$50 \leq h \leq 100 \text{ km} ,$$

$$1 \times 10^{20} \leq \eta \leq 2 \times 10^{20} \text{ Pa s} .$$

For reasons summarized in sections 4.1 and 4.2, and, in particular, the geologically recent creation of a "slab free window" [*Gorring et al.* 1997], each of these ranges probably overestimate the regional upper mantle viscosity south of the Chile Triple Junction to varying degrees. Love and Rayleigh wave

tomography reveal the upper 100 km beneath Patagonia to be similar to continental regions that presently experience tectonic extension and island arc volcanism [Montagner & Tanimoto 1991]. Recent models of plume motion and the relative fixity of hotspots indicate that the average upper mantle viscosity beneath the lithosphere of the Pacific is  $1.5 \times 10^{20}$  Pa s, or less [Steinberger & O'Connell 1998]. Although the spectrum of possible lithospheric thicknesses and/or upper mantle viscosities could be more extreme, we limit our study of mechanically weaker solid Earth structure to

$$25 \leq h \leq 75 \text{ km} ,$$

$$5 \times 10^{18} \leq \eta \leq 1.0 \times 10^{20} \text{ Pa s} .$$

This realm is, essentially "Basin and Range" in type.

The goal of the parameter study that follows is to find out how the predictions of present-day vertical isostatic rebound are influenced by the following unknowns; (1) variability in the Holocene icefield history (Figure 2), (2) the rate of mass wastage of the icefields over the observation period of 1944-1985, including post-1985 changes in that rate, and finally, (3) the trade-off of vertical rate predictions with the mechanical strength of the lithosphere-mantle system.

### 6.3 Parameter Study.

#### 6.3.1 Icefield Change Between 1944-1985 and to the Present-Day: Elastic Rebound.

Figure 5 shows a contour map of the predicted present-day uplift rate given the volume change in the icefields over the 41-year observation period of *Aniya et al.* [1997], but distributed equally among the 36 disks shown and extended to the present-day (AD 2000). The lithosphere-mantle structure assumed for the model in Figure 5 is completely elastic and has parameters given in Table 3 with  $h = 65$  km. Here the elastic-gravitational rebound rate is directly proportional to  $\dot{V}_A$ , the volume rate from *Aniya et al.* [1997].

#### 6.3.2 Viscoelastic "Fennoscandian" Structure and Types 1 and 2 Load Histories.

Figures 6a and 6b show the predicted present-day solid surface vertical displacement rate for Holocene histories of Types 1 and 2 (Figure 2). Here the lithosphere is assumed to be 65 km thick with the same rigidities and densities as in Figure 5, except that the half-space (upper mantle) is Maxwell viscoelastic with a viscosity of  $\eta = 6.5 \times 10^{20}$  Pa s. Note from a comparison of Figure 5 with Figure 6a and b that larger rates are driven by the inclusion of a viscoelastic mantle and a Neoglacial history, and, more importantly, that the sign of the prediction reverses. This emphasizes the important aspect that viscoelasticity brings to interpreting present-day crustal uplift connected to observations of Holocene glacial variability and LIA growth and collapse. Viscoelasticity acts as a low-pass filter in time, so that it is the time-integrated ice mass changes and their effect on isostasy that dominantly drive present-day uplift.

A comparison of the cases shown in Figures 5 and 6 reveals that the details of the late Holocene history are likely to be more important than the purely elastic rebound. The latter is sustained only by present-day ice mass imbalances. This is demonstrated even though only a moderately weak Earth structure model of "Fennoscandian" type [Mitrovica 1996] has been assumed. Using the two types of glacial history (Figure 2), we now explore the predictions associated with both ("Australian") and the much weaker ("Basin and Range") lithosphere-mantle structure.

### 6.3.3 "Australian" Lithosphere-Mantle Structure.

Assuming the same lithospheric thickness and glacial input parameters as assumed for computations shown in Figure 6b, Figure 7 shows the predicted response with a viscosity that is consistent with an analysis of rebound along the coast of Australia [Nakada & Lambeck 1989]. Assuming this lower viscosity, the predictions are large enough that the model input parameters might be testable using long-term GPS geodetic monitoring. It is useful to reference one site that is near the zone of maximum displacement rate (but outside of the icefield) and another that is more than several load width-wavelengths (comparable to the largest disk diameters in the load model) removed. The western reference site shown in Figure 7 (the Chilean town of Villa O'Higgins) is near S 48.5°, E 286.75° (or W 73.25°). The eastern site is near S 48.5°, E 289.0° (the Argentine town of Tamal Aike). Villa O'Higgins (Figure 7) sustains a deformation that is consistent with the inner depression for all assumed Earth structure models. For thinner lithospheres than about 50 km, Tamal Aike deforms as an outer peripheral bulge zone.

The subsidence at present-day that is predicted in Figure 7 is quite unlike what we expect 120 years of deglaciation to produce. What features of the model cause this?

In order to understand the physical mechanisms that drive the present-day response it will be necessary to decompose the load history. In Figure 8 partitioned vertical rate predictions are shown in which the pre-1400 Holocene (plus late-Pleistocene LGM) are separated from post-1400 (LIA, or Neoglacial IV in Figure 2) effects. The separation demonstrates that the pre-1400 glacial load contributions lead to a rather classic style isostasy: a load is emplaced at some time in the past and, after its removal, the depressed landscape uplifts. This type of response is shown at the left of each of the histograms of frames (a) through (c) in Figure 8. Note that the Type 2 load predicts stronger pre-1400 induced present-day uplift rates than does Type 1, due to the presence of a more recent glacial oscillation (compare the two timings of Neoglacial III in Figure 2). Also note that Type 2 produces a more robust subsidence component in the post-1400 portion of the responses. Figure 8a assumes a lithospheric thickness and an upper mantle viscosity consistent with the global study of Tushingham & Peltier [1991]. Frames (b) and (c) of Figure 8 reveal the decreased role of pre-1400 (pre-LIA) load as viscosity is decreased from  $10^{21}$  Pa s. Here frames (b) and (c) correspond to the computational results shown in Figures 6 and 7.

#### 6.3.4 "Basin & Range" Lithosphere-Mantle Structure.

As can be deduced from Figure 8c, a viscosity at, or below,  $10^{20}$  Pa s responds primarily to the last mass oscillation of the icefields. Analysis in the lower viscosity range requires a decomposition of the LIA load. A refined partitioning of the post-1400 load is shown in Figures 9a and 9b for Types 1 and 2, respectively. The partitions produce predictions of uplift due to the portion at the left (growth phases) and subsidence due to the portion at the right (incomplete collapse phases).

Figure 10 shows the LIA vertical rates predicted assuming the partitions shown in Figure 9. The white line in the bar graph for Type 2 in the left of each frame indicates the response to the growth phase if it were terminated at the year AD 1850. This assumption for Type 2 allows for an unambiguous comparison to Type 1 growth in which the latter has a fixed load from AD 1700 to 1850 (see Figures 2 and 9). Note that an extension of the Type 2 growth phase by 30 years, indeed, has a 20-25% level contribution to the total 1400-1880 response partition (compare white line to the full bar graph). In each case a reduction by 30 years in the growth phase of Type 2 results in a weaker positive uplift. The mapviews that correspond to these cases are shown in Figure 11.

A physical interpretation emerges from Figure 10. Here the longer, or more robust, loading produces larger deviation from gravitational isostatic equilibrium. That larger disequilibrium, in turn, produces larger, and more recently initiated, isostatic uplift. However, in the shorter growth phase cases for Type 2 (white line), it is the Type 1 response, which is of smaller (negative) amplitude, that is added to form the total contribution. Type 2 loading, having no prolonged period of maximum glacial advancement, is less efficient than Type 1 loading (having achieved a maximum 150 years earlier than Type 2) in producing positive uplift at present-day. This conclusion is supported by each of frames (a) through (c) of Figure 10.

Note that the partition in Figure 10a shows a near-cancellation of the growth and collapse contributions. However, for the same Earth structure and viscosity the prediction at the 'outer bulge' position (Figure 10b) shows stronger sensitivity to the early part of the LIA. This is probably due to the fact that longer wavelength components of the deformation field have a longer-term memory of the assumed 450 and 480 year growth phase than does the shorter wavelength field. Frame (c) shows a lower viscosity case that can be compared to frame (a). Note that in this lower viscosity case (Figure 10c), the total rebound from the AD 1400 to mid-19th Century depression is stronger than in the higher viscosity case (Figure 10a). This greater efficiency is also allowed to act during the (incomplete) collapse phase. For example, the subsidence response to the collapse phase after 1850 in Type 1 is reduced by about 20% over the higher viscosity regime (compare right frames of Figures 10a and 10c), while the efficiency of the rebound rate component from pre-1850 is increased by 20% (compare left frames of Figure 10 a and c), and this produces a total positive rebound rate prediction for the present-day for the lower viscosity ( $\eta = 1.0 \times 10^{19}$  Pa s). This greater efficiency enhances the sensitivity to the volume reduction (unloading) during retreat from 1850 to the present-day. The effect is also seen in the Type 2 case.

### 6.3.5 Complex Patterns of Uplift and Subsidence in the Weak Mechanical Regime.

Figure 11 shows the total predicted vertical velocity for Type 1 (a and b) and Type 2 (c and d) for cases corresponding to the histograms of Figure 10. The inner depression region, with predicted subsidence rates of -1.0 to 0 mm/yr in Figure 11a, are controlled almost entirely by the two LIA components (growth and collapse) as discussed in reference to Figure 10. Note the broad zone of outer bulge uplift that is predicted at the level of 2-3 mm/yr in Figure 11a. With a factor of two reduction in viscosity (Figure 10b), however, the inner depression zone uplifts at present-day due to the enhanced efficiency of the rebound process (see the discussion in reference to Figure 10). Here the rebound from the isostatic depression created during the first several hundred years of the LIA dominates over the (ablating) load imposition since the mid-Nineteenth Century that continues into the present-day.

Clearly, the higher viscosity cases ( $\eta > 2.0 \times 10^{19}$  Pa s) are relatively insensitive to ice mass changes over the past century and a half, but are quite sensitive to the fact that an LIA has effectively produced a *net ice load* during the last 600 years. Hence, the higher viscosity cases predict subsidence to be ongoing at present-day. The first explanation of this subtle physics involved in viscoelastic isostasy and the LIA was offered by *Wolf, Barthelmes & Sigmundsson* [1997] in modeling the 20th Century collapse of a major glacial system in Iceland. Here we have given some further explanation of this interesting sensitivity of geodetic observation to both the LIA and mantle viscosity in Patagonia.

Both the 150 year evolutionary hiatus at LIA maximum advancement and the earlier initiation of recession produces uplift in the case shown in Figure 11b (Type 1 load) in comparison to the near cancellation that is shown in Figure 11d (Type 2 load) near the inner depression zone. Figure 12 shows the vertical velocity predicted for  $h = 25$  km. The viscosity is the same as in cases (b) and (d) of Figure 11. Cases (a) and (b) assume load Type 1 and 2, respectively. Type 1 (Figure 12a) clearly shows the prediction of uplift as opposed to subsidence (Figure 12b) predicted by Type 2. An explanation of the differences between these two predicted responses parallels that for Figure 12 for  $h = 35$  km at the same viscosity values. Comparison of 12a and 12b reveals striking contrasts. Both a more efficient isostatic flow during loading for Type 1 history and the effect of a 30 year lead in glacial recession, dominate these differences. When combined, the two load history effects, at this lithospheric thickness value ( $h = 25$  km), produce dramatically different predictions of uplift pattern. The differences in prediction within the zone of central depression reach 14 mm/yr.

### 6.3.6 Sensitivity to Little Age Ice (LIA) Timing in the Weak Mechanical Regime.

The diagram of simple LIA growth and collapse that is shown in Figure 2b (Neoglacial IV) assumes that a 380-year growth phase is initiated in AD 1400 and that a maximum is achieved during the late 19th Century. These assumptions are consistent with regional observations [*Warren & Sugden* 1993; *Warren* 1993; *Villalba* 1994; *Aniya* 1995]. It is of interest to investigate the influence of a shorter growth phase. Such a case is computed with the same initiation date, but with equivalent epochs (300 yr) for

accumulation and ablation. In this case the maximum is achieved in AD 1700 and the result is shown in Figure 12c. Indeed, the difference in the resulting prediction for Type 2 is dramatic (compare predictions with either Figure 12a or 12b which assume the same mantle viscosity and lithospheric thickness). Apparently, while the loading is of sufficient duration (300 yr) to place the mechanical system far from equilibrium at the year AD 1700, the total 300-year ice mass wasting (unloading) is sufficient to cause rebound (uplift) at all wavelengths at the present-day. Our preferred model, however, has a longer growth phase, as portrayed in Figures 2a and 2b. Finally, in Figure 13 we show predictions for Types 1 and 2 Neoglaciations for the lowest mantle viscosity value considered here ( $\eta = 5 \times 10^{18}$  Pa s). Here all memory of the LIA growth phase is dwarfed by the robust isostatic response to 20th Century deglaciation.

What we have learned from these numerical experiments with realistic, yet simple, Patagonian LIA loading histories is that the lower end of the viscosity spectrum contains a rich assortment of response patterns and styles. These may involve either subsidence or uplift at present-day.

#### 6.4 Summary of Results.

Viscoelastic memory dominates the predicted deformation over all realistic ranges of viscosity. This conclusion is in some conflict with the model results of *Trupin et al.* [1996] who computed uplift rates in the Pacific northwest caused by the combined influence of LGM, an AD 1650-1900 LIA and 20th Century regional glacial recession. The main difference, however, can be attributed to the different total volume rates of recession assumed by the models during the 20th Century. The latter model assumes a mass wasting of the combined Pacific Northwest glacial system (including Alaska) that, alone, accounts for the entire 0.4 mm/yr 20th Century rise in sea level that *Meier* [1984] found plausible for the total world-wide system of small mountain glaciers and ice caps. In marked contrast, the estimate of *Aniya et al.* [1997] for South America's southernmost Cordillera, that is assumed here, accounts for approximately 1/20 th of the total small mountain glacier contribution ( $\approx 0.4$  mm/yr) to sea level rise. The estimate of *Aniya et al.* [1997] is consistent with values that *Meier* [1984] derived for southern Patagonia from scaling well-measured alpine glacial systems.

##### 6.4.1 Weak Mechanical Regime.

There is considerable sensitivity of the predicted uplift to the details of the LIA load history occur for cases where the viscosity is in the range;  $5.0 \times 10^{18} \leq \eta < 5.0 \times 10^{19}$  Pa s, and the lithosphere is relatively thin;  $h < 50$  km. This regime may be akin to that proposed for extensional continental tectonic environs such as the Basin and Range province of western North America [*Bills, Currey & Marshall* 1994]. In this mechanical regime present-day peripheral uplift (subsidence?) rates may be dramatic and peripheral bulge deformation might be unusually pronounced. Such exotic deformation style is perhaps explained as a phase-lagged viscoelastic wave, in which the forcing frequency (period of Holocene glacial fluctuations) is comparable to the inherent relaxation decay times of the Earth structure model. Geodetic

observation of vertical displacement within the inner depression zone (near the load) will be highly sensitive to both the details of Earth structure and timing of the LIA growth and collapse. The predicted results have shown that both uplift or subsidence may be predicted, or a near cancellation of effects might occur. There is some analogy to a stationary wave that is either phase-lagged (subsidence at present-day), in-phase (uplift at present-day), or in a state of transition (giving near zero rate) in which out-of-phase behavior (subsidence) is waning and will, in the future, be replaced by in-phase (uplift) as glacial collapse continues. This finding is consistent with modeling results recently reported by *Wolf et al.* [1997] who also included the effect of a finite-depth low viscosity asthenospheric layer just below the lithosphere.

#### 6.4.2 Strong Mechanical Regime.

For a mantle viscosity that is comparable to that of Fennoscandia any sensitivity to the details of late Holocene Neoglaciation is insignificant (see Figure 6a and 6b). In fact, in this viscosity range ( $\eta \geq 6.5 \times 10^{20}$  Pa s) the present-day vertical motions are likely to be small unless the glacial mass involved in the Neoglaciation or that in present-day deterioration of the SPI and NPI complexes has been grossly underestimated. For either models of Type 1 or Type 2, the maximum rates are of order 1 mm/yr of subsidence. The subsidence reflects the time-integrated load that is 'felt' by the viscoelastic mantle. Elastic rebound, which occurs as an instantaneous response to glacial mass changes, is predicted to be of smaller magnitude (about one third at  $\eta = 6.5 \times 10^{20}$  Pa s) and to have a contribution (uplift) that opposes that of viscoelasticity in both the stronger ('Fennoscandian') and intermediate ('Australian') mechanical regimes. Crustal motion induced by Neoglaciations in the stronger mechanical regime are probably undetectable using space geodesy. The story, however, is quite different if the mantle viscosity is reduced by a factor of 10, or more, below that of stable cratonic (Fennoscandian or eastern Canadian) mantle.

Although many of the environmental and solid Earth parameters are poorly known, our numerical study suggests that the Holocene Neoglaciation of southern Patagonia causes present-day crustal motions that are at a detectable level ( $\geq 4$  mm/yr), given current estimates of formal errors in the vertical associated with continuous Global Positioning System (GPS) satellite tracking data [*Zumberge et al.* 1997].

#### 7. Conclusions.

Glacial moraines of the vast icefields of the southernmost Andean Cordillera record several periods of advancement and retreat during mid and late Holocene time. These regional glacial changes may be related to variations in precipitation and/or atmospheric temperature [*Hulton et al.* 1994; *Naruse et al.* 1995]. Four  $^{14}\text{C}$  dated Neoglacial advances and retreats of the Patagonian icefields during the last 5 millennia [*Rabassa & Clapperton* 1990; *Aniya* 1995] are modeled as ice loads that force viscoelastic gravitational deformation of the solid Earth. Our numerical models illustrate that significant vertical motion (2 - 20 mm/yr) might be occurring at present-day if the rates of glacial mass wasting determined by *Aniya et al.* [1997] represent a continuous recession of the Patagonian icefields from a Little Ice Age maximum and



if the local mantle viscosity is similar to that estimated for regions sustaining Neogene tectonism. We speculate that this lower viscosity regime is very likely to exist in southern Patagonia due to the subduction of oceanic ridge segments at 6 - 14 Ma and subsequent eruption of relatively large volumes of theolitic lavas and the creation of an upper mantle slab window [Gorring *et al.* 1997]. Nearly all of the Argentine towns shown in Figure 6b are located within the Magellan Basin, a region of recent tectonic extension [Diraison *et al.* 1997]. The icefields are located within the Austral Volcanic Zone (AVZ), a region with numerous Holocene-age eruptive magmas. Geochemical analyses of these magmas indicate melting of both sediment and basalt within the subducting Antarctic plate and melting of both mantle wedge and crustal rocks located above the slab [Stern & Kilian 1996]. Peacock, Rushmer & Thompson [1994] argue that AVZ Pleistocene/Holocene magmagenesis involves the release of structurally bound  $H_2O$  at depth. Such active slab dehydration implies a relatively low mantle viscosity due to the sensitivity of  $\alpha$ -phase olivine rheology to trace content of water [Hirth & Kohlstedt 1996; Chen *et al.* 1998].

Details of a Little Ice Age glacial advancement and subsequent recession, such as the duration at maximum and timing of glacial recession, complicate the classic picture of glacial isostatic adjustment in the low viscosity range ( $5 \times 10^{18} \leq \eta \leq 10^{20}$  Pa s). The vertical response of a phase-lagged viscoelastic Earth to Little Ice Age deglaciation can be either positive (emergent) or negative (submergent) at the present-day. The latter predictions are in substantial agreement with recent Little Ice Age modeling of the Vatnajökull ice cap in Iceland by Wolf *et al.* [1997]. In sum, the mapview crustal motion predictions given in this paper illustrate that the trade-off of glacial load history during the last half-millennium with Patagonian mantle viscosity is far more intricate than initially anticipated.

## Appendix A: Comparison of Spherical and Planar Vertical Deformation Solutions

In this Appendix we briefly describe two important features of the theoretical model discussed and developed in section 5. First, the model can be directly compared to the results of Wolf [1984; 1985a; 1985b]. Figure A-1 shows the decay spectra,  $\gamma_p$ , in inverse years. A characteristic 'hummingbird' shape in wavenumber-eigenvalue space is revealed. This character underlies the response of a simple elastic lithosphere welded to a viscoelastic half-space. Figure A-2 shows the surface vertical response for a single disk load having Heaviside unit step function character in time. Cases shown in Figure A-2 are directly comparable to computational examples discussed by Wolf [1984; 1985a]. Comparison to the later examples reveals that they are essentially identical and that, therefore, each may be regarded as providing numerical benchmarks.

Secondly, we provide a comparison of predictions using both polar coordinate, planar geometry (this paper) and spherical geometry. The latter predictions are constructed using a radially layered incompressible Maxwell model developed by James [1991] after the method of Sabadini, Yuen & Boschi [1984]. This provides an assessment of the level of error that is engendered by adoption of flat-earth approximation for

the calculation of postglacial isostatic adjustment. Thus, we provide an extension of the work of *Wolf* [1984] and *Amelung & Wolf* [1994] who studied the differences in response of spherical and flat-earth models. The comparison here is performed for the case of ICE-3G deglaciation of the Patagonian region. The spherical theory employed assumes finite self-gravitational terms. The latter terms are relevant to such comparisons, as noted by *Amelung & Wolf* [1994]. Figure A-3a shows the difference between spherical and flat-earth calculations. The total surface displacement (in meters) is shown in Figure 3b at 2 kyr after the termination of deglaciation assuming the ICE-3G model of *Tushingham & Peltier* [1991] for which the equivalent time is 13 ka BP. The differences are generally of order 1%, with peak differences at a 10% level in the peripheral bulge zones (5 meter lobate-shaped uplift in the Pacific and Atlantic). Figure A-3c and A-3d show the ICE-3G isostatic uplift rates at present-day for spherical and flat-earth models, respectively. The spherical-earth model was also computed at degree 480 truncation for resolution testing. The spherical model is well-resolved at degree truncation 240. The contours are almost indistinguishable, except for slight differences in the regions of peripheral bulge generation which, here, show ongoing subsidence. The comparison demonstrates that flat-earth approximations are rather reliable over 20 degrees of Earth surface.

### Acknowledgements

This work was performed at the Jet Propulsion Laboratory, California Institute of Technology, under contract with NASA and at the Pacific Geoscience Centre, an office of the Geological Survey of Canada. The JPL Supercomputing Office has provided support of its facilities. A grant from the Solid Earth and Natural Hazards Program of NASA's Earth Science Office has provided support for this research. Correspondence and conversations with Detlef Wolf are most gratefully acknowledged. Carol A. Raymond and Kenneth Hurst are thanked for comments and suggestions related to this research. Geological Survey of Canada Contribution xxx.

### References

- Amelung, F. & Wolf, D. Viscoelastic perturbations of the earth: significance of the incremental gravitational force in models of glacial isostasy, *Geophys. J. Int.*, **117**, 864-879, (1994).
- Aniya, M. Glacier inventory for the Northern Patagonian Icefield, Chile, and variations 1944/45 to 1985/86, *Arctic and Alpine Res.*, **20**, 179-187, (1988).
- Aniya, M. Holocene glacial chronology in Patagonia: Tyndall and Upsala glaciers, *Arctic and Alpine Res.*, **27**, 311-322, (1995).
- Aniya, M., Sato, H., Naruse, R., Svarca, P. & Casassa, G. The use of satellite and airborne imagery to inventory outlet glaciers of the Southern Patagonian Icefield, South America, *Photogrammetric Eng. Remote Sensing*, **62**, 1361-1369, (1996).

- Aniya, M., Sato, H., Naruse, R., Svarca, P. & Casassa, G. Recent glacier variations in the Southern Patagonian Icefield, South America, *Arctic and Alpine Res.*, **29**, 1-12, (1997).
- Bills, B.G., Currey, D.R. & Marshall, G.A. Viscosity estimates for the crust and upper mantle from patterns of lacustrine shoreline deformation in the eastern Great Basin, *J. Geophys. Res.*, **99**, 22,059-22,086, (1994).
- Boninsegna, J.A. South American dendroclimatological records, in *Climate Since A.D. 1500*, (ed., Bradley, R.S. & Jones, P.D.) Routledge, New York, N.Y., 446-462, (1995).
- Broecker, W.S. Glacial rebound and the deformation of the shorelines of proglacial lakes, *J. Geophys. Res.*, **71**, 4777-4783, (1966).
- Dirac, P.A.M., *The Principles of Quantum Mechanics*, Oxford University Press, London, pp. 312, (1958).
- Candie, S.C. & Leslie, R.B. Late Cenozoic tectonics of the southern Chile Trench, *J. Geophys. Res.*, **91**, 471-496, (1986).
- Chen, J., Inoue, T., Weidner, D.J., Wu, Y. & Vaughan, M.T. Strength and water weakening of mantle minerals, olivine, wadsleyite and ringwoodite, *Geophys. Res. Lett.*, **25**, 575-578, (1998).
- Clapperton, C.M. & Sugden, D.E. On Late-glacial and Holocene glacier fluctuations in maritime West Antarctica, in *Late- and Postglacial Oscillations of Glaciers: Glacial and Periglacial Forms*, (ed., Schroeder-Lanz, H.) A.A. Balkema, Rotterdam, 283-290, (1983).
- Clapperton, C.M. & Sugden, D.E. Holocene glacier fluctuations in South America and Antarctica, *Quat. Sci. Rev.*, **7**, 185-198, (1988).
- Clapperton, C.M., Sugden, D.E., Kaufman, D.S. & McCulloch, R.D. The Last Glaciation in Central Magellan Strait, southernmost Chile, *Quat. Res.*, **44**, 133-148, (1995).
- Clark, J.A. A numerical model of worldwide sea level changes on a viscoelastic Earth, in *Earth Rheology, Isostasy and Eustasy*, (ed. N.A. Mörner) Wiley Interscience, N.Y., 525-534, (1980).
- Diraison, M., Cobbold, P.R., Gapais, D. & Rossello, E.A. Magellan Strait: part of a Neogene rift system, *Geology*, **25**, 703-706, (1997).
- Farrell, W.E., Deformation of the Earth by surface loads, *Rev. Geophys.*, **10**, 761-797, (1972).
- Giunchi, C., Spada, G. & Sabadini, R. Lateral viscosity variations and postglacial rebound: Effects on present-day VLBI baselines, *Geophys. Res. Lett.*, **24**, 13-16, (1997).
- Gorring, M.L., Kay, S.M., Zeitler, P.K., Ramos, V.A., Rubiolo, D., Fernandez, M.I. & Panza, J.L. Neogene Patagonian plateau lavas: continental magmas associated with ridge collision at the Chile Triple Junction, *Tectonics*, **16**, 1-17, (1997).
- Goes, S., Govers, R., Schwartz, S. & Furlong, K.P., 3-D modeling for the Mendocino Triple Junction area, *Earth Planet. Sci. Lett.*, **148**, 45-57, (1997).

- Hamza, V.M. & Muñoz, M. Heat flow map of South America, *Geothermics*, **25**, 599-616, (1996).
- Hansen, J. & Lebedeff, S. Global trends of measured surface air temperature, *J. Geophys. Res.*, **92**, 13,345-13,372, (1987).
- Heusser, C.J. Southern Westerlies during the last glacial maximum, *Quaternary Res.*, **31**, 423-425, (1989).
- Heusser, C.J. & Streeter, S. A temperature and precipitation record of the past 16,000 years in southern Chile, *Science*, **210**, 1345-1347, (1980).
- Heusser, C.J., Denton, G.H., Hauser, A., Andersen, B.G. & Lowell, T.V. Water fern (*Azolla filiculoides* Lam.) in southern Chile as an index of paleoenvironment during early deglaciation, *Arctic and Alpine Res.*, **28**, 148-155, (1996).
- Hirth, G. & Kohlstedt, D.L., Water in the oceanic upper mantle: implications for rheology, melt extraction and the evolution of the lithosphere, *Earth Planet. Sci. Lett.*, **144**, 93-108, (1996).
- Hsui, A., Some remarks on the thermal consequences of ridge subduction, *Geophys. Res. Lett.*, **8**, 1031-1034, (1981).
- Hulton, N., Sugden, D., Payne, A. & Clapperton, C. Glacier modeling and the climate of Patagonia during the last glacial maximum *Quaternary Res.*, **42**, 1-19, (1994).
- Hutter, K., *Theoretical Glaciology*, D. Reidel, Dordrecht, Holland, pp. 510, (1983).
- Huybrechts, P. The Antarctic ice sheet and environmental change: A three-dimensional modeling study, *Ber. Polarforsch.*, **99**, 1-241, (1992).
- Ivins, E.R., Transient creep of a composite lower crust: 2. A polymineralic basis for rapidly evolving postseismic deformation modes, *J. Geophys. Res.*, **101**, 28,005-28,028, (1996).
- Ivins, E.R. & C.G. Sammis, On lateral viscosity contrast in the mantle and the rheology of low-frequency geodynamics, *Geophys. J. Int.*, **123**, 305-322, (1995).
- Jaeger, J.C., *Elasticity, Fracture and Flow with Engineering and Geological Applications*, Chapman & Hall, London, pp. 268, (1969).
- James, T.S., Post-glacial deformation, Ph.D. Dissertation, Princeton University, (1991).
- Jones, P.D., Raper, S.C.B. & Wigley, T.M.L. Southern Hemisphere surface air temperature variations: 1851-1984, *J. Climate Appl. Meteorology*, **25**, 1213-1230, (1986).
- Kaufmann, G. & Wolf, D., Deglacial land emergence and lateral upper-mantle heterogeneity in the Svalbard Archipelago: 2. Extended results for high-resolution load models, *Geophys. J. Int.* **127**, 125-140, (1996).
- Lambeck, K., Glacial rebound of the British Isles - II. A high-resolution, high-precision model, *Geophys. J. Int.*, **115**, 960-990, (1993).

- McConnell, R.K., Isostatic adjustment in a layered Earth, *J. Geophys. Res.*, **70**, 5171-5188, (1965).
- Maeda, Y., Nakada, M., Matsumoto, E., & Matsuda, I. Crustal tilting from Holocene sea-level observations along the east coast of Hokkaido in Japan and upper mantle rheology. *Geophys. Res. Lett.* **16**, 857-860, (1992).
- Matsu'ura, M. & Iwasaki, T. Study on coseismic and postseismic movements associated with the 1923 Kanto earthquake. *Tectonophysics* **97**, 201-215, (1983).
- Meier, M.F., Contribution of small mountain glaciers to global sea-level, *Science*, **226**, 1419-1421, (1984).
- Mercer, J.H., Variations of some Patagonian glaciers since the Late-Glacial: II, *Amer. J. Sci.*, **269**, 1-25, (1970).
- Mercer, J.H., Glacial history of southernmost South America, *Quaternary Res.*, **6**, 125-166, (1976).
- Mercer, J.H., Holocene glacier variations in southern South America, *Striae*, **18**, 35-40, (1982).
- Mitrovica, J.X., Haskell [1935] revisited, *J. Geophys. Res.*, **101**, 555-569, (1996).
- Mitrovica, J.X. & Peltier, W.R., A complete formalism for the inversion of postglacial rebound data: resolving power analysis, *Geophys. J. Int.*, **104**, 267-288, (1991).
- Montagner, J-P. & Tanimoto, T., Global upper mantle tomography of seismic velocities and anisotropies, *J. Geophys. Res.*, **96**, 20,337-20,351, (1991).
- Nakada, M. & Lambeck, K. Late Pleistocene and Holocene sea-level change in the Australian region and mantle rheology. *Geophys. J.* **96**, 497-517, (1989).
- Nakada, M. & Lambeck, K. Late Pleistocene and Holocene sea-level change; evidence for lateral mantle viscosity structure? in *Glacial Isostasy, Sea-level and Mantle Rheology*, pp. 79-94, eds Sabadini, R., Lambeck, K. & Boschi, E., Kluwer, Dordrecht, (1991). (1989).
- Naruse, R. & Aniya, M. *Glaciological Researches in Patagonia*, 1990 Japanese Society of Snow and Ice, 130 pp. (1992).
- Naruse, R., Aniya, M., Skvarca, P. & Casassa, G. Recent variations of calving glaciers in Patagonia, South America, revealed by ground surveys, satellite-data analyses and numerical experiments. *Anal. Glaciology* **21**, 297-303, (1995).
- Oerlemans, J., Climate sensitivity of Franz Joseph Glacier, New Zealand, as revealed by numerical modeling, *Arctic Alpine Res.*, **29**, 233-239, (1997).
- Peacock, S.M., Rushmer, T., & Thompson, A.B. Partial melting of subducting oceanic crust, *Earth Planet. Sci. Lett.*, **121**, 227-244, (1994).
- Peltier, W.R., The impulsive response of a Maxwell Earth, *Rev. Geophys. Space Phys.*, **12**, 649-668, (1974).

- Peltier, W.R., Glacial-isostatic adjustment - II. The inverse problem, *Geophys. J. R. Astr. Soc.*, **46**, 669-705, (1976).
- Peltier, W.R., Ice age paleotopography, *Science*, **265**, 195-201, (1994).
- Porter, S., Pleistocene glaciation in the southern Lake District of Chile, *Quatern. Res.*, **16**, 263-292 (1981).
- Rabassa, J. & Clapperton, C.M. Quaternary glaciations of the southern Andes. *Quatern. Sci. Rev.*, **9**, 153-174, (1990).
- Sabadini, R.C.A., Yuen, D.A. & Boschi, E. A comparison of the complete and truncated versions of the polar wander equations, *J. Geophys. Res.*, **89**, 7609-7620 (1984).
- Sigmundsson, F. Postglacial rebound and asthenospheric viscosity in Iceland, *Geophys. Res. Lett.*, **18**, 1131-1134, (1991).
- Sneddon, I.H. *The Use of Integral Transforms*, McGraw-Hill, N.Y., pp. 539, (1972).
- Steinberger, B. & O'Connell, R.J. Advection of plumes in mantle flow: implications for hotspot motion, mantle viscosity and plume distribution, *Geophys. J. Int.*, **132**, 412-434, (1998).
- Stern, C.R. & Kilian, R. Role of the subducted slab, mantle wedge and continental crust in the generation of adakites from the Andean Austral Volcanic Zone, *Contrib. Mineral Petrol.*, **134**, 263-281, (1996).
- Thompson, L.J., Mosley-Thompson, E., Dansgaard, W. & Grootes, P.M. The Little Ice Age as recorded in tropical Quelcaya ice cap, *Science*, **234**, 361-364, (1986).
- Thorkelson, D.J. Subduction of diverging plates and the principles of slab window formation, *Tectonophysics*, **225**, 47-63, (1996).
- Trupin, A.S., Easson, D.A. & D. Han. Vertical motion and ice thickness variation in western North America. *Geophysical Res. Lett.* **23**, 253-256, (1996).
- Tushingham, A.M. & Peltier, W.R. ICE-3G: A new global model of late Pleistocene deglaciation based upon geophysical predictions of postglacial relative sea-level, *J. Geophys. Res.*, **96**, 4497-4523, (1991).
- Villalba, R. Climate fluctuations in Northern Patagonia during the last 1000 years as inferred from tree ring records, *Quatern. Res.*, **34**, 346-360 (1990).
- Villalba, R. Tree-ring and glacial evidence from the Medieval Warm Epoch and the Little Ice Age in southern South America, *Climate Change*, **26**, 183-197 (1994).
- Vermeersen, L.L.A. & N.J. Vlaar, The gravito-elastodynamics of a pre-stressed Earth, *Geophys. J. Int.*, **104**, 555-563, (1991).
- Walcott, R.I. Isostatic response to loading of the crust in Canada. *Canadian J. Earth Sci.*, **7**, 716-729, (1970).

- Ward, S.N., A note on lithospheric bending calculations, *Geophys. J. R. Astr. Soc.*, **78**, 241-253, (1984).
- Warren, C.R. Rapid recent fluctuations of the calving San-Rafael glacier, Chilean Patagonia: climatic or non-climatic? *Geografiska Annal.*, **75 A**, 111-125, (1993).
- Warren, C.R. & Sugden, D.E. The Patagonian icefields: A glaciological review, *Arctic and Alpine Res.*, **25**, 316-331, (1993).
- Wolf, D., The relaxation of spherical and flat Maxwell Earth models and effects due to the presence of the lithosphere, *J. Geophysics*, **56**, 24-33, (1984).
- Wolf, D., The normal modes of a layered, incompressible Maxwell half-space, *J. Geophysics*, **57**, 106-117, (1985a).
- Wolf, D., The normal modes of a uniform, compressible Maxwell half-space, *J. Geophysics*, **56**, 100-105, (1985b).
- Wolf, D., The changing role of the lithosphere in models of glacial isostasy: a historical review, *Global and Planetary Change*, **8**, 95-106, (1993).
- Wolf, D., F. Barthelmes & F. Sigmundsson, Predictions of deformation and gravity caused by recent change of Vatnajökull ice cap, Iceland, *Comp. Rend. J. Luxemb. Geodyn.*, **82**, 36-42, (1997).
- Zumberge, J.F., Heflin, M.B., Jeffereson, D.C., Watkins, M.M. & F.H. Webb, Precise point positioning for efficient and robust analysis of GPS data from large networks, *J. Geophys. Res.*, **102**, 5005-5017, (1997).

### Figure Captions

**Figure 1.** South (a) and North (b) Patagonia icefields [Naruse *et al.* 1995].

**Figure 2.** Two types of chronology parameterizations assumed for the mid-late Holocene retreats and advances. Some of the main differences between Neoglaciation scenarios 1 and 2 (frames a and b, respectively) are as follows: (1) Type 1 includes an early advancement (phase I) beginning at 5 and ending at 4 ka BP, a period of sustained minimal glaciation between 2.1 and 0.6 ka BP and a 150 year long maximal glacial volume sustained during the years 1700 to 1850 AD. The second, third and fourth (II, III and IV, respectively) coincide to the three Neoglacial chronologies adopted by Mercer [1970]. (2) Type 2 scenarios have Neoglacial oscillations beginning at 4 ka BP, include a Neoglacial volume growth beginning at 400 and ending at 1050 AD and a linear build up of volume during the LIA (phase IV) from 1400 to 1880 AD. Type 2 chronology coincides with a recent estimate of Aniya [1995] for the Tyndall and Upsala glaciers. Type 1 assumes a constant volumetric rate  $\dot{V}_A$  in accordance with the observations of Aniya *et al.* [1996; 1997] whereas Type 2 also considers a slow recession phase during 1880 to 1960 followed by an accelerated phase at rate  $\dot{V}_{Aa}$  (at the minimum and maximum volumetric rates determined by Aniya *et al.* [1997], respectively, see Table 1, for typical values assumed in this study). We find that the sensitivity of the predicted present-day rebound signal to  $\dot{V}_{Aa}$  and  $\dot{V}_A$  is substantially smaller than anticipated.

**Figure 3.** Basic model parameters for Earth structure and square-edged cylindrical disk load.

**Figure 4.** Model load height variation as a function of time. Case (a) shows an arbitrary history with a period of readvancement. Cases (b) and (c) show approximate histories that can be used for benchmarking the theory and computer code by comparison to the results of Wolf [1985a]. Cases (b) and (c) differ in that the model evaluation time  $t$  (see tick marks on time-axis) in (c) must include the direct elastic effect of the load, while in case (b) only viscoelastic effects are present.

**Figure 5.** Vertical velocity in mm/yr due to elastic deformation in response to present-day ice recession. The elastic rigidities and densities are given in Table 3. Here the maximum glacial recession estimates from Aniya *et al.* [1997] for the period 1944/45 to 1985/86 are assumed to continue to the present-day. The SPI loss rate estimate is applied to the entire icefield system as idealized by the circular (square-edged) disks as shown. This elastic response is implicit in all computations with a viscoelastic mantle (half-space) included. Here positive-valued contours indicate ongoing uplift.



**Figure 6.** Predicted vertical velocity (mm/yr) for the two load histories of Figure 2. Unlike Figure 5, mantle viscoelastic deformation is accounted for. Frame (a) assumes a "Type 1" load history and (b) assumes "Type 2" with a uniform volumetric loss rate (as in Figure 5) since AD 1850 and 1880 (see Figures 2a and 2b, respectively). Structure parameters are given in Table 3. Here negative-valued contours indicate the prediction of ongoing subsidence. The assumed lithosphere/mantle structure is of 'Fennoscandian' type (see section 6.2 of text).

**Figure 7.** Predicted vertical velocity (mm/yr) for "Type 2" load as in Figure 6a with a smaller mantle viscosity ( $\eta = 1.0 \times 10^{20}$  Pa s). All other Earth structure and load parameters are identical to those assumed in Figure 6. The assumed lithosphere/mantle structure is of 'Australian' type.

**Figure 8.** Partitioned vertical rate predictions at locations shown in Figure 7. The partition assumes all three Neoglacials (I through III) plus LGM for pre-1400 load and only the LIA (IV) for post-1400 load.

**Figure 9.** Refined partitioning of vertical rate responses for the LIA load (post-1400) alone. The partition is used for analysis of vertical rate predictions for viscosities  $\eta \leq 1.0 \times 10^{20}$  Pa s. Note that the growth phase, when taken alone, should predict ongoing rebound (uplift), entirely analogous to classic near-field post-glacial rebound due to deglaciation from late-Pleistocene LGM.

**Figure 10.** LIA vertical rates predicted assuming the partitions shown in Figure 9. The white line in the bar graph for Type 2 in the left of each frame corresponds to a growth phase concluded at AD 1850, as in all Type 1 cases. The location termed 'inner depression' is identical to that assumed for Figure 8. Note that the 'outer bulge zone' and 'inner depression' are analogous to 'Zones 1 and 2' for post-glacial isostatic emergent and collapsing forebulge coastal sites, respectively, as defined by Clark [1980]. Mapviews of the total Neoglacial plus LGM predictions at present-day are shown in Figure 11.

**Figure 11.** Predicted vertical velocity for Type 1 (a and b) and Type 2 (c and d) at two relatively low mantle viscosity values. Cases (a) and (c) assume  $\eta = 2.0 \times 10^{19}$  Pa s while cases (b) and (d) assume  $\eta = 1.0 \times 10^{19}$  Pa s with  $h = 35$  km. The cases correspond to Figure 10, but are shown in mapview and show the total of all components on the predicted present-day rate. The assumed lithosphere/mantle structure is of 'Basin and Range' type.

**Figure 12.** Predicted vertical velocity for  $h = 25$  km. The viscosity is the same as in cases (b) and (d) of Figure 11 ( $\eta = 1.0 \times 10^{19}$  Pa s). Cases (a) and (b) assume load Type 1 and 2, respectively. Case (c)

assumes Type 2, but with the Neoglacial IV (see Figure 2) maximum centered at the year AD 1700. Direct comparison of Figure 12a with 11b reveals an enhanced outer bulge evolution in the thinner lithosphere case.

**Figure 13.** Predicted vertical velocity for cases identical to (a) and (b) of Figure 12, but with viscosity reduced by a factor of 2.

**Figure A-1.** Relaxation spectra for half-space viscosity  $\eta = 0.75 \times 10^{21} \text{ Pa} \cdot \text{s}$  and  $h = 100 \text{ km}$  (elastic layer thickness). The wave number  $n$  is identical to that employed by *Wolf* [1985a] in which  $n(k') = k' \cdot (R/h)$ , where  $R$  is the Earth's radius. Solid line is  $\gamma_1$  and dashed for  $\gamma_2$ . Note the near degeneracy for  $n > 3 \times 10^2$ . Model density structure is  $\rho_1 = 2.9 \text{ gm/cm}^3$  and  $\rho_2 = 3.9 \text{ gm/cm}^3$ . Elastic shear moduli are  $\mu_1^f = 44.1 \text{ GPa}$  and  $\mu_2^f = 75.0 \text{ GPa}$ .

**Figure A-2.** Surface vertical displacement field,  $w_0(r, t)$ , for benchmark comparison case (a). Load history is simulated as in Figure 4b with  $\alpha = 600 \text{ km}$ ,  $t_1 = 1.0$ ,  $t_2 = 2000.0$ ,  $t_3 = 2000.1$  (units ka) and  $h_{0,1} = h_{0,2} = 2.0 \text{ km}$ ,  $h_{0,3} = 0.0 \text{ km}$  with  $\rho_0 = 1.0 \text{ gm/cm}^3$ . Assumed Earth model parameters are  $h = 100 \text{ km}$ ,  $\rho_1 = 3.36 \text{ gm/cm}^3$ ,  $\rho_2 = 3.38 \text{ gm/cm}^3$ ,  $\mu_1^f = 67 \text{ GPa}$ ,  $\mu_2^f = 145 \text{ GPa}$  and  $\eta = 1.0 \times 10^{21} \text{ Pa} \cdot \text{s}$ . Frame (b) shows rates at same set of times as (a) after complete load removal: 2 ka (solid curve), 5 ka (double short, single long dashed curve) and 10 ka (even dashed curve). Frame (c) shows vertical displacement for a load history as in Figure 4b with  $t_1 = 10^{-4}$ ,  $t_2 = 2 \times 10^{-4}$ ,  $t_3 = 2500 \text{ ka}$  and  $h_{0,2} = h_{0,3} = 3.0 \text{ km}$ ,  $h_{0,1} = 1.5 \text{ km}$ . Frame (c) has all parameters identical to (a) and (b) except  $\alpha = 800 \text{ km}$ ,  $\rho_1 = 3.32 \text{ gm/cm}^3$  and  $\rho_2 = 3.34 \text{ gm/cm}^3$ . Evaluation times in frame (c) are  $t = 3 \times 10^{-4}$  ( $\approx 0$ ),  $t = 1.0003$  and  $t = 2400 \text{ ka}$  ( $\approx \infty$ ) with solid, double short and single dashed curves for progressively longer evaluation times, respectively. (Also see Figure 10 of *Wolf* [1985a] and Figure 6 of *Wolf* [1984] for comparison). Frames (a)-(c) assume square-edged disk load in contrast to (d) for a load of elliptical cross section. Frame (d) has all other parameters identical to (c).

**Figure A-3.** Comparison of spherical and flat-earth model computation. Load build up phase assumes zero height at 108 ka BP with subsequent linear ramp to ICE-3G heights at 18 ka. All subsequent load history is identical to ICE-3G as in *Tushingham & Peltier* [1991].  $\rho_0 = 1.0 \text{ g/cm}^3$ . Load heights are zero after 15 ka. The Earth parameters assumed are  $h_1 = 100 \text{ km}$ ,  $\eta = 1.0 \times 10^{21} \text{ Pa} \cdot \text{s}$ ,  $\mu_1^f = 67.0 \text{ GPa}$ ,  $\mu_2^f = 145.0 \text{ GPa}$ ,  $\rho_1 = 3.38 \text{ g/cm}^3$ ,  $\rho_2 = 3.39 \text{ g/cm}^3$  and  $g = 9.832186 \text{ m/sec}^2$ . Frame (a) shows the difference in vertical displacement at 13 ka. Frame (b) shows the amplitude and sign of the solution for flat-earth assumption. Frames (c) and (d) show the present-day uplift rate for spherical and flat-earth models, respectively. Spherical harmonic truncation level is  $n = 240$ . Note the remarkable similarity of the rate of uplift magnitude and pattern in frames (c) and (d).

**Table 1.** Terms forming  $\gamma_p$  and  $\xi_p$ .

$n$	$\hat{a}_n$
0	$4 \frac{\mu_1^e}{\mu_2^e} k'^2 \left[ 1 + e^{4k'} + 2 e^{2k'} (1 + 2 k'^2) \right]$
1	$2 \rho_1 \frac{g}{\mu_2^e} \frac{h}{\mu_2^e} k' (1 - e^{4k'} + 4k' e^{2k'})$
2	$8 \left( \frac{\mu_1^e}{\mu_2^e} k' \right)^2 (-1 + e^{k'}) (1 + e^{k'}) (1 + e^{2k'})$
3	$2k' \frac{g}{\mu_2^e} \frac{h}{\mu_2^e} \frac{\mu_1^e}{\mu_2^e} \left[ (\rho_1 + \rho_2)(1 + e^{4k'}) + 2(\rho_2 - \rho_1) e^{2k'} (1 + 2k'^2) \right]$
4	$\left( \frac{g}{\mu_2^e} \frac{h}{\mu_2^e} \right)^2 \rho_1 (\rho_2 - \rho_1) (1 - e^{4k'} + 4k' e^{2k'})$
5	$4k'^2 \left( \frac{\mu_1^e}{\mu_2^e} \right)^3 (1 - e^{2k'} - 2k' e^{k'}) (1 - e^{2k'} + 2e^{k'} k')$
6	$2k' \left( \frac{\mu_1^e}{\mu_2^e} \right)^2 (1 - e^{4k'} - 4e^{2k'} k') \frac{g}{\mu_2^e} \frac{h}{\mu_2^e} \rho_2$
7	$\frac{\mu_1^e}{\mu_2^e} \left[ \frac{g}{\mu_2^e} \frac{h}{\mu_2^e} (1 - e^{k'}) (1 + e^{k'}) \right]^2 \rho_1 (\rho_2 - \rho_1)$
8	$-2k' \left\{ 1 + e^{2k'} \left[ 1 + 2k' (1 + k') \right] \right\}$
9	$4k' \frac{\mu_1^e}{\mu_2^e} - \frac{g}{\mu_2^e} \frac{h}{\mu_2^e} (\rho_2 - \rho_1) \left\{ 1 + e^{2k'} \left[ 1 + 2k' (1 + k') \right] \right\}$
10	$-2k' \left( \frac{\mu_1^e}{\mu_2^e} \right)^2 \left[ 1 - e^{2k'} - 2k' e^{2k'} (1 + k') \right]$
11	$\frac{g}{\mu_2^e} \frac{h}{\mu_2^e} \frac{\mu_1^e}{\mu_2^e} (\rho_2 - \rho_1) \left[ 1 - e^{2k'} (1 + 2k') \right]$

**Table 2. Dimensionless free modes  $p = 1$  and  $p = 2$ .**

---


$$\hat{\beta} = \hat{a}_0 - \hat{a}_1 + \hat{a}_2 + \hat{a}_3 - \hat{a}_4 + \hat{a}_5 - \hat{a}_6 + \hat{a}_7$$

$$\hat{\beta} a_0 = \hat{a}_{10} + \hat{a}_{11}$$

$$\hat{\beta} a_1 = 2 (\hat{a}_{10} + \hat{a}_{11}) + \hat{a}_9$$

$$\hat{\beta} a_2 = \hat{a}_8 + \hat{a}_9 + \hat{a}_{10} + \hat{a}_{11}$$

$$\hat{\beta} b_0 = \hat{a}_5 - \hat{a}_6 + \hat{a}_7$$

$$\hat{\beta} b_1 = \hat{a}_2 + \hat{a}_3 - \hat{a}_4 + 2 (\hat{a}_5 - \hat{a}_6 + \hat{a}_7)$$


---



---

inverse decay time

---


$$\gamma_p = \frac{b_1 \pm \sqrt{b_1^2 - 4b_0}}{2}$$


---



---

amplitude factors

---


$$\xi_p = \frac{(-1)^p}{\gamma_2 - \gamma_1} \left[ \gamma_p (a_1 - a_2 \gamma_p) - a_0 \right]$$

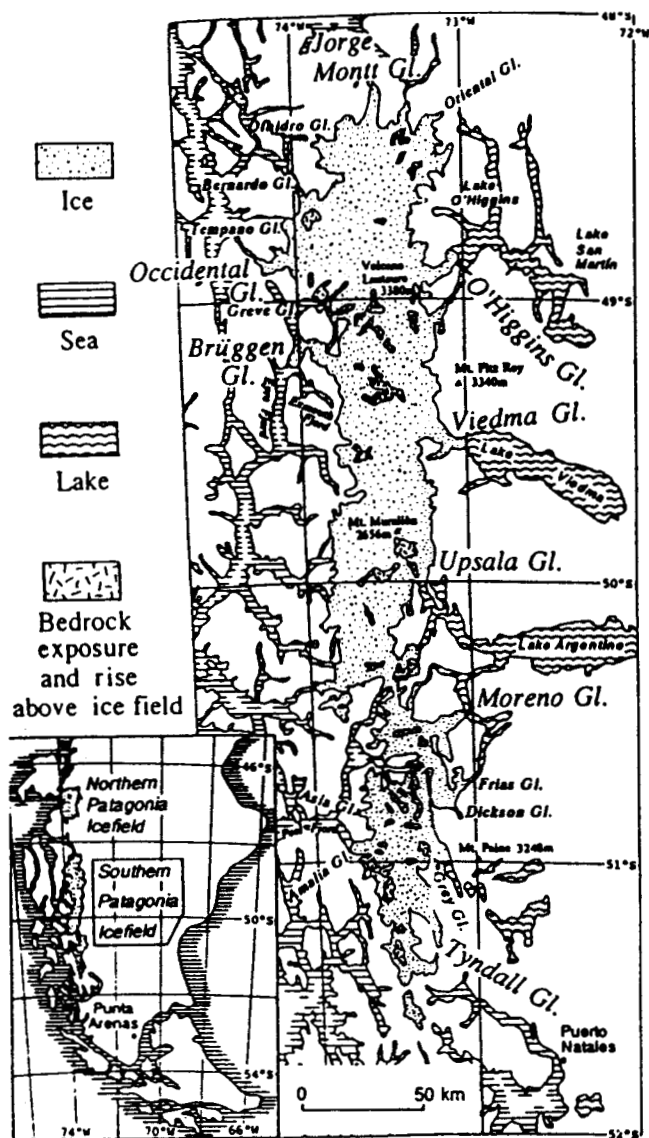

---



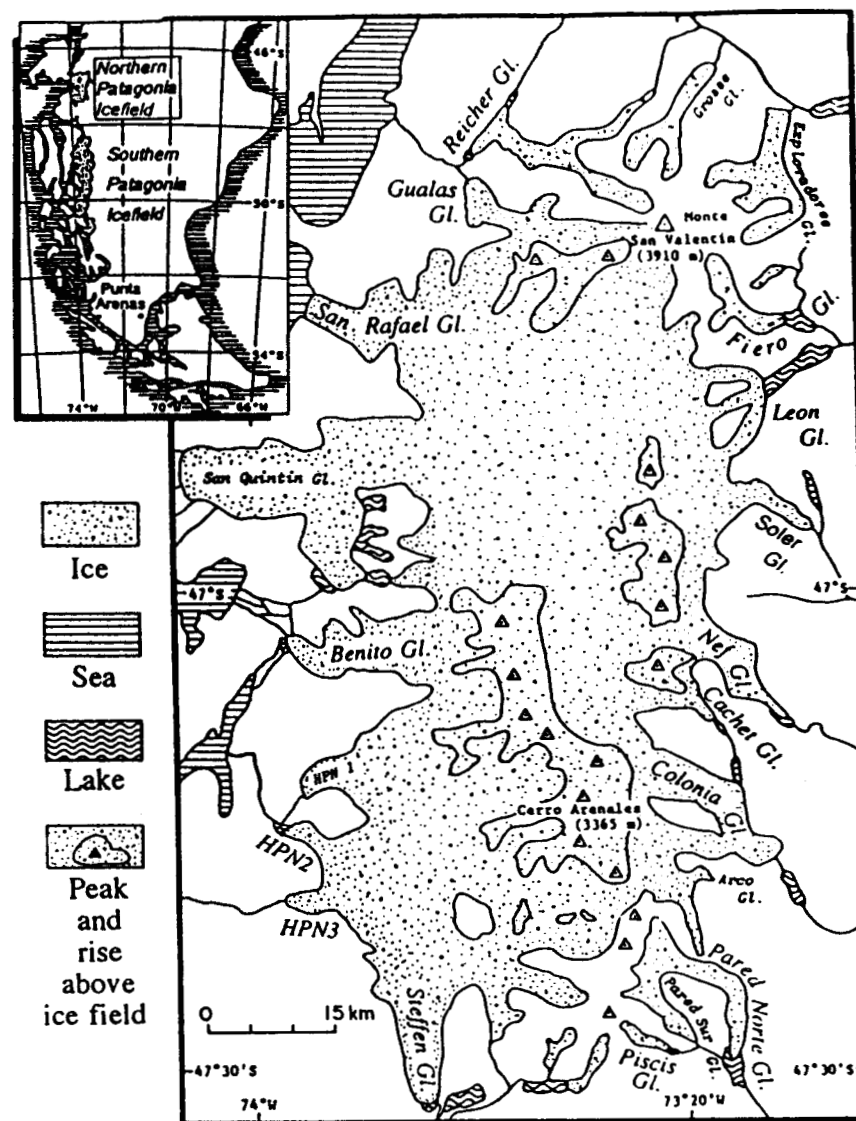
---

**Table 3. Model Mechanical Parameters**

symbol	definition	model value
$\rho_{ice}$	ice density	917.0 kg/m <sup>3</sup>
$\rho_1$	lithospheric density	3380.0 kg/m <sup>3</sup>
$\rho_2$	mantle (half-space) density	3590.1 kg/m <sup>3</sup>
$g$	uniform gravity	9.832186 m/sec <sup>2</sup>
$\mu_1^f$	lithospheric elastic rigidity	67 GPa
$\mu_2^f$	mantle (half-space) elastic rigidity	145 GPa
$\eta$	mantle (half-space) viscosity	variable
$h$	lithospheric thickness	variable



(a)



(b)

Figure 1.

### Type 1 Neoglaciations

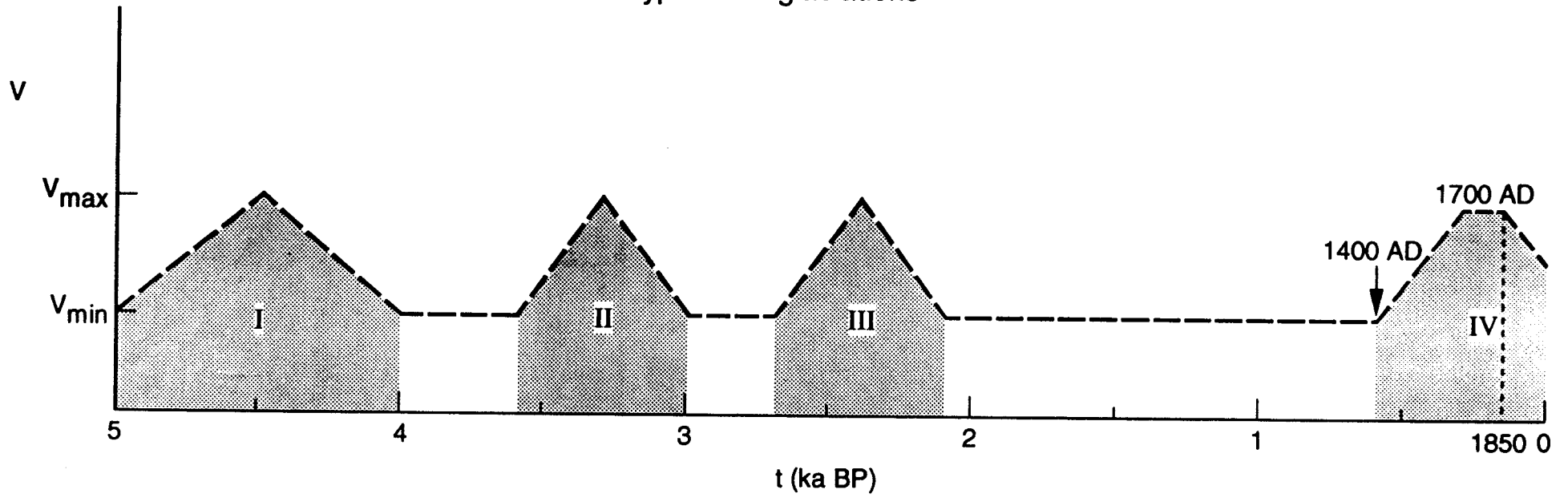


Figure 2a.

# Type 2 Neoglaciations

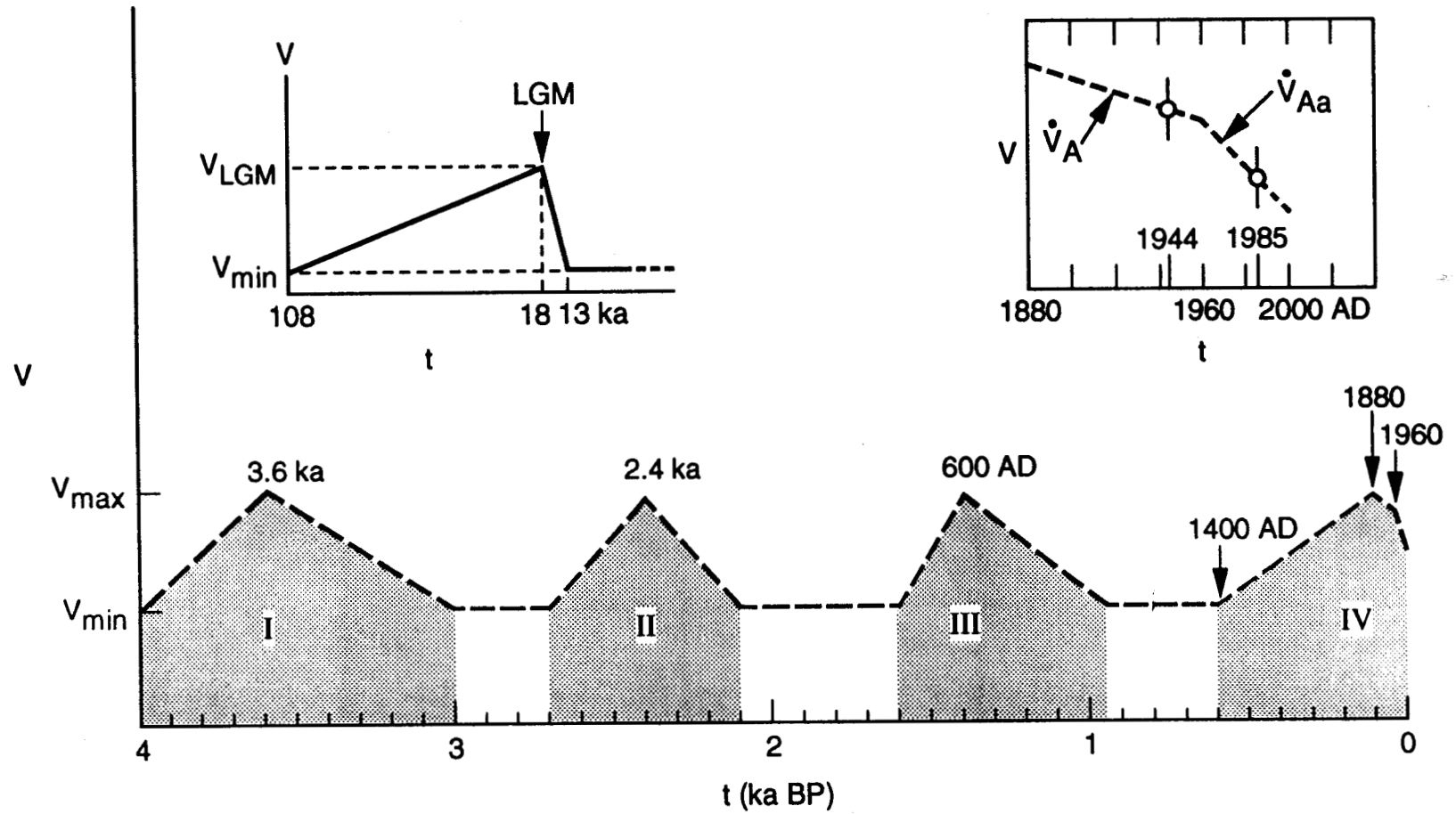
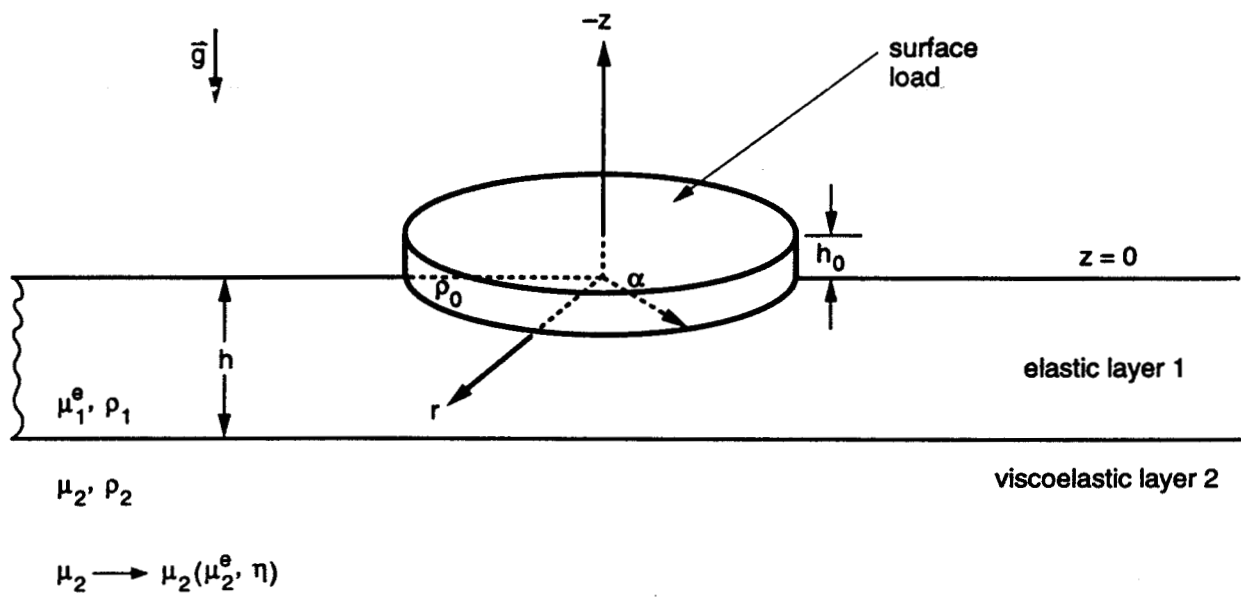


Figure 2b.





**Figure 3.**

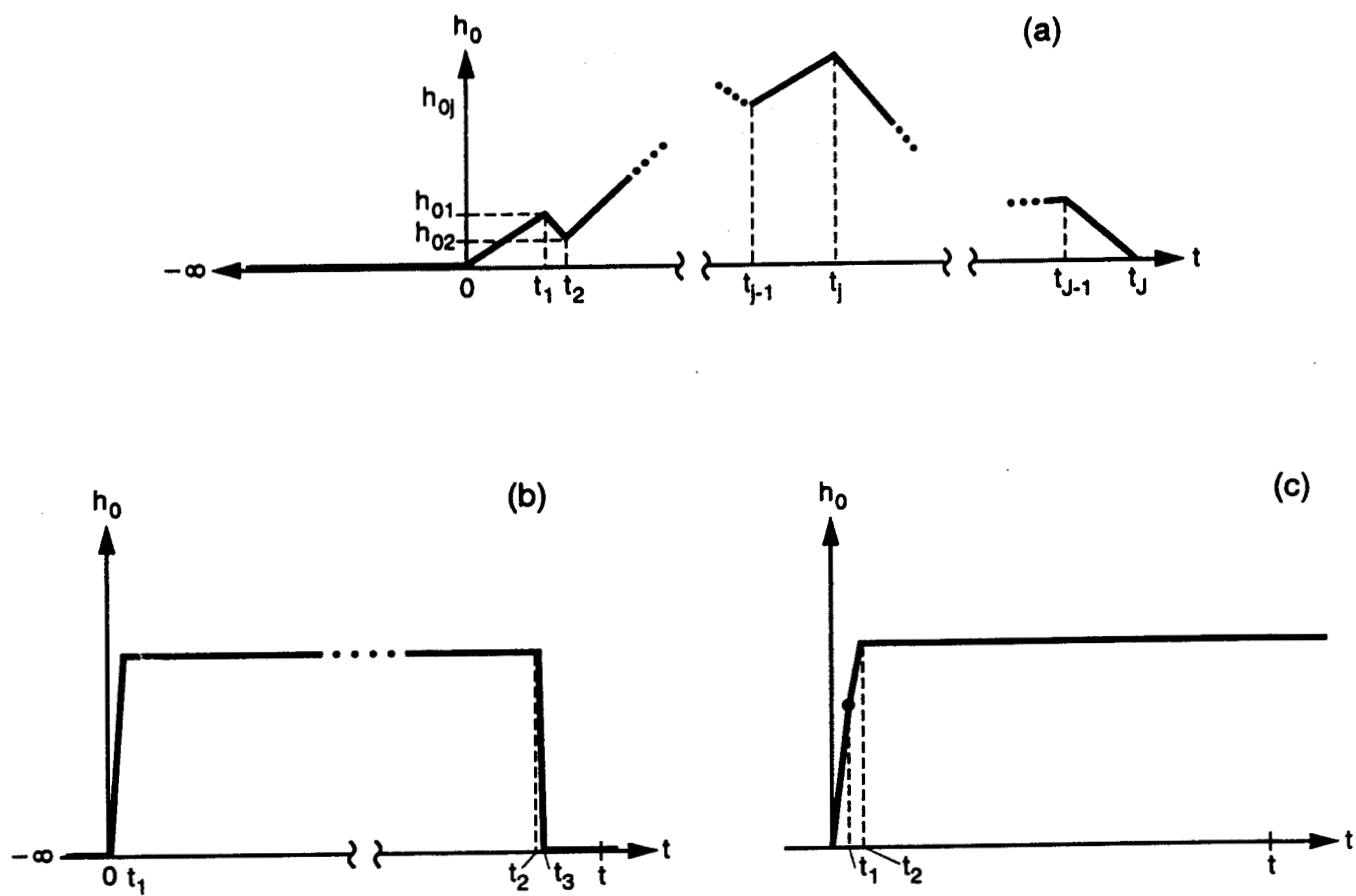


Figure 4

02/03/98

PD (2000 AD) vert disp. rate (mm/a) lith. th. = 65 km

DV = 10,000 cubic km. Type 1 loss rate = -9.27 c. km/yr infinite viscosity

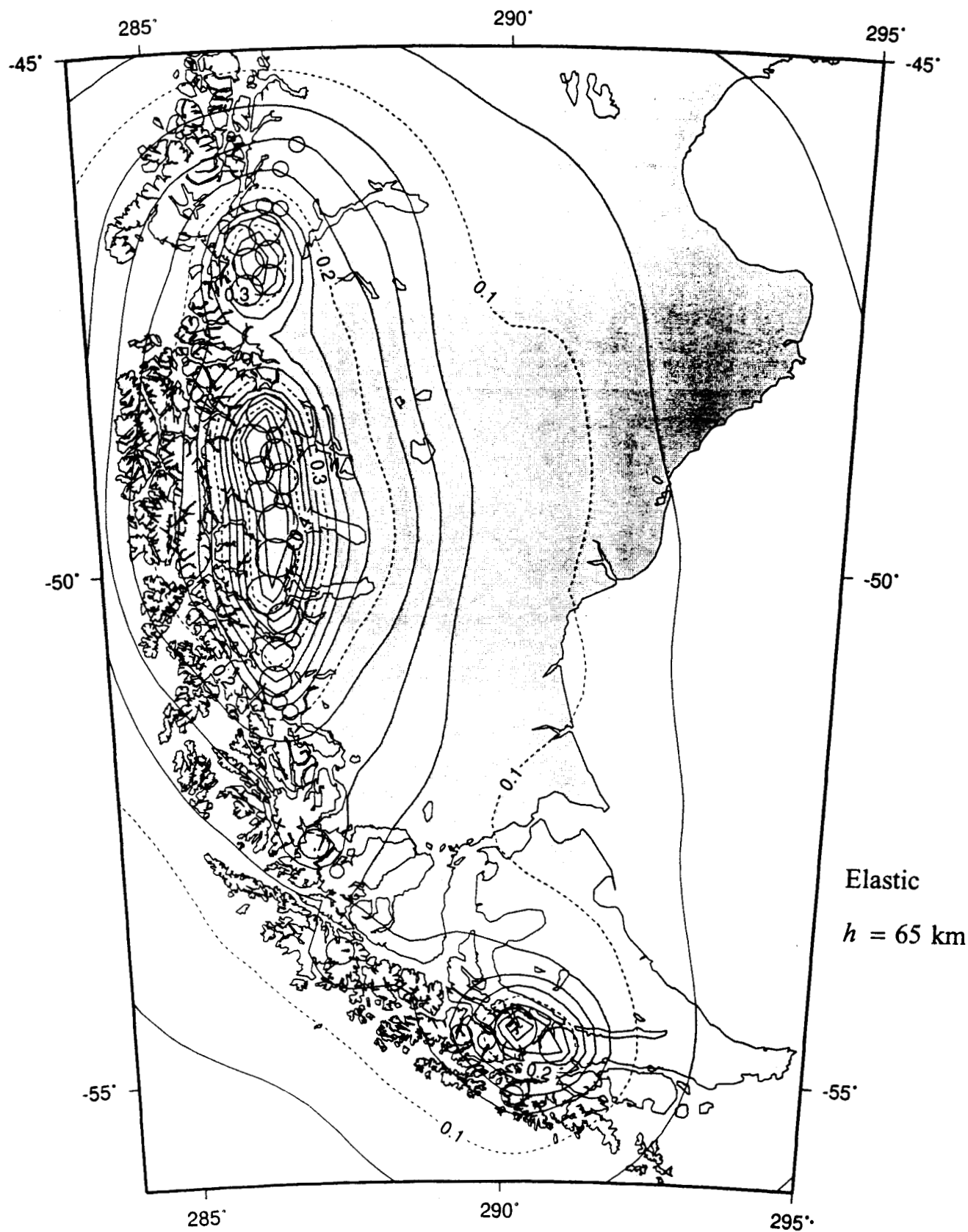
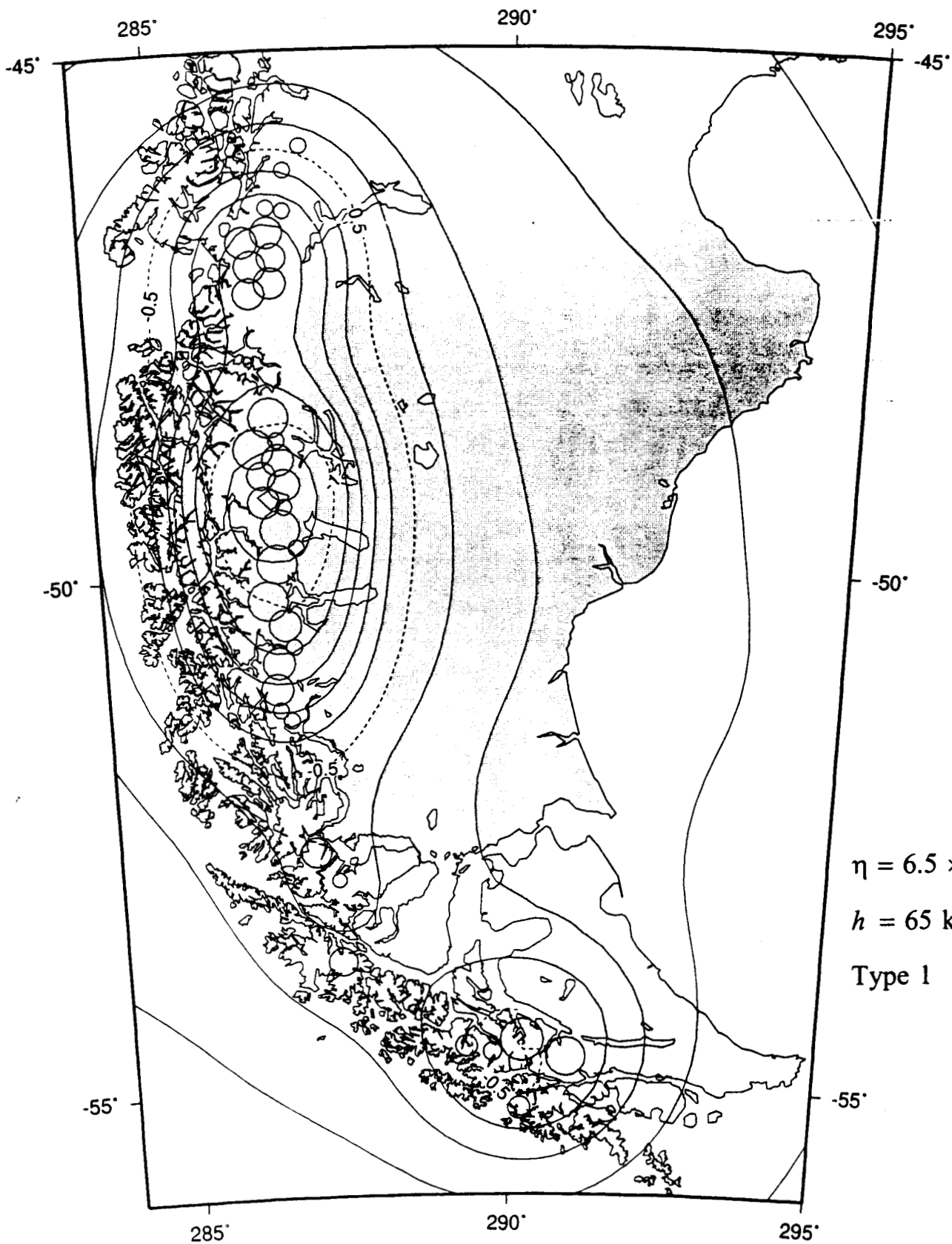


Figure 5.

$\eta = 6.5 \times 10^{20} \text{ Pa} \cdot \text{s}$   
02/03/98

PD (2000 AD) vert disp. rate (mm/a) lith. th. = 65 km

DV = 10,000 cubic km. Type 1 loss rate = -9.27 c. km/yr MFLB viscosity



$\eta = 6.5 \times 10^{20} \text{ Pa} \cdot \text{s}$

$h = 65 \text{ km}$

Type 1

Figure 6a.

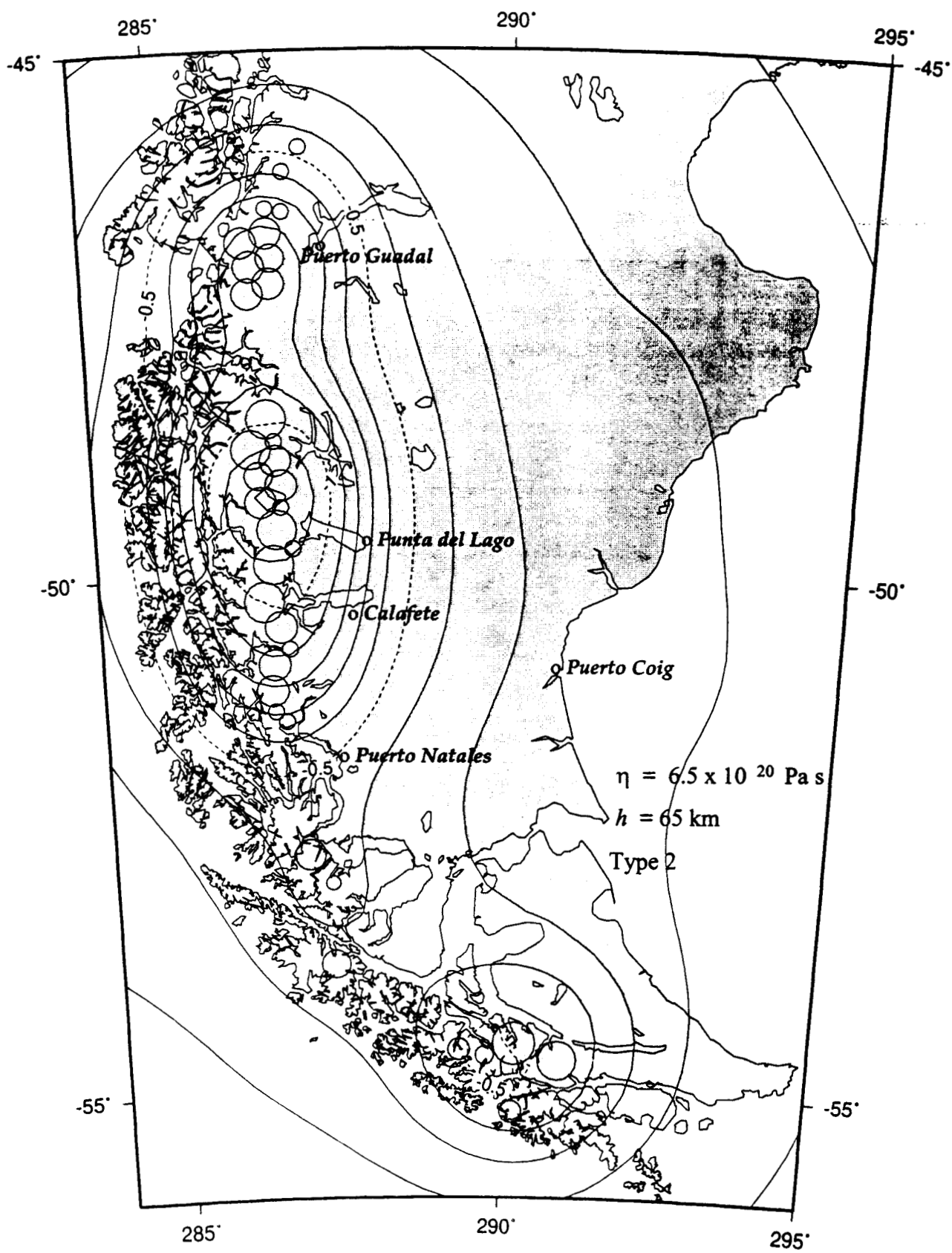


Figure 6b.

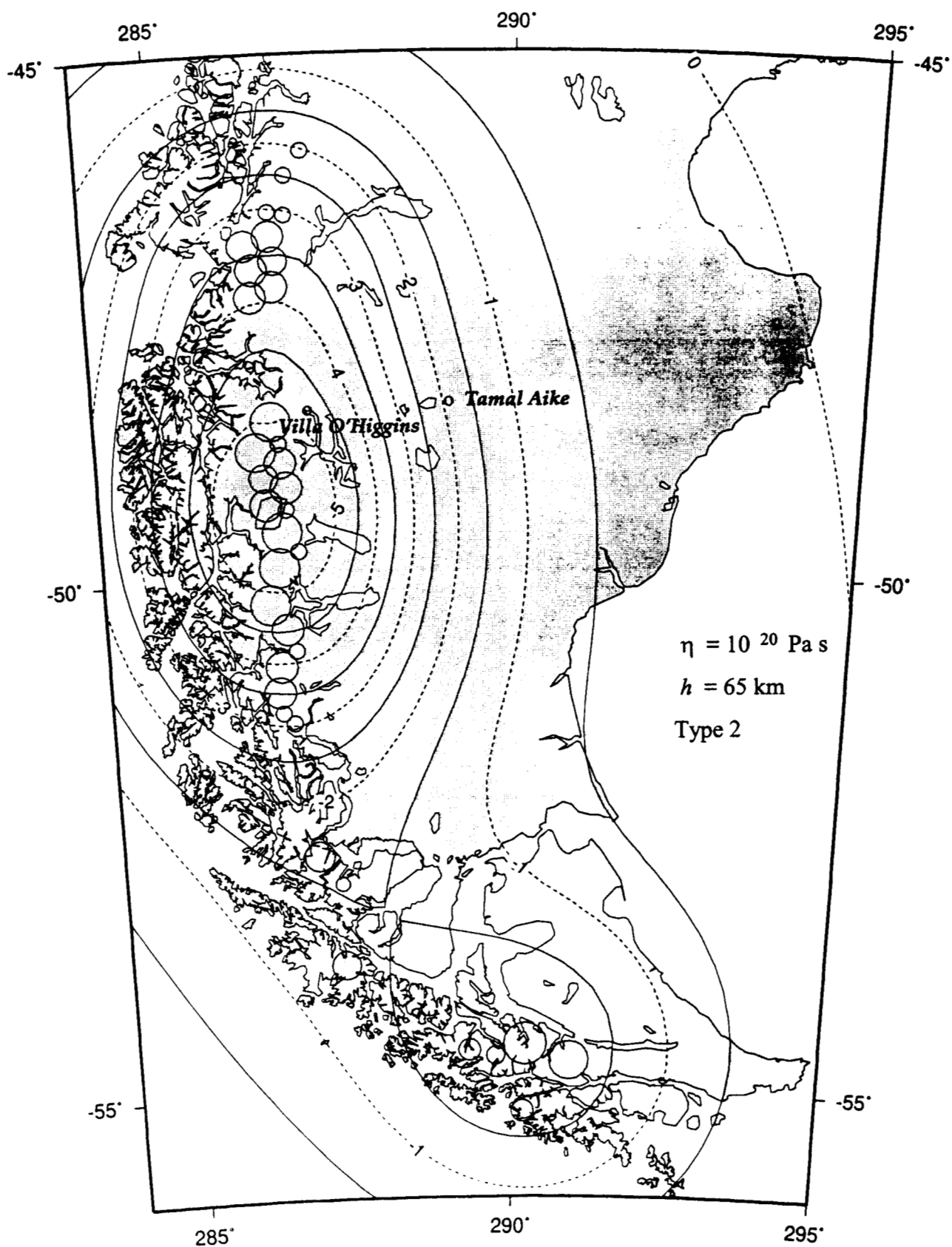


Figure 7.

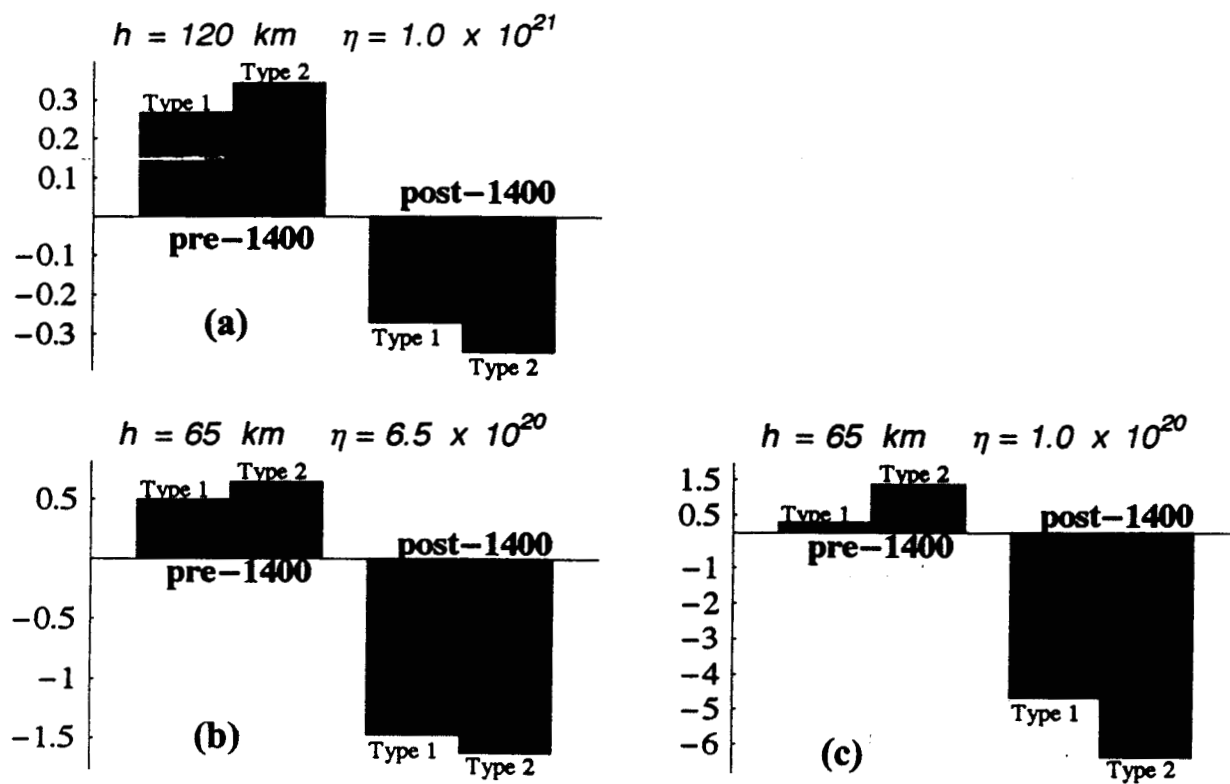
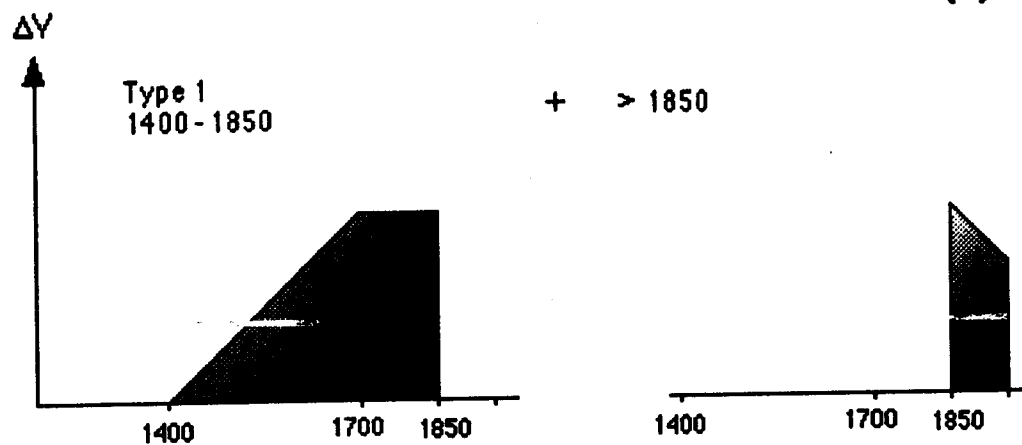


Figure 8.

(a)



(b)

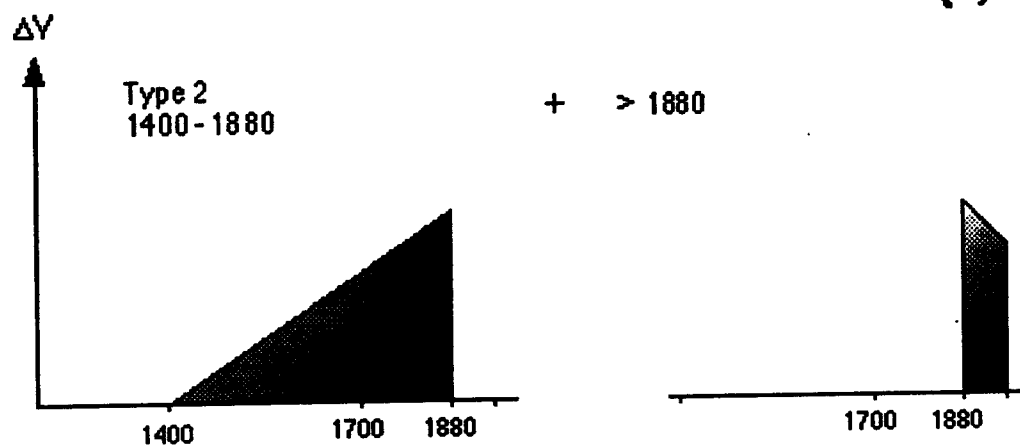


Figure 9



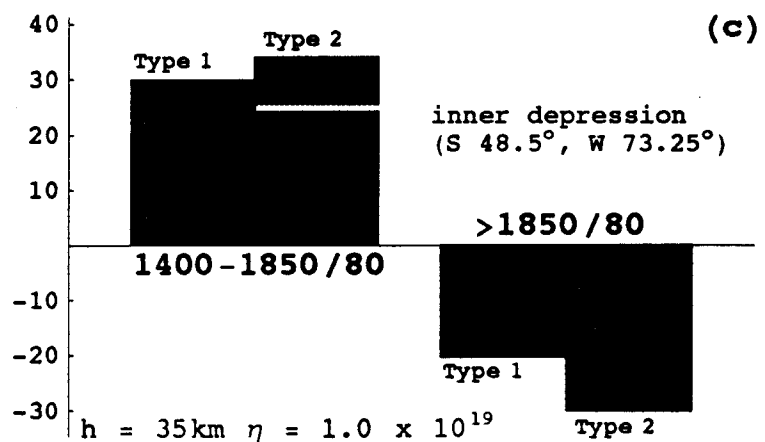
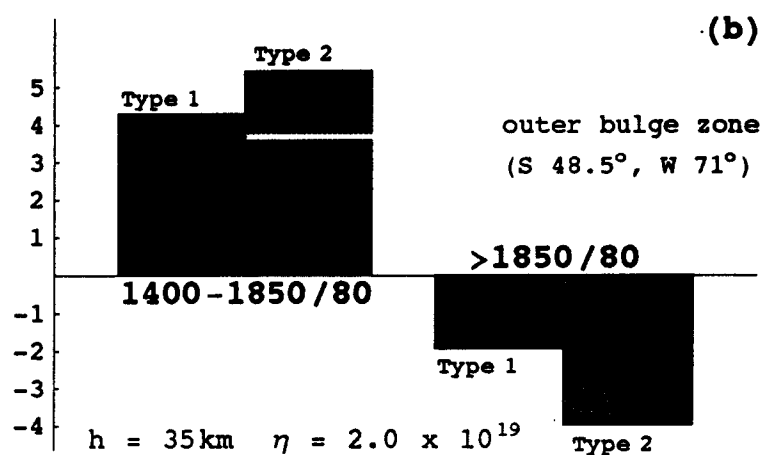
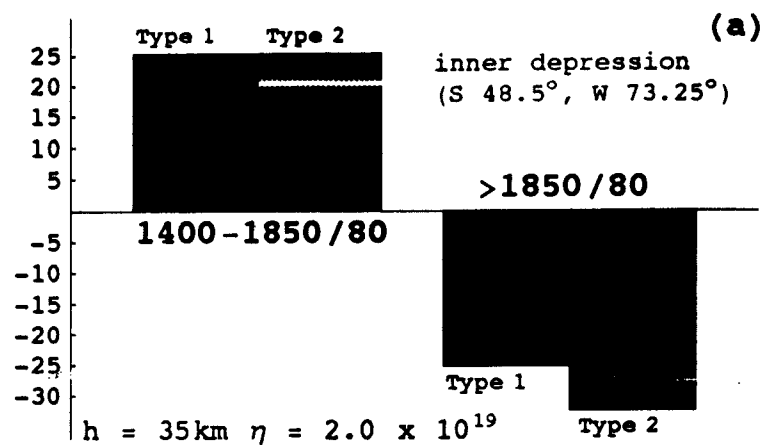


Figure 10.

PD (2000 AD) vert disp. rate (mm/a) lith. th. = 35 km  $\eta_{\text{hank}} = 512$

DV = 10,000 cubic km. Type 1 loss rate = -9.27 c. km/yr 1/50 H viscosity

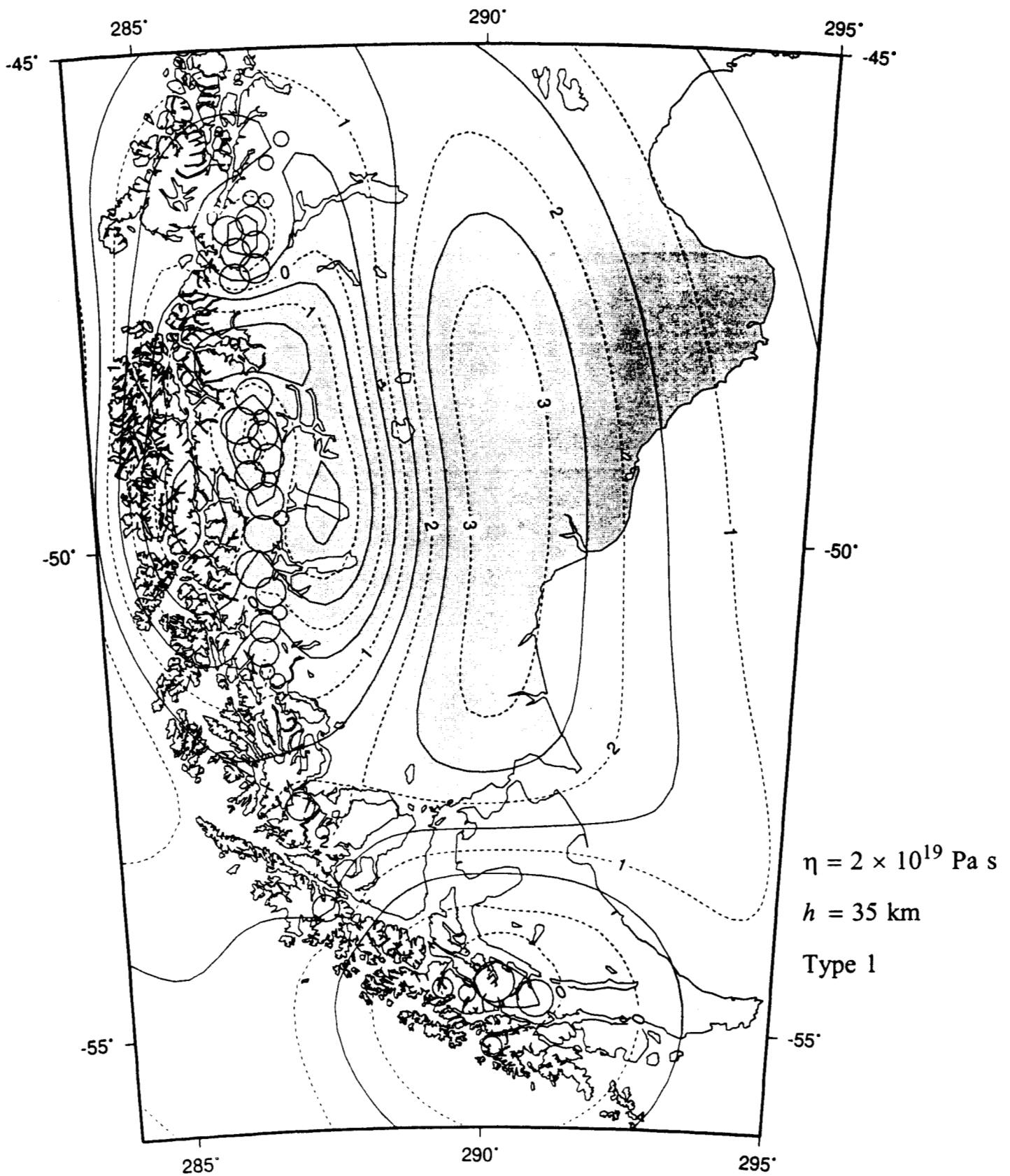


Figure 11a.

02/03/98

PD (2000 AD) vert disp. rate (mm/a) lith. th. = 35 km

DV = 10,000 cubic km. Type 1 loss rate = -9.27 c. km/yr 1/100 H viscosity

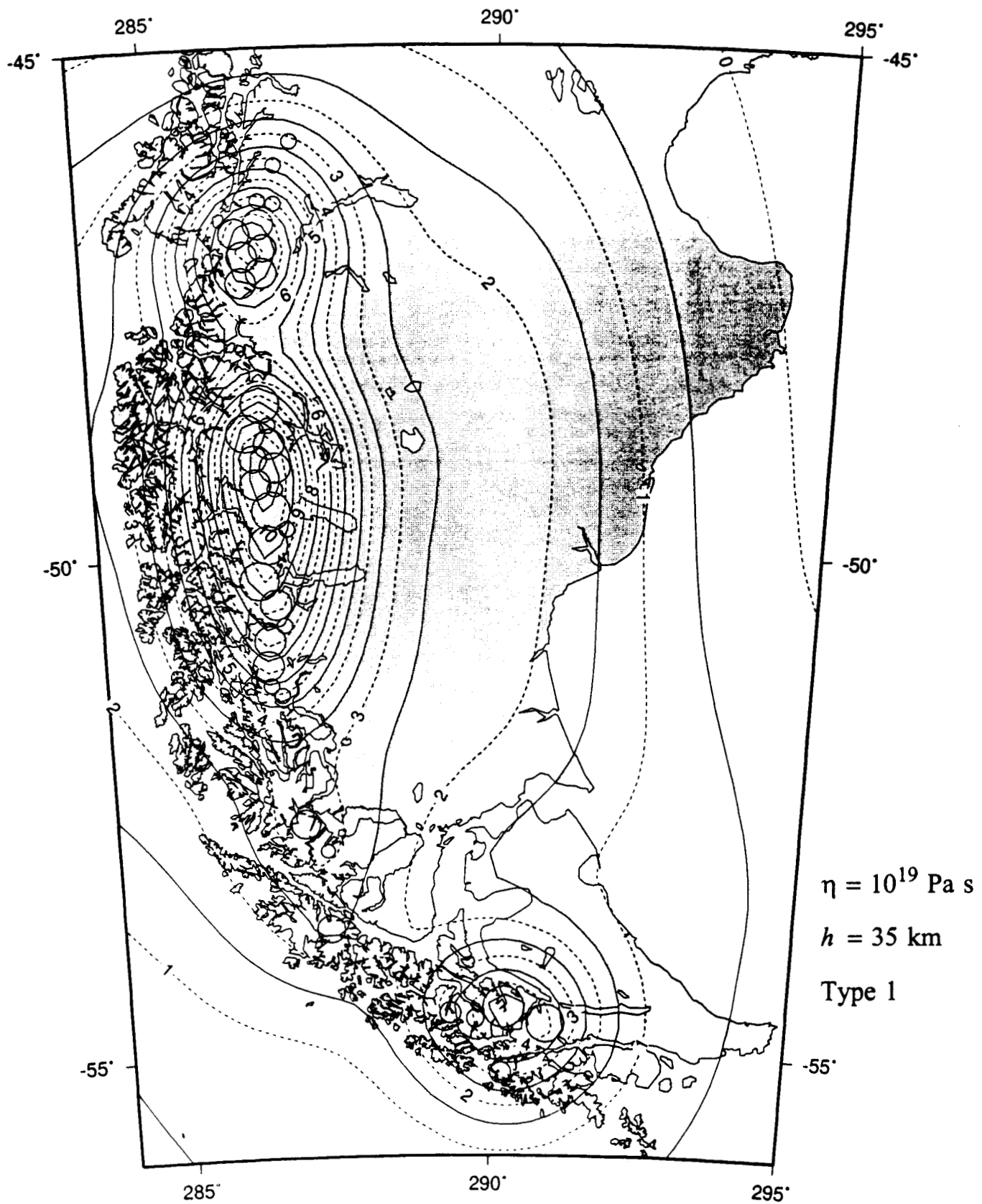


Figure 11b.

02/04/98

PD (2000 AD) vert disp. rate (mm/a) lith. th. = 35 km

DV = 10,000 cubic km. Type 2 loss rate = -9.27 c. km/yr 1/50 H viscosity

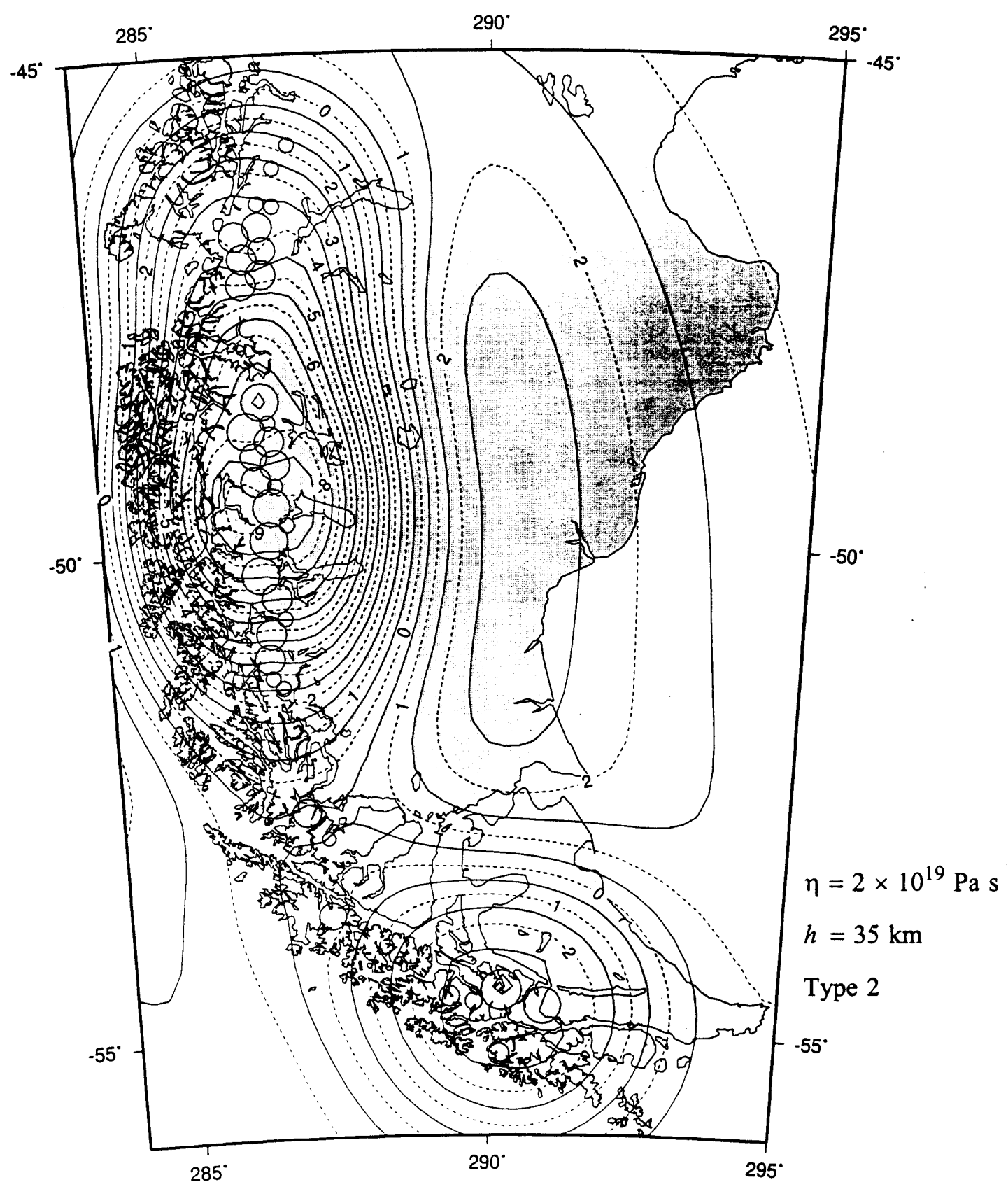


Figure 11c.

nr M2.33.6147.95  
02/04/98

PD (2000 AD) vert disp. rate (mm/a) lith. th. = 35 km

DV = 10,000 cubic km. Type 2 loss rate = -9.27 c. km/yr 1/100 H viscosity

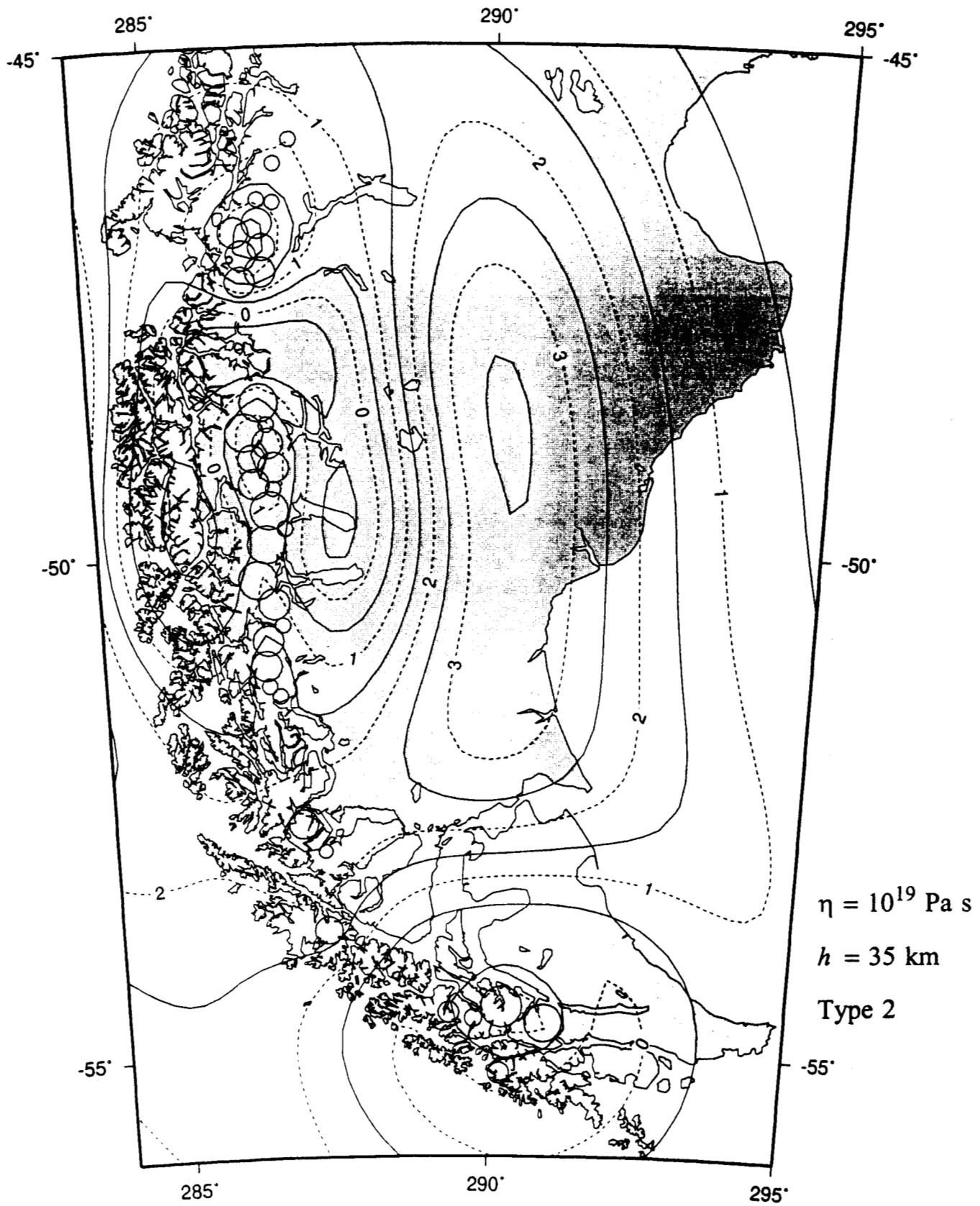


Figure 11d.

PD (2000 AD) vert disp. rate (mm/a) lith. th. = 25 km

DV = 10,000 cubic km. Type 1 loss rate = -9.27 c. km/yr 1/100 H viscosity

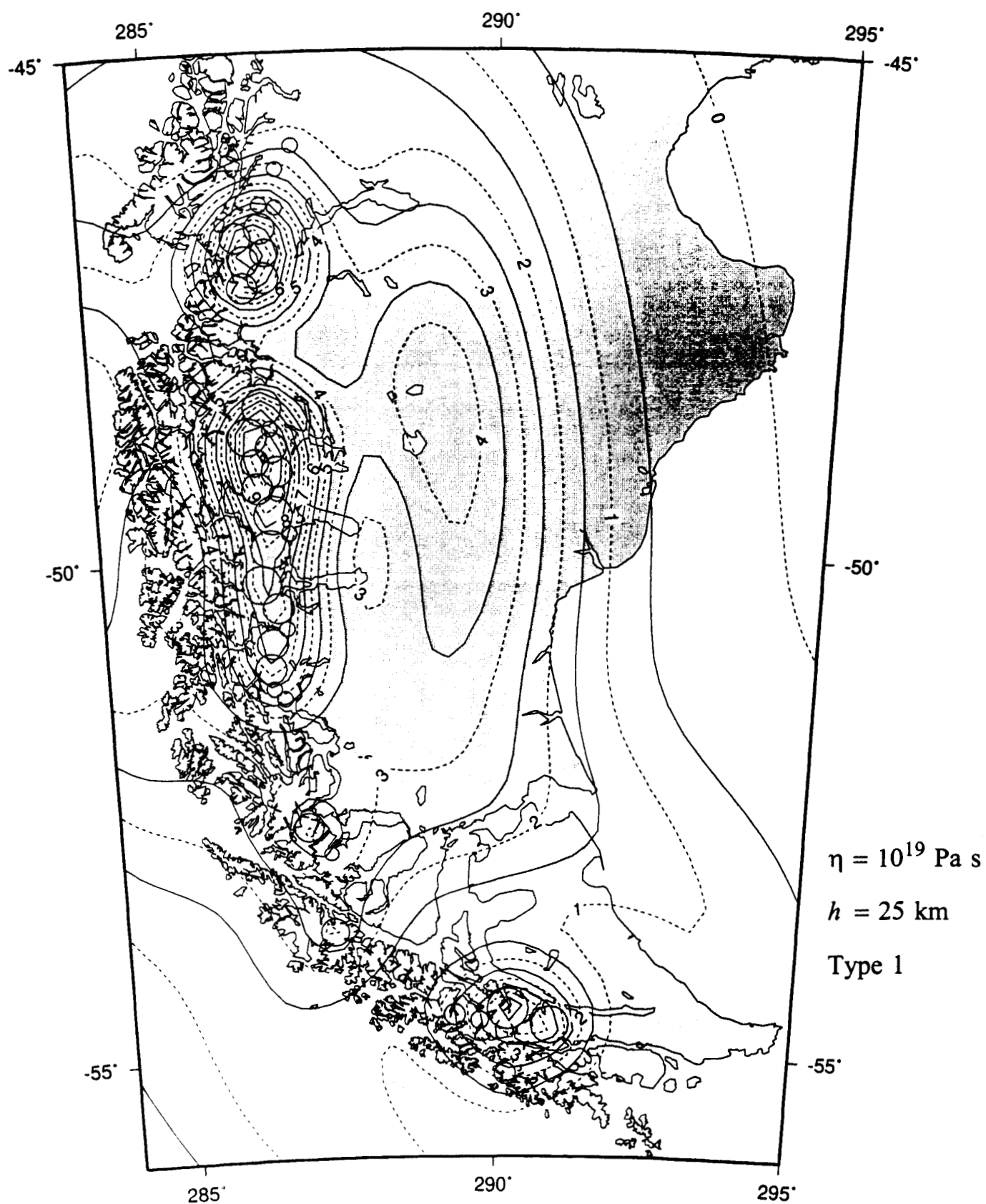


Figure 12a.

nr M2,25.01 H.r. ps  
02/04/98

PD (2000 AD) vert disp. rate (mm/a) lith. th. = 25 km

DV = 10,000 cubic km. Type 2 loss rate = -9.27 c. km/yr 1/100 H viscosity

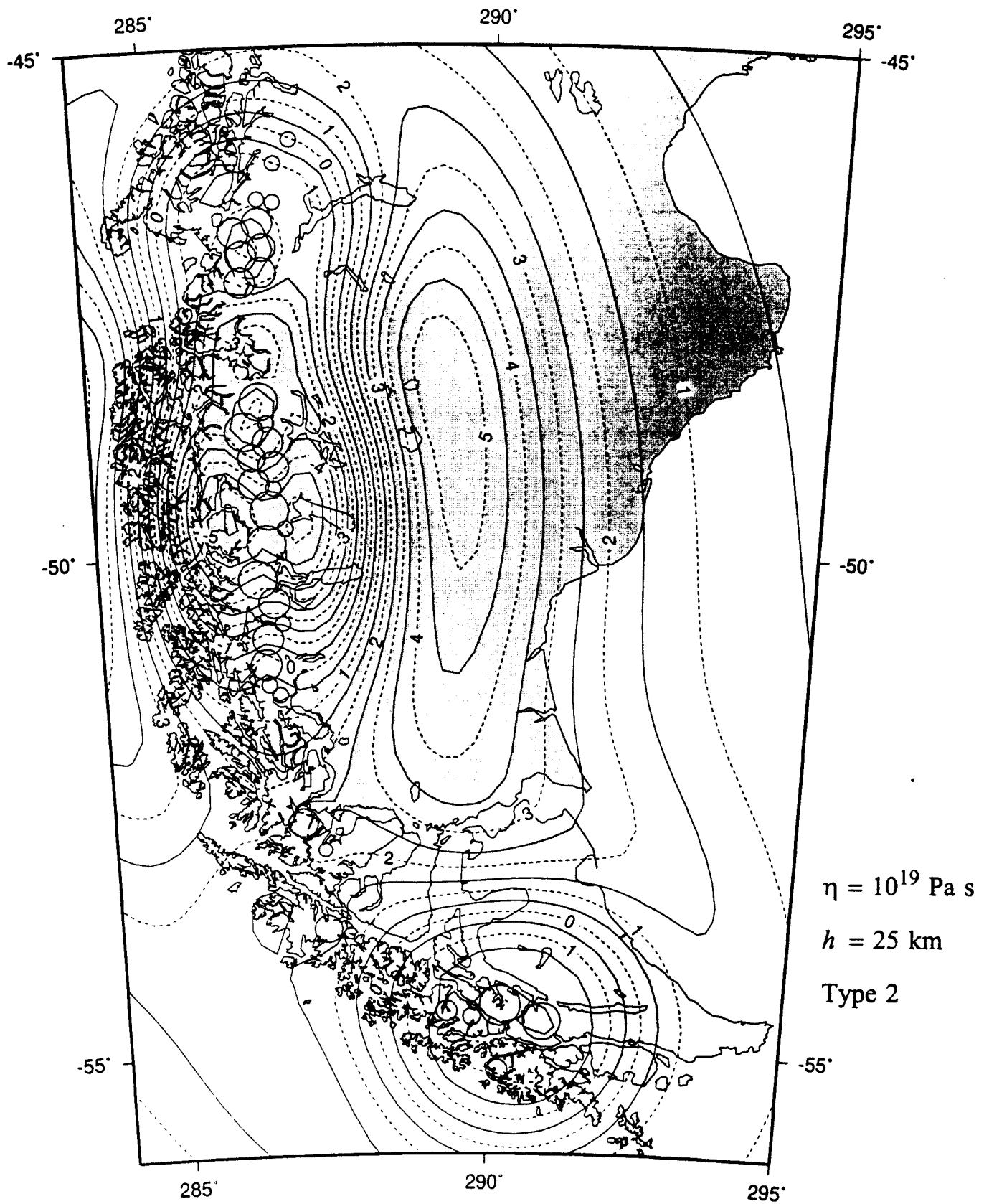


Figure 12b.

PD (2000 AD) v. rate (mm/a) lith. th. = 25 km LIA max. at 1700 AD

DV = 10,000 c. km. Type 2 loss rate = -9.27 c. km/yr 1/100 H viscosity

02/20/98

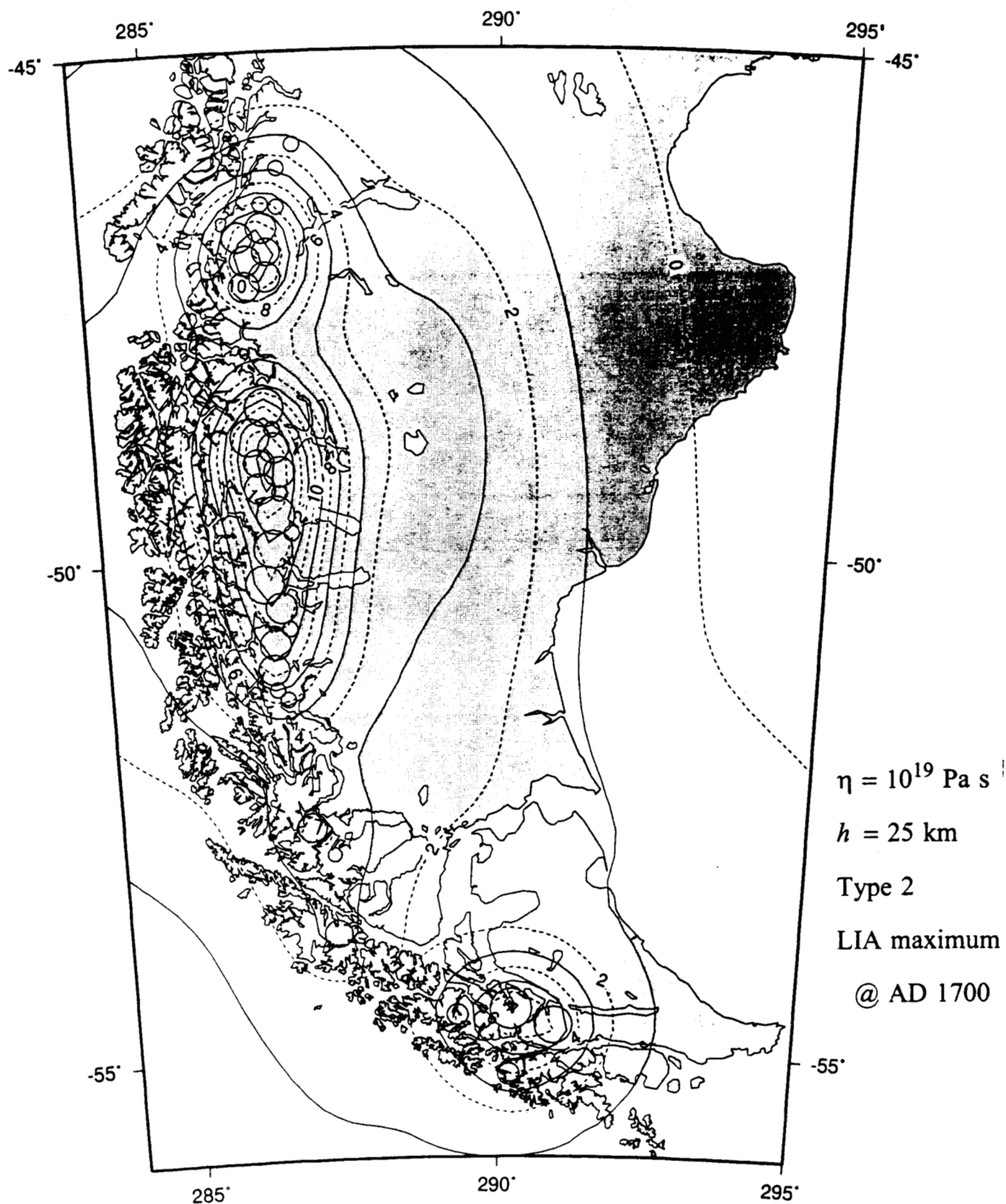


Figure 12c.



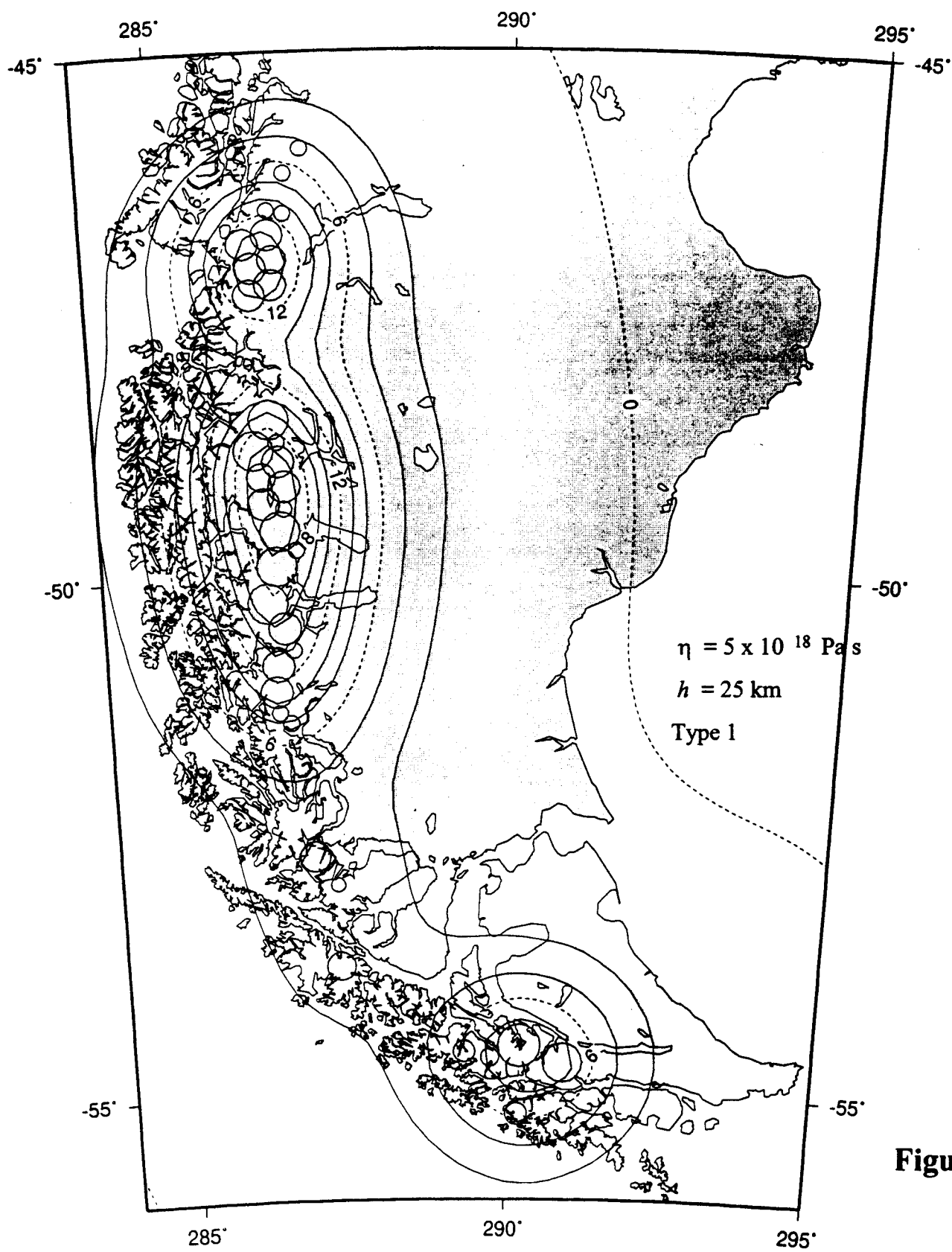
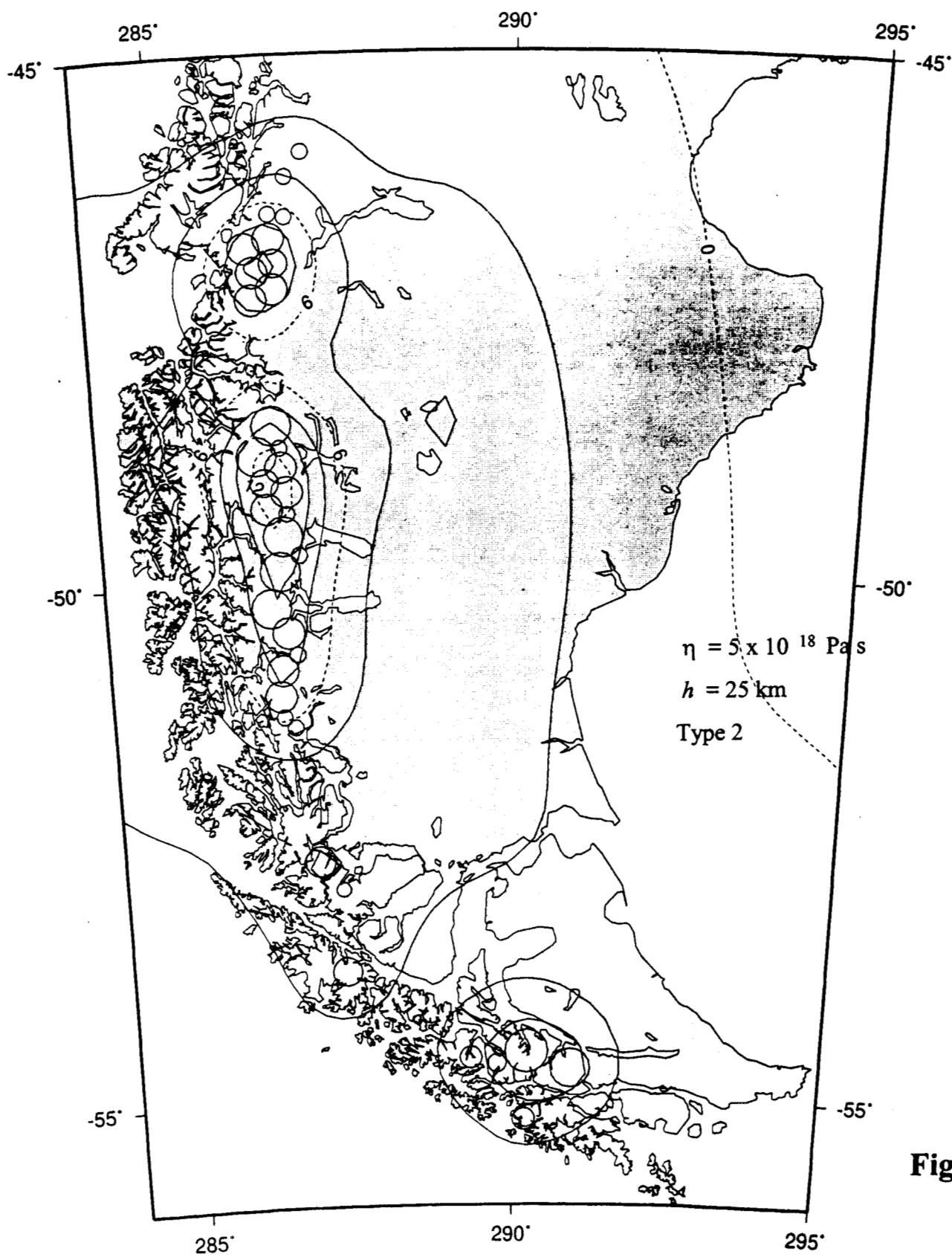
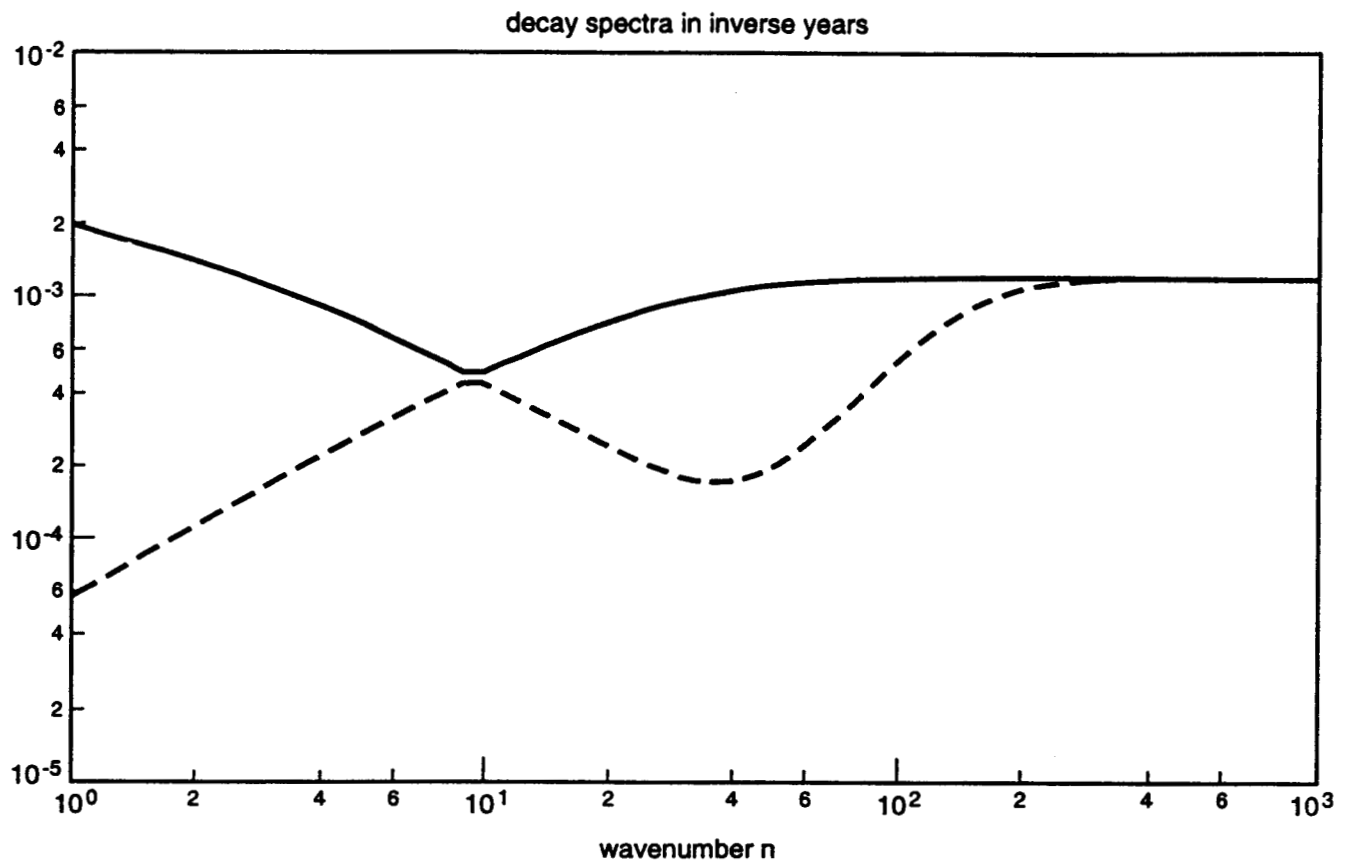


Figure 13a.

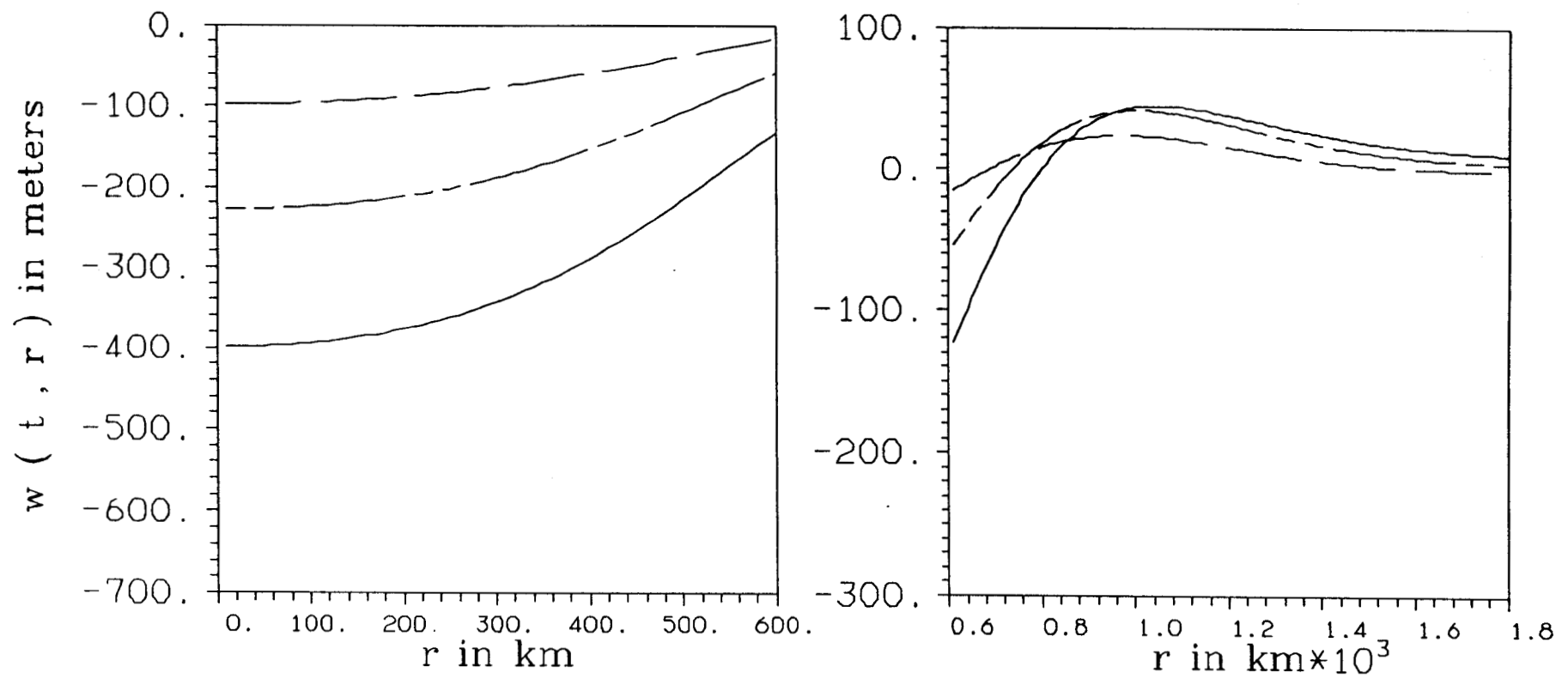


**Figure 13b.**



**Figure A-1.**

$t = 2, 5, \text{ and } 10 \text{ ka}$  displacement both inside and outside of load



(a)

Figure A-2a.

$t = 2, 5, \text{ and } 10 \text{ ka}$  displacement both inside and outside of load

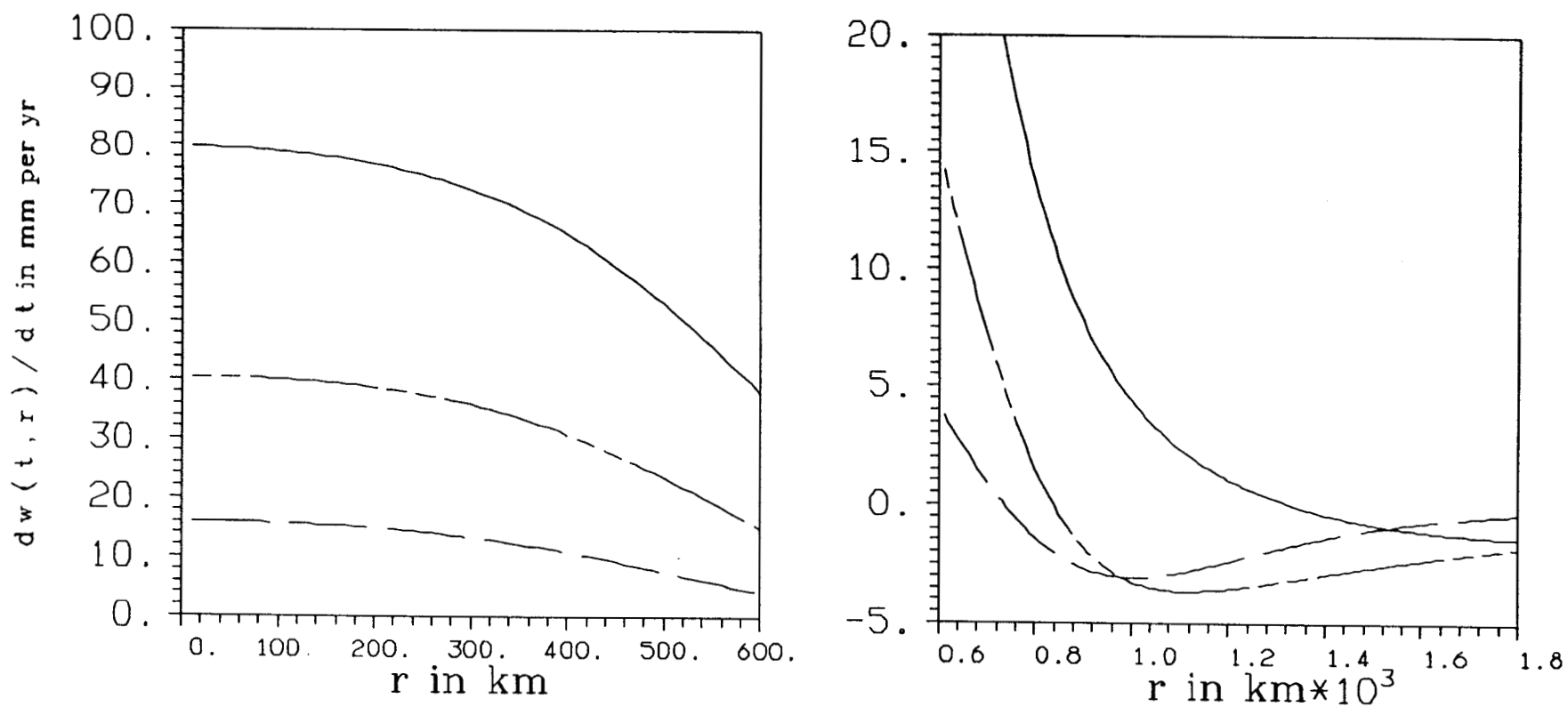
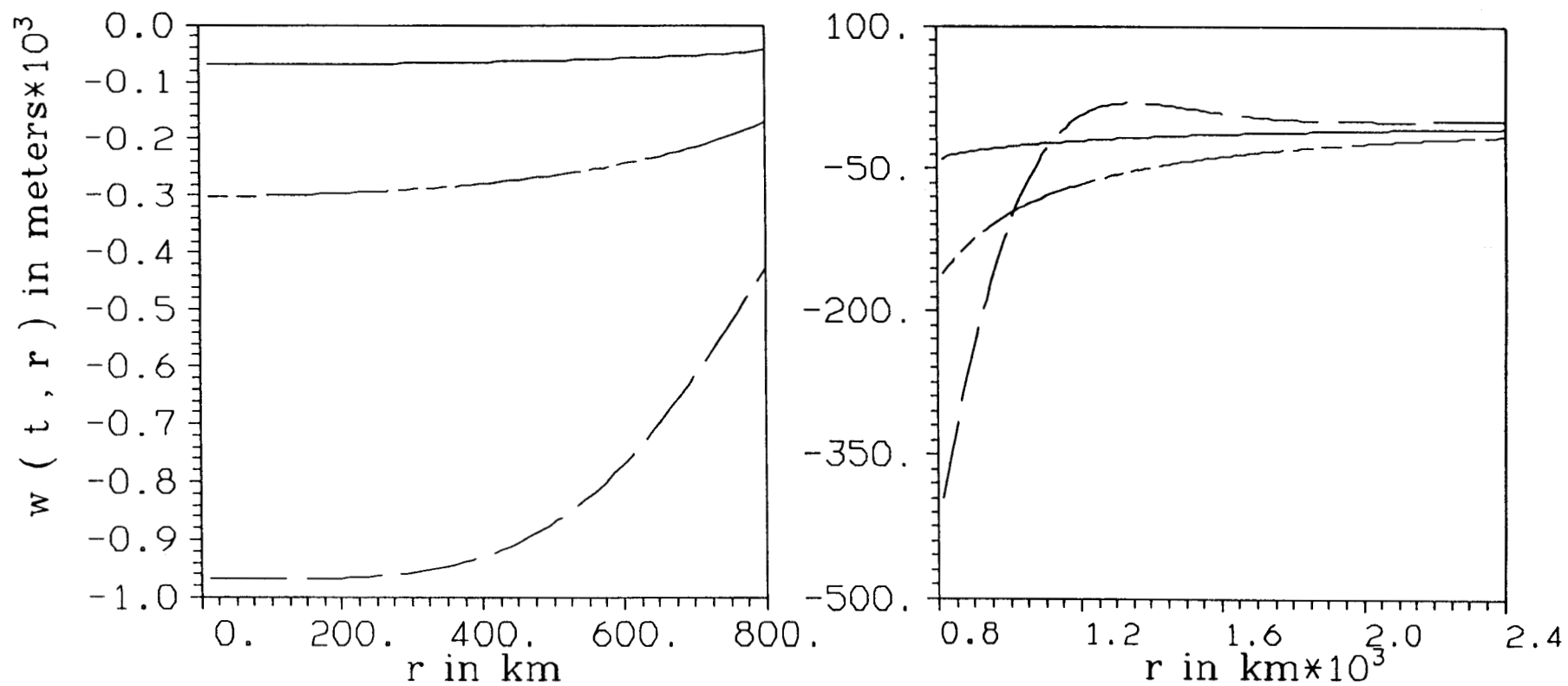


Figure A-2b.

$t = 0, 1, \text{ and } 2400 \text{ ka}$  displacement inside and outside of load



(c)

Figure A-2c.

$t = 0, 1, \text{ and } 2400 \text{ ka}$  displacement inside and outside of load

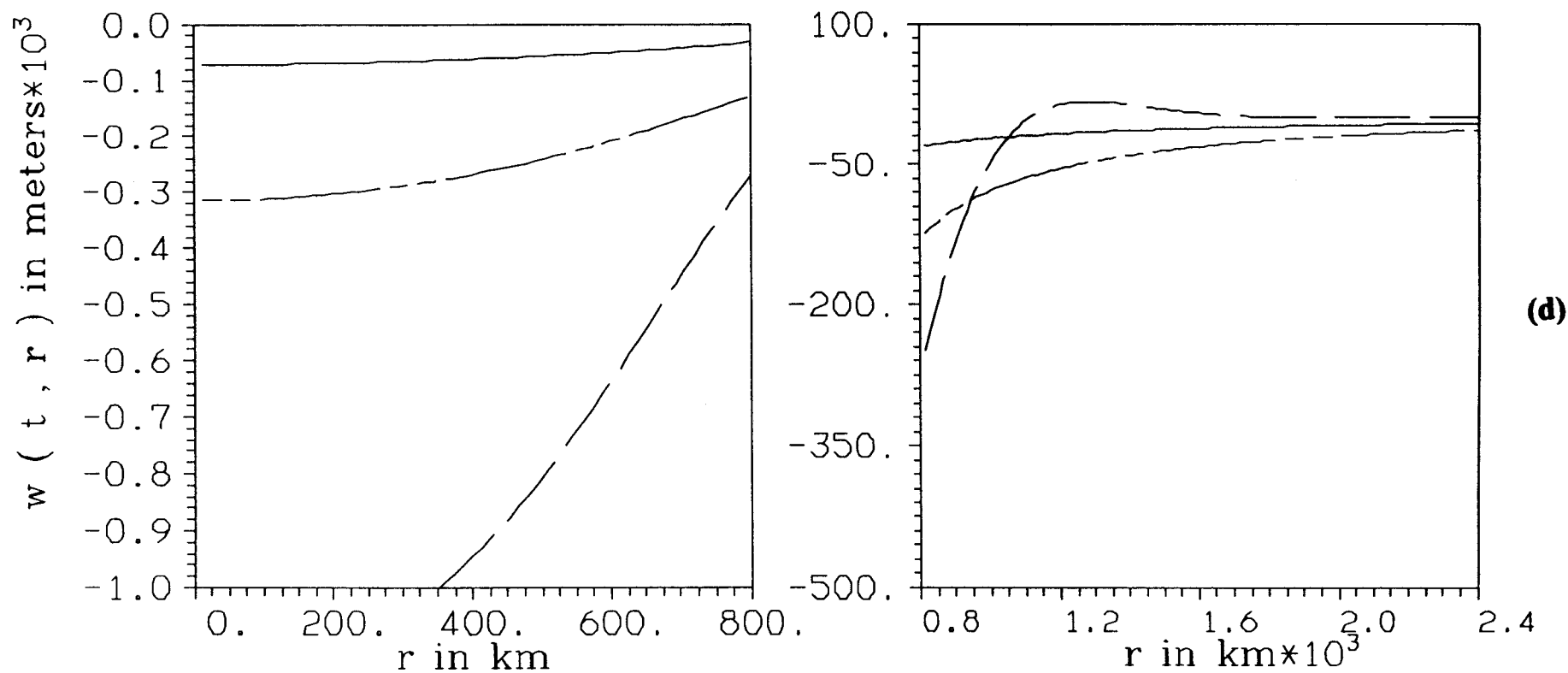


**Figure A-2d.**

ICE-3G Patagonian Load, Displacement at 13 kyr.  
Difference between spher. and flat Earth

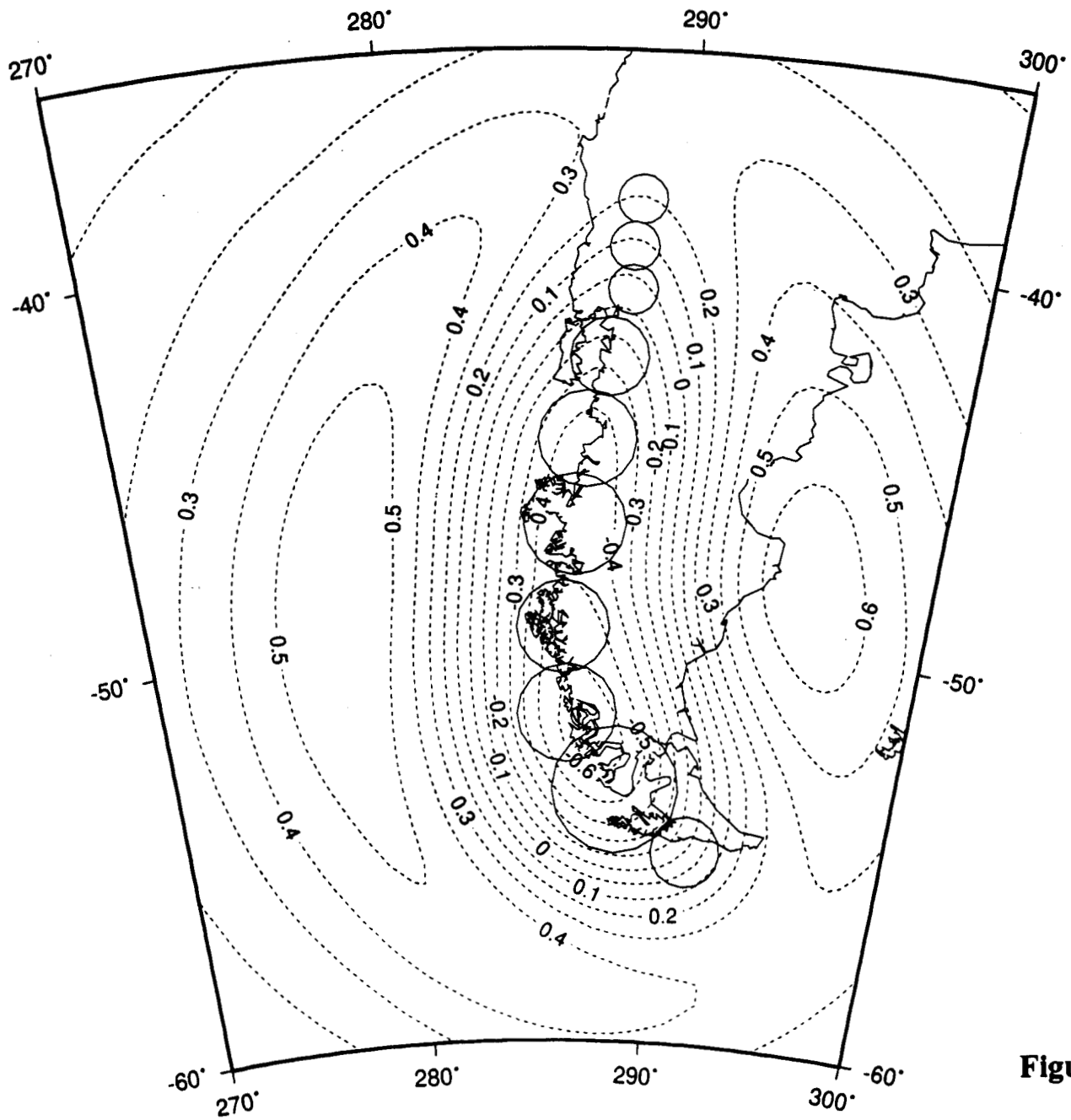


Figure A-3a.



ICE-3G Patagonian Load, Displacement at 13 ka.

lith. thick. = 100 km   Flat-Earth Approx.

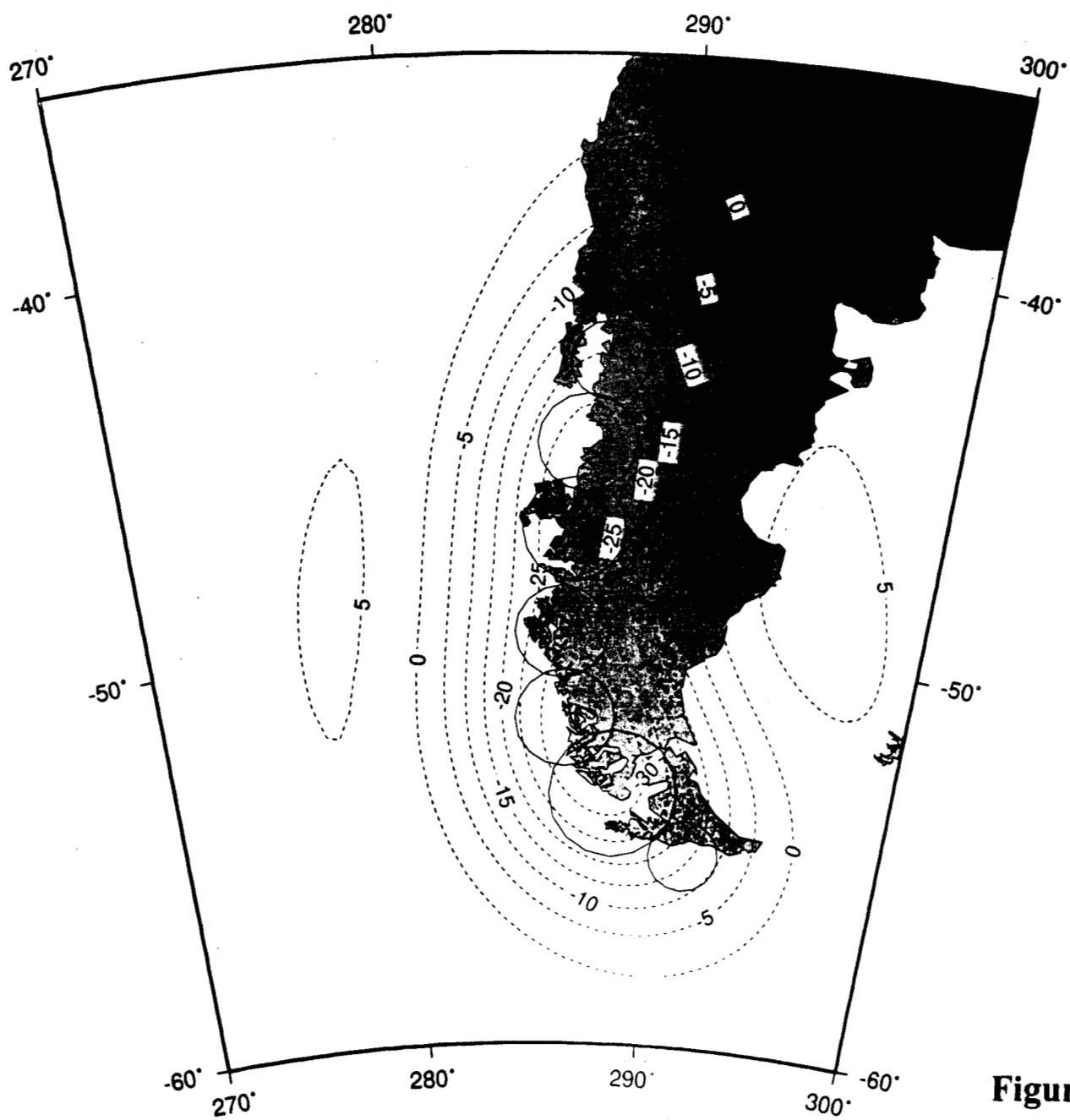


Figure A-3b.

ICE-3G Patagonian Load, Present day vertical rates ( mm per yr )

lith. thick. =100 km Flat-Earth Approx.

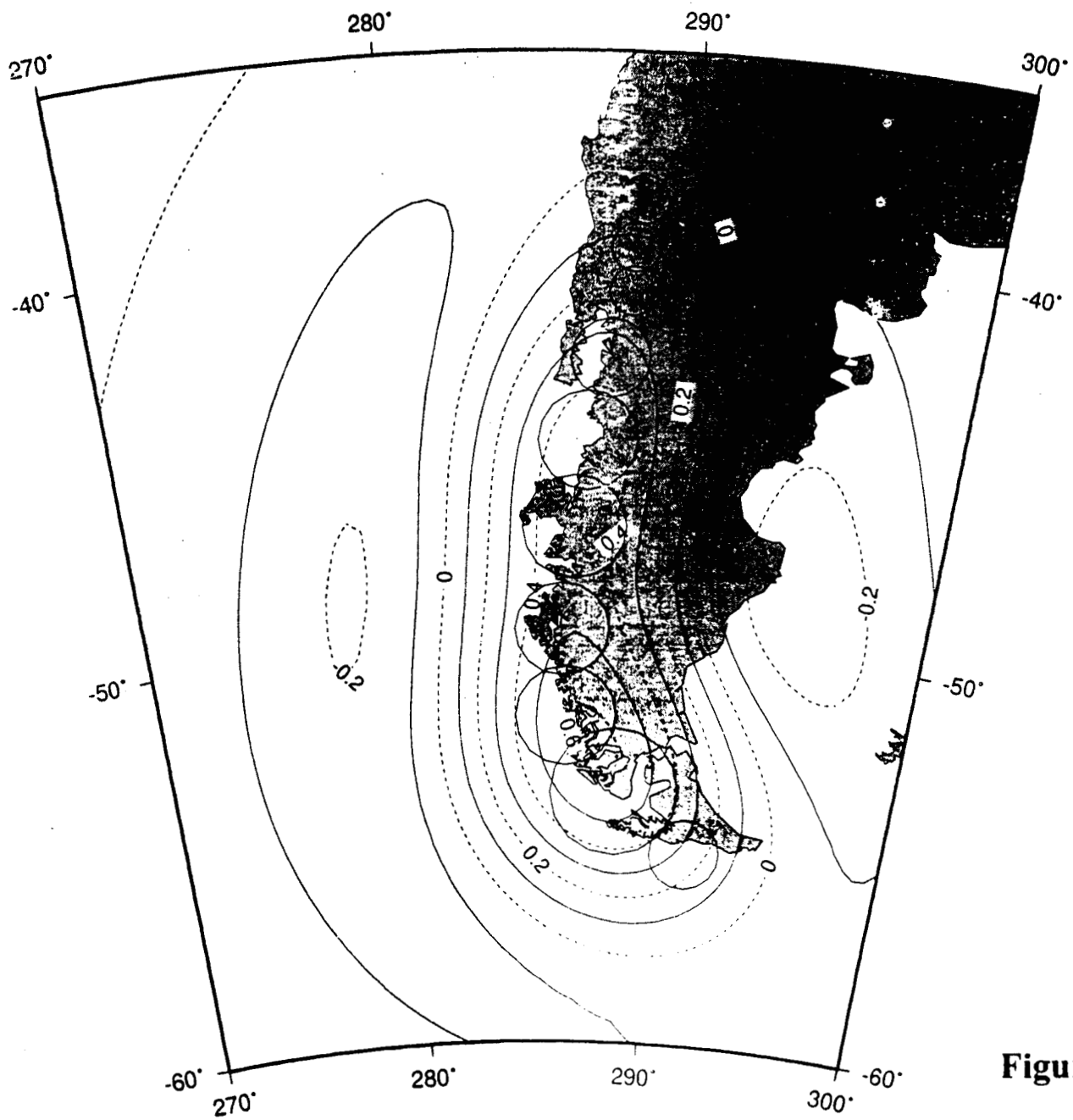


Figure A-3d.

ICE-3G Patagonian Load, Present-day Uplift in mm/yr  
Ramped Load, Summation from 2 to 240  
100 km lithosphere, Spherical Earth

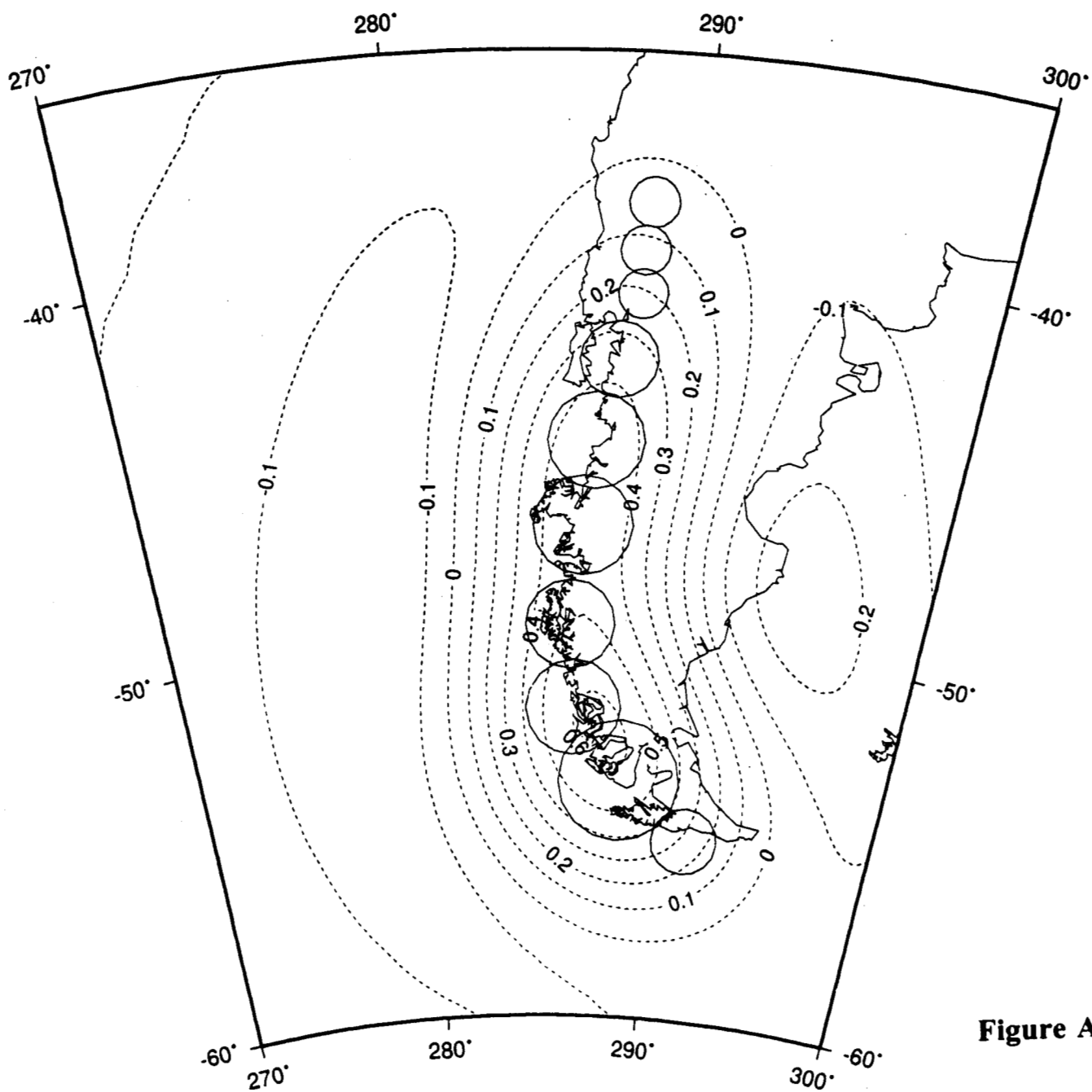


Figure A-3c.